UNIVERSIDAD DE CONCEPCIÓN

FACULTAD DE INGENIERÍA

DEPARTAMENTO DE INGENIERÍA ELÉCTRICA

Axial Flux Permanent Magnet Machines – Development of Optimal Design Strategies

(Máquinas de Flujo Axial e Imanes Permanentes – Desarrollo de Estrategias de Diseño Óptimo)

Tesis para optar al grado de Doctor en Ciencias de la Ingeniería Mención en Ingeniería Eléctrica

The thesis was written under a double doctoral degree agreement between Lappeenranta University of Technology, Finland and University of Concepción, Concepción, Chile and jointly supervised by supervisors from both universities.

WERNER EDUARDO JARA MONTECINOS

CONCEPCIÓN-CHILE

2016

Supervisors Professor Juan Tapia
Department of Electrical Engineering
Faculty of Engineering
University of Concepción
Chile

Professor Juha Pyrhönen
LUT School of Energy Systems
Lappeenranta University of Technology
Finland

Reviewers Professor Metin Aydin
Department of Mechatronics Engineering
University of Kocaeli
Turkey

Professor Bulent Sarlioglu
Department of Electrical and Computer Engineering
University of Wisconsin-Madison
USA

Opponents Professor Metin Aydin
Department of Mechatronics Engineering
University of Kocaeli
Turkey

Professor Bulent Sarlioglu
Department of Electrical and Computer Engineering
University of Wisconsin-Madison
USA

December 2016

Abstract

Werner Eduardo Jara Montecinos

Axial Flux Permanent Magnet Machines – Development of Optimal Design Strategies

Nowadays, rotational electrical machines are involved in all our daily activities. Modern life is inconceivable without electrical machines, both motors and generators, and therefore, machine designers can be considered to play a fundamental role in society. Thus, even a slight improvement in the design, manufacture, materials, or efficiency may be of great significance on a global scale, and can make an important contribution to society. Within this context, the advancement of permanent magnet materials and their use in electrical machines began the era of high-power-density and high-efficiency electrical machines. Further, versatility in the selection of the winding configuration has promoted the success of these machines.

This doctoral dissertation focuses on the electromagnetic design of axial flux permanent magnet machines for low-speed applications. The winding configurations under study are a distributed winding (DW) and a tooth coil winding (TCW). The design equations for an axial flux machine are presented based on three fundamental design variables; tangential stress, outer diameter, and internal to outer diameter ratio. The design equations are validated by a 3D finite element model in an axial flux permanent magnet machine with a distributed winding. An analytical 2D model of the air-gap flux density distribution is developed for a more detailed analysis to improve the accuracy of the machine design and its evaluation. Furthermore, the inductance equations for the distributed winding and the tooth winding are derived in terms of pole pitch, number of slots per pole and phase, and coil pitch to facilitate their application and enhance their usability. The loss sources in a two-stator one-rotor topology are studied focusing mainly on the study of the permanent magnet eddy current losses and their minimization. A novel rotor structure is analysed by the 2D finite element method, which shows a significant reduction in losses in the permanent magnets.

Based on this structure, a 100 kW machine prototype is analysed in order to verify the computed losses.

Keywords: Axial flux machines, eddy currents, finite element analysis, magnetic losses, permanent magnet machines, rotor losses, synchronous machines, distributed winding, tooth coil winding.

Resumen

Werner Eduardo Jara Montecinos

Axial Flux Permanent Magnet Machines – Development of Optimal Design Strategies

En nuestros días, las máquinas eléctricas están íntimamente ligadas con muchas de nuestras actividades diarias. La vida moderna es inconcebible sin estos dispositivos, sea motores o generadores, y por lo tanto, los diseñadores de máquinas juegan un papel fundamental en la sociedad para avanzar hacia equipos más confiables, robusto y amigables con el medio ambiente. En consecuencia, una pequeña mejora en el diseño, construcción, uso de materiales o eficiencia puede tener un gran impacto a escala global, y por lo tanto, puede conllevar a una importante contribución a la sociedad. En este contexto, el avance en el desarrollo tecnológico en las áreas de ciencia e ingeniería ha permitido promover el uso intensivo del imán permanente de alta densidad de energía en aplicaciones de máquinas eléctricas lo que dio inicio a la era de aparatos y sistemas de alta potencia y eficiencia, ampliando el rango de aplicaciones e introduciendo novedosas formas de diseño y control.

Esta Tesis doctoral se orienta al diseño electromagnético óptimo de máquinas de flujo axial con imanes permanentes para aplicaciones de baja velocidad. La configuración del bobinado de estator que se estudia corresponde a bobinados distribuidos y bobinados concentrados. Se presentan el desarrollo de las ecuaciones de diseño para máquinas de flujo axial las que involucran tres parámetros fundamentales; estrés tangencial, diámetro externo y la razón de diámetros. Las ecuaciones de diseño son validadas mediante un modelo de elementos finitos tridimensional en una máquina de flujo axial con devanados distribuidos. Además, se desarrolló un modelo analítico en dos dimensiones para un estudio más detallado de la densidad de flujo en el entrehierro con el objetivo de mejorar la precisión y evaluación del diseño. También, se derivaron las expresiones para estimar la inductancia para los devanados distribuidos y concentrados en términos del paso polar, el número de ranuras por polo y por fase y el paso de bobina facilitando su aplicación y uso.

Asimismo, se analizaron las fuentes de pérdidas en una topología de dos estatores y un rotor central, enfocándose principalmente en el estudio del origen de las pérdidas en los imanes permanentes debido a las corrientes parasitas inducidas y el mecanismo para su minimización. Se analizó una nueva topología del polo excitatriz mediante el método de elementos finitos en 2D, la cual mostró una significativa reducción de estas pérdidas.

Basado en la estructura estudiada, un prototipo experimental de una máquina de 100 kW fue analizada con el objeto de verificar las pérdidas calculadas mediante el modelo de elementos finitos en dos dimensiones.

Acknowledgements

This work was carried out at the Laboratory of Electrical Machine Design, Electrical Engineering Faculty, University of Concepción, Chile between 2012 and 2014 and at the Laboratory of Electrical Drives Technology, Electrical Engineering, LUT School of Energy Systems, Lappeenranta University of Technology, Finland, between 2015 and 2016.

I am especially grateful to my supervisors Professor Juan Tapia, who encouraged me to search for new frontiers and take on new challenges, and Professor Juha Pyrhönen, who gave me the opportunity to do research in Lappeenranta University of Technology. I am grateful for your guidance and patience during my studies in Chile and Finland; you guided me to write scientific publications and to develop critical thinking. Yours suggestion and comments helped me to improve my research and publications. I deeply appreciate the opportunities to work with both my supervisors.

I am grateful for the comments and constructive suggestions of the honoured pre-examiners and opponents, Professor Metin Aydin of University of Kocaeli and Professor Bulent Sarlioglu of University of Wisconsin-Madison; your effort strongly contributed to enhance the quality of this doctoral dissertation.

I would like to express my gratitude to Associate Professor Pia Lindh to invite me to participate in her research, in the different activities developed at LUT, and for her contributions to improve this doctoral dissertation.

Over my doctoral studies I have had the opportunity to be the assistant of Professor Emeritus Rogel Wallace from the University of Concepción, in courses of Electromagnetism and Electromagnetic Waves. This experience and his support allow me to have a deep understanding of electromagnetism, of which I will always be grateful.

I extend my heartfelt thanks to Mr. Ramon Lillo, the technician who has built most of the machines developed in the Faculty of Engineering of the University of Concepción. Working with you has been one of the greatest privileges that I have enjoyed throughout my university studies.

I would like to thank Mr. Peter Jones for improving the language in my journal paper and conference presentation, and Dr. Hanna Niemelä for improving the English language of my doctoral dissertation. Your valuable support and readiness to help made the writing process easier.

I would like to thank Professor Nicola Bianchi from the University of Padova for his support during parts of the development of this doctoral dissertation and for allowing me to make a short stay in Italy.

The financial support by the Comisión Nacional de Investigación Científica y Tecnológica CONICYT through the Project Fondecyt 1130328 and through

CONICYT/National Scholarship/2012-21120920, the Research Foundation of Lappeenranta University of Technology, and the Internationalization project of the University of Concepción is gratefully acknowledged.

I would like to thank the working group of the laboratory testing of electrical machines of the University of Concepción and the Laboratory of Electrical Drives Technology of the University of Lappeenranta. I enjoyed every day studying and working with Cristian Pesce, Ivan Andrade, Javier Riedemann, Jusef Nome, Boris Vera, Gustavo Hunter and Dmitry Egorov as well as the visiting scholar Juan Nohpal and Alejandro Olloqui. The same thanks are also expressed to Ilya Petrov and Maria Polikarpova for their contributions to this doctoral dissertation.

Finally, I reserve this paragraph to express my thanks to my family. To my wife Elizabeth Pereira, thank you for your support and your infinite love for our son Bernardo and for me. I wish to thanks to my parents Werner Jara and Cristina Montecinos for your efforts to give me all the tools necessary for my professional development.

Werner Jara
December 2016
Lappeenranta, Finland

Contents

List of publications related to the topic of the doctoral dissertation

This doctoral dissertation contains material from the following papers. The rights have been granted by the publishers to include the material in the dissertation.

Werner Jara is the principal author and investigator in Publications I, II, V, VI, and VIII. In Publication III, Dr. Lindh was the corresponding author, and Werner Jara participated in the determination and estimation of the electromagnetic losses in the machine by a 2D finite element analysis. In Publication IV, Dr. Minav was the corresponding author, and Werner Jara participated in the design of the axial flux permanent magnet machine with an ironless stator. In Publication V, Dr. Polikarpova was the corresponding author, and Werner Jara participated in the determination and estimation of additional losses in the machine.

I. **W. Jara**, J. A. Tapia, N. Bianchi, J. Pyrhönen, and R. Wallace, "Procedure for fast electromagnetic design of axial flux permanent magnet machines," in *XIX International Conference on Electrical Machines (ICEM), 2014*, Berlin, Germany, pp. 1396–1402, Sept. 2014.

II. **W. Jara**, J. Tapia, J. Pyrhönen and P. Lindh, "Analytical electromagnetic torque estimation of an axial flux permanent magnet machine under saturation," in *2015 IEEE International Electric Machines & Drives Conference (IEMDC)*, Coeur d'Alene, ID, USA, pp. 143–146, May 2015.

III. P. M. Lindh, J. Montonen, H. Jussila, J. Pyrhönen, **W. Jara**, and J. A. Tapia, "Axial flux machine structure reducing rotor eddy current losses," in *2015 IEEE International Electric Machines & Drives Conference (IEMDC)*, Coeur d'Alene, ID, USA, pp. 143–146, May 2015.

IV. T. A. Minav, H. Handroos, J. Heikkinen, J. A. Tapia, and **W. Jara**, "Modelling Study of an Optimum Electric Motor for Directly Driven Hydraulic Pump Emulator in Real-Time HIL-Simulation," in *Scandinavian International Conference on Fluid Power 2015*, May 2015.

V. M. Polikarpova, P. Ponomarev, P. Lindh, I. Petrov, **W. Jara**, V. Naumanen, J. A. Tapia, and J. Pyrhönen, "Hybrid Cooling Method of Axial-Flux Permanent Magnet Machines for a Vehicle Applications," *IEEE Trans. Ind. Electron.*, vol. 63, no. 12, pp. 7382–7390, Dec. 2015.

VI. **W. Jara**, P. Lindh, J. Tapia, and J. Pyrhönen, "A novel rotor structure for an Axial Flux PM machine: Performance analysis," in *2016 International Symposium on Power Electronics, Electrical Drives, Automation and Motion (SPEEDAM)*, Capri, Italy, 2016, pp. 237–241.

VII. **W. Jara**, P. Lindh, J. A. Tapia, I. Petrov, A. K. Repo, and J. Pyrhönen, "Rotor Eddy-Current Losses Reduction in an Axial Flux Permanent-Magnet Machine," *IEEE Trans. Ind. Electron.*, vol. 63, no. 8, pp. 4729–4737, Aug. 2016.

VIII. **W. Jara**, I. Petrov, J. A. Tapia, P. Lindh, and J. Pyrhönen," Analytical Model of Tooth-Coil Winding Permanent Magnet Synchronous Machines with Modular U-Shape Stator," in *International Conference on Electrical Machines (ICEM), 2016*, Sept. 2016. (Status: accepted).

List of Figures

List of Tables

Nomenclature

Latin alphabet

A	linear current density	A/m
a	constant	–
B	magnetic flux density	T
B_r	remanence flux density	T
b	constant	–
b	width	m
b_s	slot width	m
b_t	tooth width	m
b_0	slot opening	m
C_M	torque coefficient	–
c	constant	–
D_i	internal diameter	m
D_o	external diameter	m
D_m	mean diameter	m
E	induced voltage	V
F	force, scalar	N
f	frequency	Hz
G_c	magnetic load of the yoke	–
G_t	magnetic load of the teeth	–
H	magnetic field strength	A/m
H_c	coercivity related to the flux density	A/m
h	height	m
h_{hs}	height of the slot opening	m
h_{PM}	permanent magnet height	m
h_s	slot height	m
h_{yr}	height of the rotor yoke	m
h_{ys}	height of the stator yoke	m
J	current density	A/m^2
I	electric current, in RMS	A
k	diameter ratio (D_i/D_o)	–
k_C	Carter factor	–
k_{Cu}	space factor for copper	–
k_d	distribution factor	–
k_{Fe}	space factor for iron	–
k_p	pitch factor	–
k_R	skin effect factor	–
k_{trq}	torque correction factor	–
k_u	slot leakage flux factor	–
k_w	winding factor	–
L	self-inductance	H

L_d	tooth tip leakage inductance	H
L_{ew}	end-winding leakage inductance	H
L_m	magnetizing inductance	H
L_u	slot leakage inductance	H
L_h	air-gap harmonic leakage inductance	H
l	length	m
l_c	total length of the conductor	m
l_e	radial stator length	m
l_{ef}	effective stator core length	m
M	mutual inductance	H
M	magnetization	A/m
m	phase number	–
m_r	mass of the rotating part	kg
N	number of turns in series in a phase	–
P	electric power	W
p	number of pole pairs	–
Q_s	slot number	–
q	number of slots per pole and phase	–
q_{ph}	number of spokes per phase	–
R_{AC}	electrical resistance of the phase winding	Ω
r	radius	m
r_m	mean radius	m
S_{slot}	slot area	m^2
S_1	vectors related to the x position of a given phase coil	–
S_2	vectors related to the sign of a given phase coil	–
sgn	sign function	–
s_{sq}	skewing pitch ratio	–
T	torque	Nm
t	time	s
t	machine periodicity	–
U	voltage	V
U	depiction of a phase	–
V	volume	m^3
V	depiction of a phase	–
v	harmonic order	–
W	depiction of a phase	–
W	coil pitch in the number of slots	–
w_c	coil span	m
x	x-coordinate	m
y	y-coordinate	m
y_Q	pole pitch in the number of slots	–
z	z-coordinate	m
z_Q	number of conductors in a slot	–
α_{PM}	relative permanent magnet width	–

β	constant	–
γ	displacement angle	rad, °
δ	air-gap length	m
δ	load angle	rad, °
δ_{PM}	equivalent air-gap length	m
δ_{ef}	effective air gap (taking into account the influence of iron)	m
Θ	current linkage	A
θ	angle	rad, °
λ	permeance, leakage permeance factor	
μ	permeability	V·s/(A m)
μ_r	relative permeability	–
μ_0	permeability of vacuum	V·s/(A m)
ρ	resistivity	Ω·m
σ	conductivity	S/m
σ_{Ftan}	tangential stress	Pa
τ_c	coil pitch	rad, °, m
τ_p	pole pitch	rad, °, m
τ_s	slot pitch	rad, °, m
Φ	magnetic flux	Wb
ϕ	phase angle	rad, °
Ψ	magnetic flux linkage	V·s
ω	electric angular velocity, angular frequency	rad/s

Dimensionless numbers

Re	Reynolds number

Superscripts

^	peak/maximum value, amplitude

Subscripts

ew	end winding
Fe	iron
m	magnetizing
PM	permanent magnet
s	slot
t	tooth
vent	ventilation
x	*x*-direction
y	*y*-direction, yoke
δ	air gap
ρ	rotational losses
ρ_w	windage losses

ρb	bearing losses

Abbreviations

2D	two-dimensional
3D	three-dimensional
AF	axial flux
AFPM	axial flux permanent magnet
DL	double layer
DW	distributed winding
FE	finite element
PM	permanent magnet
RF	radial flux
RFPM	radial flux permanent magnet
SL	single layer
TCW	tooth coil winding

1 Introduction

From the beginning of the electrical machine development, the axial flux (AF) topology has been considered. In 1821, Michael Faraday presented a primitive disc-shaped machine, similar to an axial flux machine. Later, when Thomas Davenport obtained the first American patent of a radial flux (RF) electrical machine in 1837, this topology became the commonly used one, replacing the axial topology except for certain non-typical applications. However, scientific studies show that the axial flux topology provides a better power–weight ratio when compared with radial flux machines, being a suitable option to electrical vehicles and aircrafts (Chan, 1987; Surong et al., 1999; Yiang and Chuang, 2007; Crescimbini et al., 2012; Aydin and Güben, 2014; Nakahara et al., 2014).

Moreover, because of its compact and thin structure, the AF topology is appropriate for different applications such as fans, pumps, wheels, and domestic applications (Chan, 1987; Kahourzade et al., 2014). These advantages have been strongly enhanced with the inclusion of permanent magnets (PM) in the electrical machine development as a result of technological improvements of this material (Campbell, 1974; Wang et al., 2008).

Currently, the focus of permanent magnet machine designers is on the study and development of a non-traditional winding configuration, that is, the fractional slot non-overlapping concentrated windings. Hereafter, this winding configuration is referred to as a tooth-coil winding (TCW). Different studies have reported that TCW allows to obtain a higher power density in the machine, a high efficiency, and a reduction in the cogging torque (Cros and Viarouge, 2002; El-Refaie, 2010; El-Refaie, 2013). For example, a low cogging torque can be achieved in PM machines when a TCW with $2p = Q_s \pm 2$ is selected (Jafari-Shiadeh and Ardebili, 2013). However, this technique also has some problems such as an increase in the rotor magnetic losses caused by the higher current linkage harmonic components inherent in this winding configuration. Therefore, machine designers have directed their efforts to minimize the rotor losses to avoid problems of heat dissipation and the risk of demagnetization.

1.1 Axial flux permanent magnet machine

In axial flux permanent magnet (AFPM) machines, the air-gap flux, produced by the magnets, has an axial direction while the active parts of conductors are radially positioned as shown in Fig. 1.1. Owing to its excellent power/weight ratio and particular geometrical shape, this topology has certain advantages in some particular applications when compared with an RF machine. Several studies show that the AF topology provides a better power/weight ratio when compared with RF machines, being thus a suitable option in electrical vehicles and aircrafts. AFPM machines are, because of their short axial length, an attractive alternative to radial flux permanent magnet (RFPM) machines in different applications, such as fans, pumps, valve control, machine tools, and in-wheel

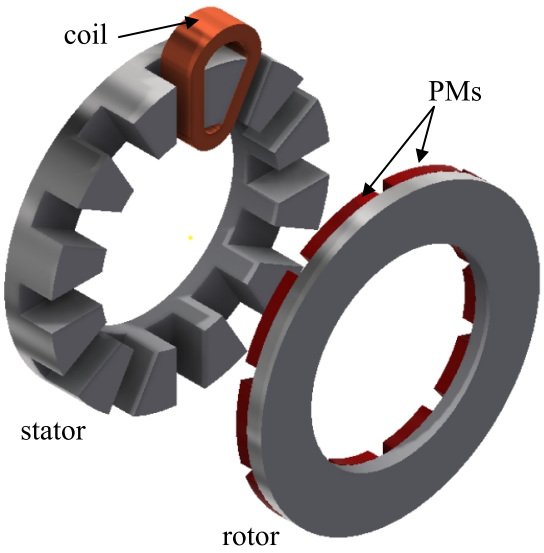

Fig. 1.1. Basic structure of a one-stator one-rotor axial flux permanent magnet machine. (Source: own elaboration)

motors. Moreover, by a TCW configuration, it is possible to further improve the power/weight ratio of these electrical machines.

The AFPM machine can be classified depending on the number of stators and rotors as shown in Fig. 1.1 and Fig. 1.2. Multiple stators and multiple rotors can be made by combining the structures described above. The one-stator one-rotor structure is used mainly in low- and medium-power applications because of the simplicity of the manufacture and the compact structure (Kahourzade et al., 2014), whereas the other

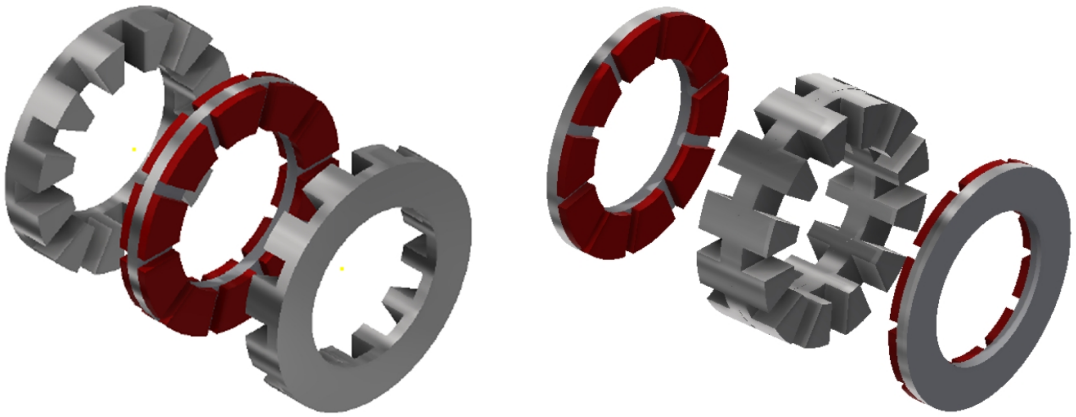

a) b)

Fig. 1.2. AFPM; a) two-stator configuration with q=2/5, and b) two-rotor configuration with q=2/5. (Source: own elaboration)

configurations are used to increase the output power of the machine, to reduce the axial forces over the bearing, and to decrease the cogging torque (Letelier et al., 2007).

Other configurations of AFPM machines can be obtained by various stator and pole constructions, such as a North-South (NS) or North-North (NN) structure, a slotted or slotless stator, an iron or ironless stator structure, an iron or ironless rotor structure, or a core-wound (toroidal) or slot-wound stator (Aydin and Gulec, 2014; Kahourzade et al., 2014; Kim, Choi, and Sarlioglu, 2016).

An interior permanent magnet rotor can be used to protect the PMs from mechanical impacts and corrosion (Aydin, Surong, and Lipo, 2006). However, the power density is lower compared with the surface-mounted structure because of an increase in the rotor width and the leakage flux.

The wide range of AFPM machine structures together with the alternative winding configurations provides various options to develop a proper solution for a specific application.

1.2 Tooth coil winding

The use of a TCW in the stator (see Fig. 1.2(a) and Fig. 1.2(b)) is a relatively new approach, and most of the technical literature addresses the impact of this winding on RF machines. A tooth coil winding either as an all teeth wound (double-layer) or an alternate teeth wound (single-layer) construction is shown in Fig. 1.3. The number of slots per pole and phase (q) of a three-phase machine that can be equipped with a TCW is less than or equal to 1/2.

From the viewpoint of the manufacturing process, the TCW provides several advantages over the distributed winding (DW):

- As the coils are wound around a single tooth, the end winding is short, thereby reducing the copper mass in the machine (Magnussen and Sadarangani, 2003). The short end winding results in a reduction in the total diameter of the AFPM machine and enables the development of a compact structure.
- The low slot number (close to the pole number) allows the use of segmented structures and a soft magnetic material to facilitate the manufacturing process (Petrov, 2015).
- It is possible to achieve a high copper space factor when segmented structures, open slots, and pre-wound coils are used (Viarouge and Gelinas, 1998; Jack et al., 1999; Cros et al., 2001; Akita et al., 2003).

From the perspective of machine performance, it is possible to achieve:

- A low cogging torque and a low ripple torque (Jafari-Shiadeh and Ardebili, 2013).
- Low winding losses, which reduce the heat dissipation requirement.

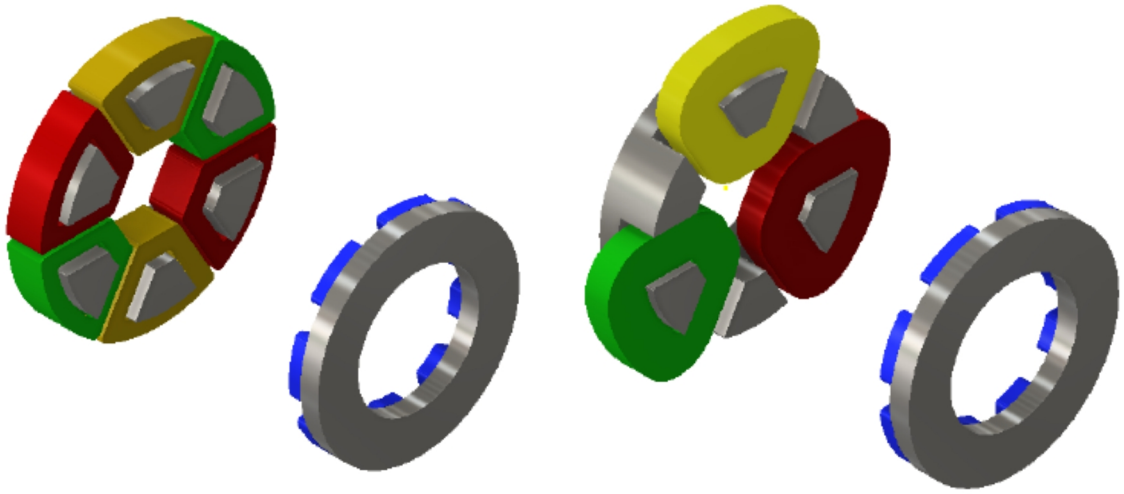

a) b)

Fig. 1.3. 6-Slot 8-pole AFPM machine with two types of TCW: a) all teeth wound, b) alternate teeth wound. (Source: own elaboration)

- Because some pole and slot configurations have a high value of harmonic leakage inductance (Ponomarev et al., 2014), it is possible to develop a wide constant power–speed range even when surface-mounted permanent magnets are used.
- A high fault tolerance capability because of the magnetic decoupling between the different phases. Physical decoupling is also possible in alternate teeth wound TCWs (El-Refaie, 2010).

1.3 Design equations

This section presents an analytical expression for the electromagnetic torque developed by the axial flux machine, depending on the geometrical dimensions and the electrical and magnetic parameters. This approach achieves the best diameter ratio to obtain the maximum electromagnetic torque for a given value of tangential stress and outer diameter. A first estimation is made with a number of simplifications in order to obtain a simple expression for the developed torque. Subsequently, in the second estimation, the non-ideal effects such as magnetic saturation in the iron, the effect of armature reaction, and leakage flux produced by the stator winding are taken into account. Based on these electromagnetic phenomena, a correction factor is determined for the ideal torque expression.

1.3.1 Assumptions

The torque developed by an axial flux permanent magnet machine can be obtained from the electromagnetic force dF acting on the surface current in the air gap as shown in Fig. 1.4. This model makes the following simplifications:

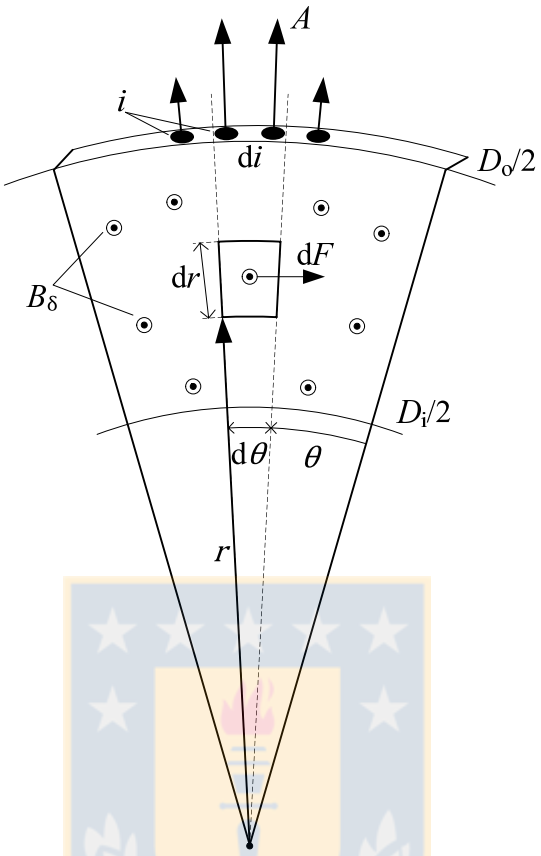

Fig. 1.4. Electromagnetic force over a surface current element. (Source: own elaboration)

i. The maximum value of the sinusoidal air-gap flux distribution is constant along the radial direction. Since the machine excitation is provided by a high-energy-product permanent magnet, $\hat{B}_\delta$ is assumed constant.
ii. The slot current is distributed in the air gap as a very thin sheet with a linear current density A.
iii. The linear current density has a sinusoidal distribution with an azimuthal dependence.
iv. The linear current density and air-gap flux density distributions have a displacement angle γ. This angle is imposed by the control systems.
v. A slotless stator and infinite iron permeability are considered for the sake of simplicity.

The electromagnetic torque over a differential proportion of the air gap as a function of the radius r is given by

$$dT = r dF = B_\delta A r^2 dr d\theta \,, \tag{1.1}$$

where

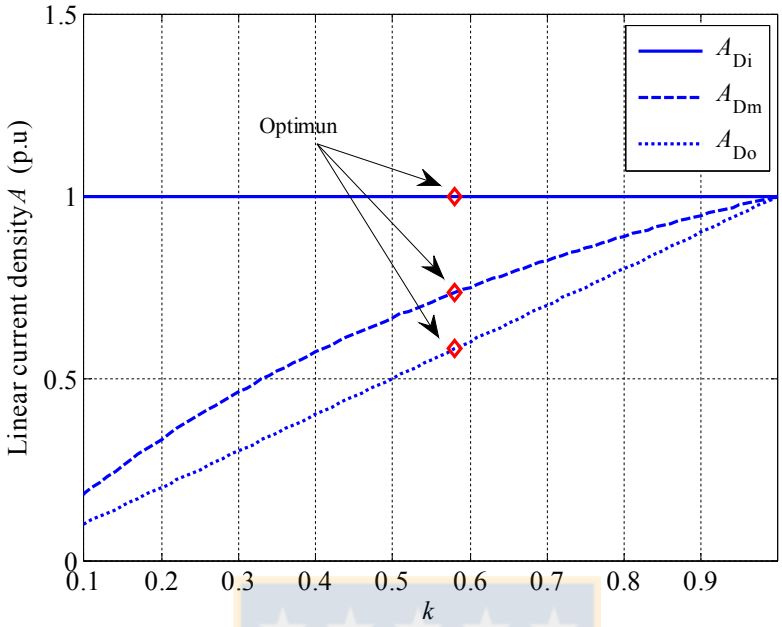

Fig. 1.5. Electrical loading variation as a function of diameter ratio considering the tangential stress defined at the inner diameter. (Source: own elaboration)

$$B_\delta(\theta) = \hat{B}_\delta \cos(\theta) \tag{1.2}$$

$$A(\theta, r) = \hat{A}(\mathrm{r}) \cos(\theta - \gamma)\,. \tag{1.3}$$

The total torque is obtained by integrating Eq. (1.1) over the entire surface of the air gap

$$T = \sigma_{\mathrm{Ftan}} \pi \frac{D_\mathrm{o}^3}{8} k(1 - k^2)\,, \tag{1.4}$$

where k is defined as the diameter ratio, given by

$$k = \frac{D_\mathrm{i}}{D_\mathrm{o}}\,. \tag{1.5}$$

Tangential stress is defined at the inner diameter of the machine, resulting in

$$\sigma_{\mathrm{Ftan}} = \left(\frac{\hat{A}_{D_\mathrm{i}} \hat{B}_\delta}{2} \cos\gamma \right). \tag{1.6}$$

The above is due to the fact that the electrical loading is at the maximum at the inner radius of the machine. In Fig. 1.5 the respective electrical loading at the inner diameter, the middle diameter, and the external diameter is presented in terms of diameter ratio (k).

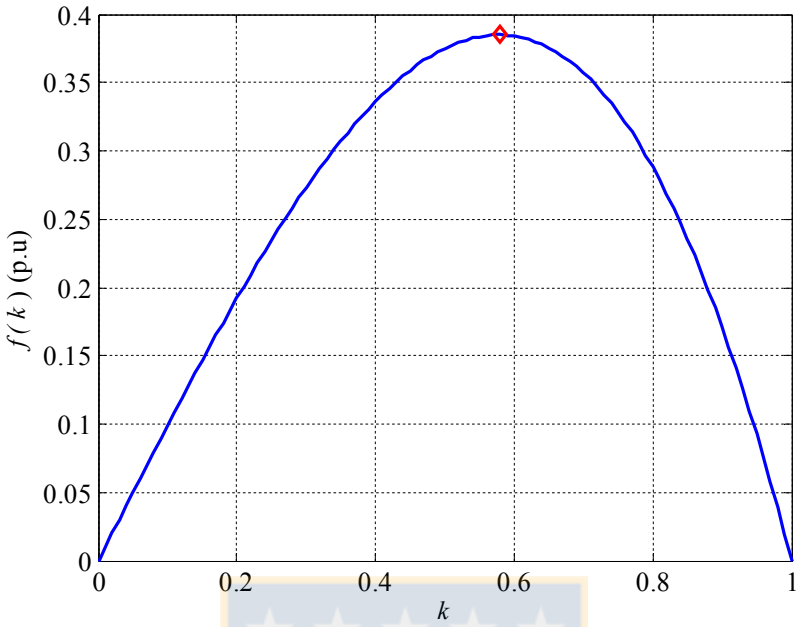

Fig. 1.6. Variation of the air-gap torque function as a function of diameter ratio. (Source: own elaboration)

1.3.2 Optimal diameter ratio

It can be noticed from Eq. (1.4) for given outer diameter and tangential stress values that torque is proportional to the torque function defined by (Campbell, 1974; Chan, 1987; Parviainen, 2005)

$$f(k) = k(1 - k^2)\,. \tag{1.7}$$

Evolution of (1.7) with respect to the diameter ratio is shown in Fig. 1.6. The maximum of this function is found at

$$k_{\text{opt}} = \frac{1}{\sqrt{3}}. \tag{1.8}$$

Substituting Eq. (1.8) into Eq. (1.7), the expression for the maximum torque becomes

$$T_{\text{max}} = \frac{2\sqrt{3}}{9}\sigma_{\text{Ftan}}\frac{\pi D_{\text{o}}^3}{8}. \tag{1.9}$$

1.3.3 Geometrical relations

The main dimensions of the machines are shown in Fig. 1.7(a), and their expressions are given by the magnetic and electrical loading of the machine. For convenience, a linear

representation of the machine is considered along a cylindrical cutting plane at the mean diameter as shown in Fig. 1.7(b). Based on the magnetic flux continuity law, it is possible to express the middle stator tooth width and yoke height as

$$b_{\mathrm{t}} = \frac{\pi D_{\mathrm{o}}}{2Q_{\mathrm{s}}} \cdot (1+k) G_{\mathrm{t}} \tag{1.10}$$

$$h_{\mathrm{y}} = \frac{D_{\mathrm{o}}}{4p} (1+k) G_{\mathrm{y}}\,, \tag{1.11}$$

where G_{t} and G_{y} represent the tooth saturation ratio and the yoke saturation ratio with respect to the air-gap flux density, respectively, and their expression is given by (Tapia et al., 2013):

$$G_{\mathrm{t}} = \frac{\hat{B}_{\delta}}{k_{\mathrm{Fe}} \hat{B}_{\mathrm{t}}} \tag{1.12}$$

$$G_{\mathrm{y}} = \frac{\hat{B}_{\delta}}{k_{\mathrm{Fe}} \hat{B}_{\mathrm{y}}}\,. \tag{1.13}$$

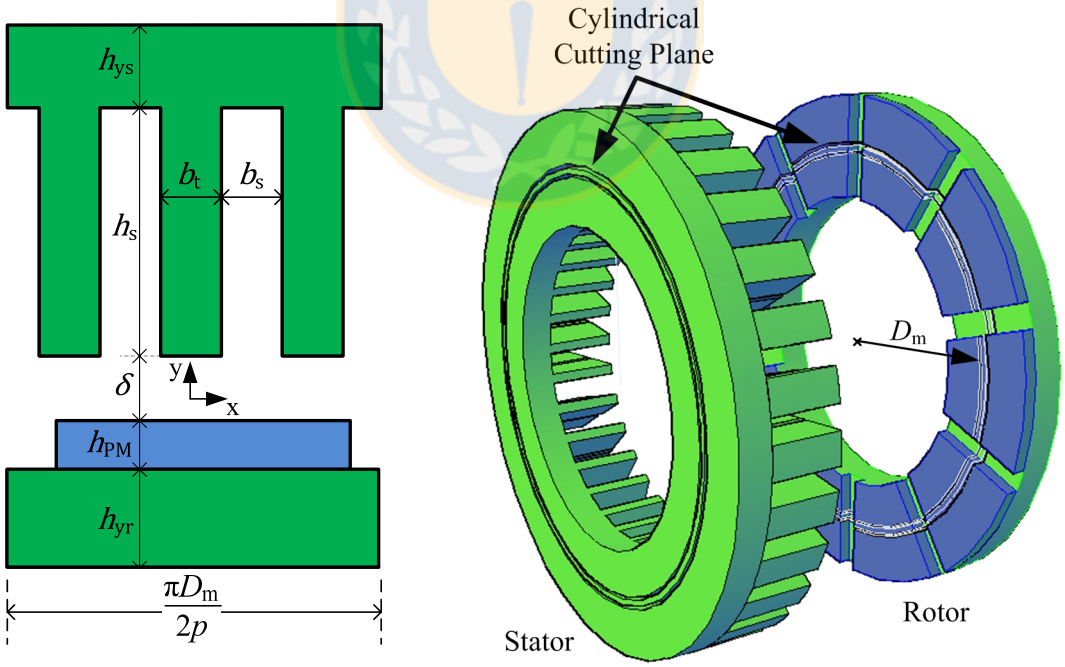

a) b)

Fig. 1.7. Machine geometry; a) machine main dimensions, b) cylindrical cutting plane. (Jara et al., 2015)

Table 1.1. Design data. (Jara et al., 2014)

Symbol	*Variable*	*Value*	*Unit*
D_o	Outer stator diameter	250	mm
J	Current density	3.2	A/mm^2
$\hat{B}_\delta$	Air-gap flux density	0.9	T
$\cos\gamma$	Displacement factor	1	
Q_s	Slot number	30	
k_{Cu}	Copper space factor	0.5	
p	Number of pole pairs	5	

The slot width can be determined by the middle stator tooth width and the total geometry of the machine;

$$b_s = \frac{\pi D_o}{2Q_s}(1+k)(1-G_t)\,. \tag{1.14}$$

Finally, because the slot must accommodate the current of the conductors, the expression of the slot height can be written as

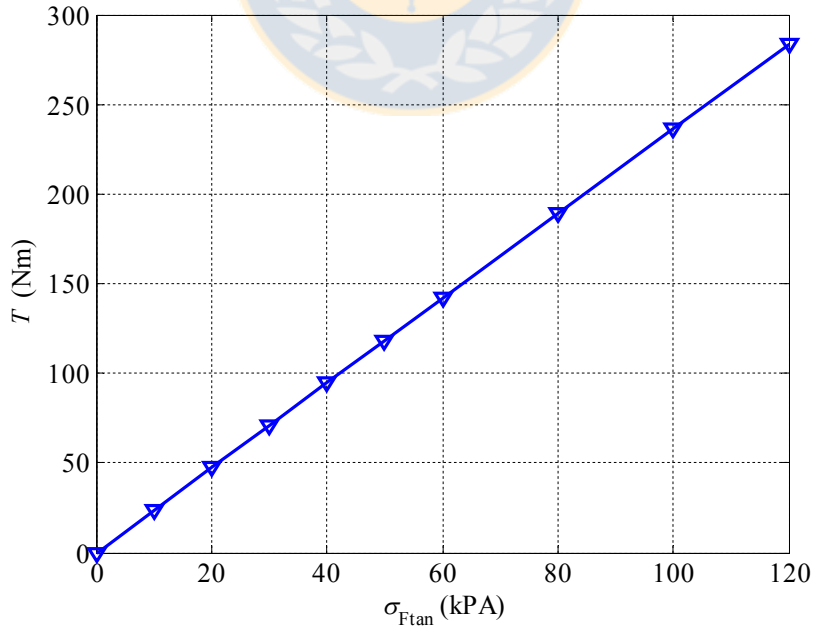

Fig. 1.8. Ideal torque as a function of tangential stress defined by Eq. (1.6) with the boundary conditions set in Table 1.1. (Source: own elaboration)

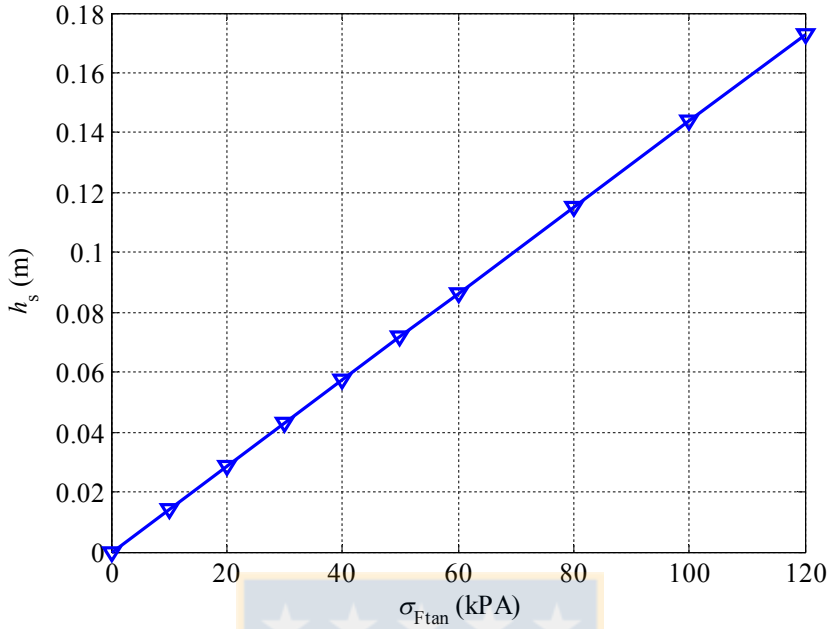

Fig. 1.9. Slot height as a function of tangential stress defined by Eq. (1.6). (Source: own elaboration)

$$h_{\mathrm{s}} = \frac{2\sigma_{\mathrm{Ftan}}}{\sqrt{2}k_{\mathrm{Cu}}J(1-G_{\mathrm{t}})}. \tag{1.15}$$

In the no-load condition, the only magnetic sources are the rotor permanent magnets. For a non-slotted stator and infinite iron permeability, the height of the permanent magnet is given by

$$h_{\mathrm{PM}} = \frac{\frac{\hat{B}_{\delta}}{\mu_{\mathrm{o}}}\delta}{H_{\mathrm{c}} - \frac{H_{\mathrm{c}}}{B_{\mathrm{r}}}\hat{B}_{\delta}}. \tag{1.16}$$

1.4 Optimal design example

Equation (1.9) provides that for a given external diameter value, the maximum torque developed by the machine is proportional to the tangential stress. For instance, for the design data of Table 1.1, the torque curve is obtained as a function of tangential stress shown in Fig. 1.8.

However, the structure of the machine changes significantly depending on the tangential stress value used as shown in Fig. 1.9. This can be demonstrated by Eq. (1.15), which establishes the relationship between the height of the slot and the tangential stress.

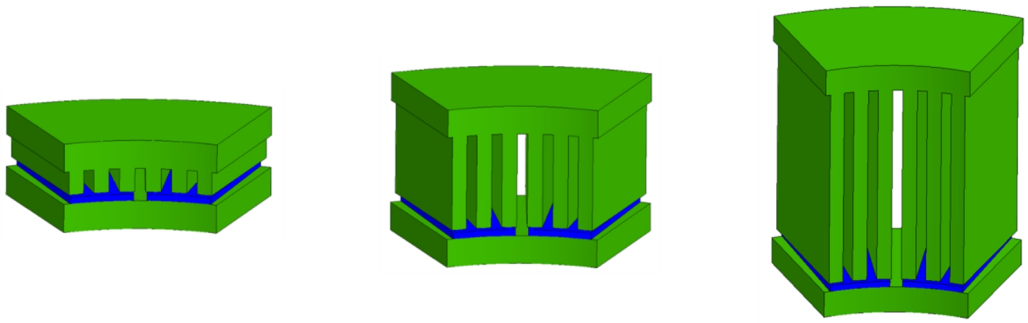

a) 20 kPa b) 40 kPa c) 80 kPa

Fig. 1.10. Design results (based on the data of Table 1.1). A linear increase in the slot depth seems to produce a linear increment in the tangential stress. However, there are phenomena restricting the linear increase in the stress such as leakage and saturation, the effects of which will be studied later in the dissertation. (Jara et al., 2014)

Two-pole machine sections are shown in Fig. 1.10(a) to (c) for 20 kPA, 40 kPA, and 80 kPA, respectively. Since the teeth magnetic load (G_t) and the current density (J) are constants, to allocate the required current to reach the specified tangential stress, the slot depth increases proportionally according to σ_{Ftan}. As a result, the effective torque capacity will decrease as this length increases, degrading the machine performance as a result of the magnetic saturation of the stator iron and the leakage flux. These phenomena are not considered in Eq. (1.9), because we assume a slotless stator and infinite iron permeability. These two assumptions will be removed by following the procedure presented in the next sections.

1.4.1 Non-ideal parameters

In this section, magnetizing and leakage inductances are determined analytically in order to obtain a better approximation of the torque value given by Eq. (1.9).

Permanent magnet height

For an ideal case, the reluctance of the magnetic circuit is only defined by the air-gap length, the value of which is given by Eq. (1.16). In the non-ideal case, this reluctance increases with the iron reluctance (and saturation); this fact can be taken into account by

$$h'_{\mathrm{PM}} = \frac{\frac{\hat{B}_\delta}{\mu_0} k_{\mathrm{C}} \delta + \hat{H}_{\mathrm{t}} h_{\mathrm{s}} + \hat{H}_{\mathrm{y}} \frac{\pi D_{\mathrm{m}}}{2p}}{H_{\mathrm{c}} - k_{\mathrm{C}} \frac{B_{\mathrm{r}}}{H_{\mathrm{c}}} \hat{B}_\delta}, \tag{1.17}$$

where k_C is the Carter factor (Pyrhönen, Jokinen, and Hrabovcová, 2008).

Induced voltage

The height of the PM is determined for the no-load condition by Eq. (1.16), which remains invariant for all the values of tangential stress. However, to keep the magnetic flux constant, the height of the PM should be increased according to Eq. (1.17). If the height of the PM remains constant, one immediate effect is a decrease in the induced voltage, which can be approximated by

$$E' = \left(\frac{h_{\mathrm{PM}}}{h'_{\mathrm{PM}}}\right) E. \tag{1.18}$$

Magnetizing inductance

The mutual flux linkages produced by the stator current distribution are represented by the magnetizing inductance. This parameter can be calculated for an axial flux machine configuration in order to take into account an infinitely permeable iron (Pyrhönen, Jokinen, and Hrabovcová, 2008)

$$L_{\mathrm{m}} = \mu_0 \frac{m \cdot D_{\mathrm{o}}}{4\pi p^2 \delta_{\mathrm{PM}}} (1 - k^2)(k_{\mathrm{w}} N)^2, \tag{1.19}$$

where δ_{PM} is the equivalent air-gap length taking into account the physical air-gap length and the magnet height ($\delta + h_{\mathrm{PM}}/\mu_{\mathrm{r,PM}}$). However, the non-ideal iron permeability will reduce the amount of flux for the same current, which results in a lower value of magnetizing inductance. In order to introduce this effect, the effective air gap is calculated considering the magnetic voltage drop along the magnetic circuit

$$\delta_{\mathrm{ef}} = k_{\mathrm{C}} \delta_{\mathrm{PM}} + \frac{\widehat{H}_{\mathrm{t}} h_{\mathrm{s}} + \widehat{H}_{\mathrm{y}} \frac{\pi D_{\mathrm{m}}}{2p}}{\frac{\widehat{B}_{\delta}}{\mu_0}}. \tag{1.20}$$

By substituting Eq. (1.20) into Eq. (1.19), a better approximation of the magnetizing inductance L'_{m} will be obtained for the actual non-ideal iron

$$L'_{\mathrm{m}} = \mu_0 \frac{m D_{\mathrm{o}}}{4\pi p^2 \delta_{\mathrm{ef}}} (1 - k^2)(k_{\mathrm{w}} N)^2. \tag{1.21}$$

Slot leakage inductance

As the slot becomes deeper and the tangential stress increases, the slot leakage flux appears to be more relevant to the torque production. In an ideal case, all the stator current is used to produce mutual flux; on the other hand, in a slotted configuration, the stator current produces a flux component that is not linked by the rotor magnetic circuit. This effect degrades the torque capacity of the machine compared with an ideal case.

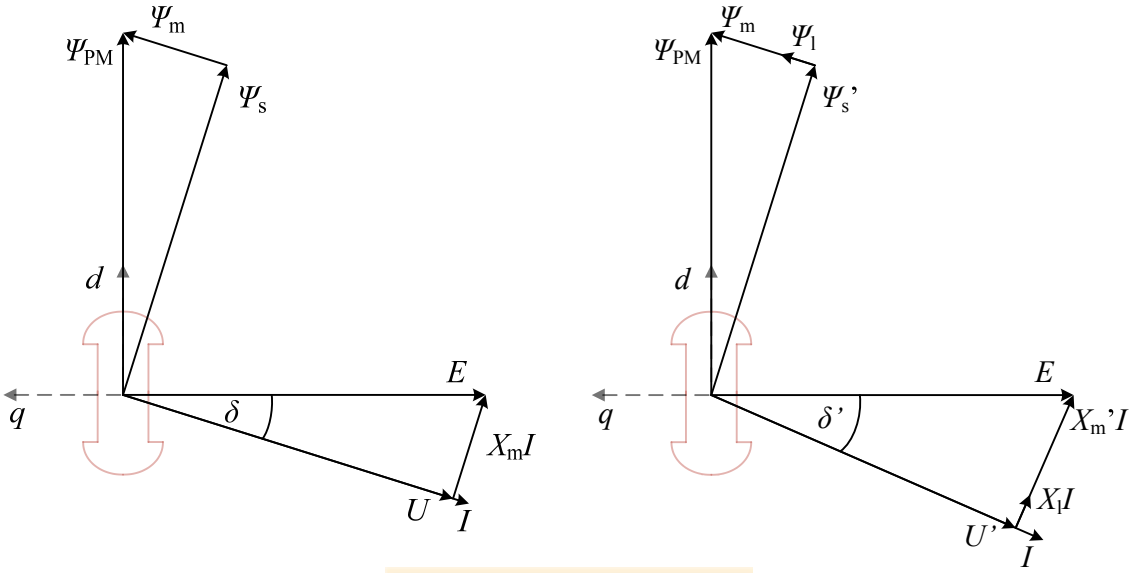

a) b)

Fig. 1.11. Phasor diagram of the synchronous generator with E = 1 p.u., I = 1 p.u. for a) an ideal case with U = 0.95 p.u., L_m = 0.3 p.u., L_l = 0 p.u., and for b) a non-ideal case with U = 0.92 p.u., L_m = 0.29 p.u., L_l = 0.11 p.u. (Source: own elaboration)

The slot leakage inductance for a rectangular slot is given by (Kim, Choi, and Sarlioglu, 2016)

$$L_u = \mu_0 \frac{N^2 l_e h_s}{3 b_s}, \tag{1.22}$$

where the radial stator length is

$$l_e = \frac{D_o(1-k)}{2}. \tag{1.23}$$

Torque angle

The torque expression given by Eq. (1.9) can be written in RMS values of the line current and the induced voltage with the load angle δ as

$$T = m \frac{p}{\omega_s} EI \cos\delta, \tag{1.24}$$

where the angle δ can be determined by the phasor diagram of the axial flux machine, considering the ideal and non-ideal cases for a given operating point as shown in Fig. 1.11. Based on Fig. 1.11(a), the ideal torque angle is

$$\delta = \tan^{-1}\left(\frac{\omega_s L_m I}{U}\right). \tag{1.25}$$

On the other hand, in order to include the non-linear effect of the iron and stator teeth leakage flux, the non-ideal torque angle according to Fig. 1.11(b) is written as

$$\delta' = \tan^{-1}\left(\frac{\omega_s (L'_m + L_l) I_{rms}}{U'}\right). \tag{1.26}$$

Torque correction factor

As was described in the previous sections, the analysis of non-ideal cases removes several of the initial assumptions, which leads to a closer result in the torque estimation. The corrected expression for the electromagnetic torque can be written as

$$T' = m\frac{p}{\omega_s} E' I \cos\delta'. \tag{1.27}$$

By taking the ratio between Eq. (1.27) and Eq. (1.24), a correction factor for the ideal torque calculation becomes

$$T' = K_{trq} T, \tag{1.28}$$

where

$$K_{trq} = \left(\frac{h_{PM}}{\cos\delta}\right)\left(\frac{\cos\delta'}{h'_{PM}}\right). \tag{1.29}$$

The first component of Eq. (1.29) is obtained from the ideal torque expression, which is given in terms of tangential stress, magnet properties, and outer diameter. Further, the second component is obtained from the resultant machine geometry and iron characteristics. By taking this approach, torque estimation is calculated directly in an analytical way. In the next section, a finite element analysis is carried out to validate the proposed correction.

Finite element analysis

A three-dimensional (3D) finite element analysis (FEA) is carried out to determine the flux density distribution. This enables a better estimation of the developed electromagnetic torque. The flux density distributions for no-load and load conditions of a section of the two-pole machine are depicted in Fig. 1.12 to Fig. 1.14 for 20 kPa, 40 kPa, and 80 kPa, respectively.

The geometric dimensions were obtained from the previous model considering the design data of Table 1.1 and different values of tangential stress.

At low tangential stress values, the flux density distributions for no-load and load conditions are similar (see Fig. 1.12) because of a low armature reaction effect and leakage flux. Thus, the ideal torque estimation given by Eq. (1.9) is close to the FE torque estimation. However, as the tangential stress value increases, the magnetic reluctance increases with the iron reluctance (and saturation) as shown in Fig. 1.13. In this case, the torque estimation given by Eq. (1.9) is not good enough. This effect is most evident for high tangential stress values, where the values of magnetic flux density are greater as shown in Fig. 1.14. Additionally, the structures of the rotor yoke and the stator also become saturated.

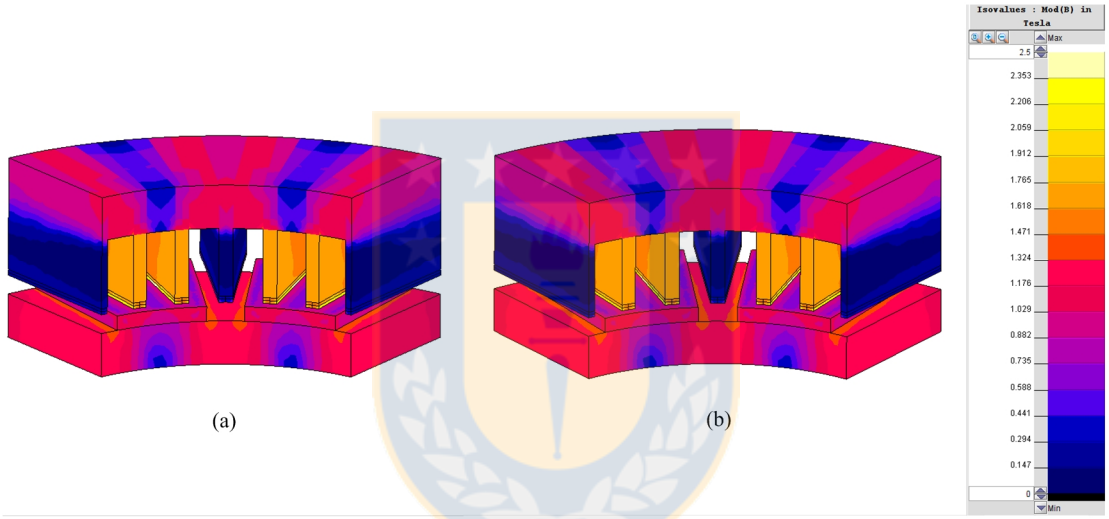

Fig. 1.12. Flux density distribution for σ_{Ftan} = 20 kPa; a) no-load, b) on-load. (Jara et al., 2014)

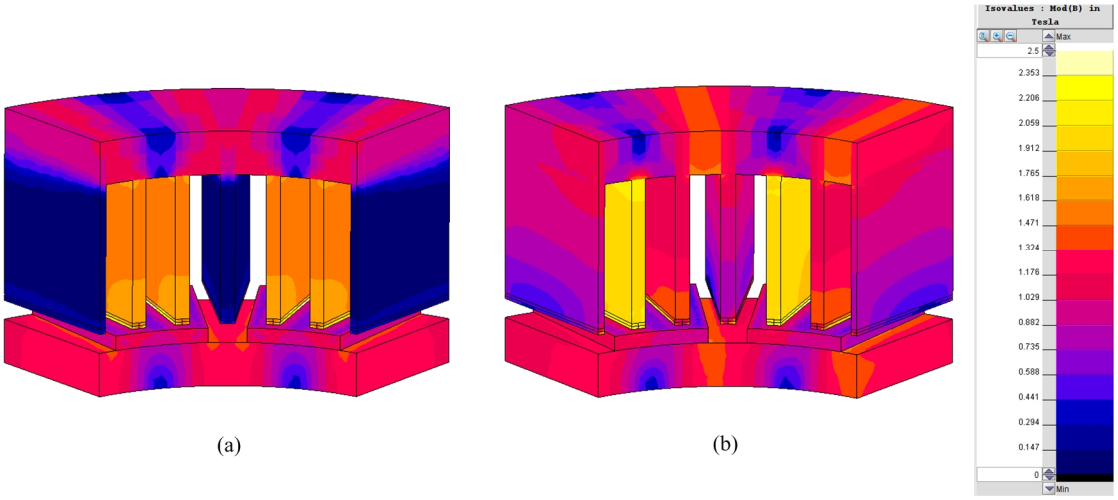

Fig. 1.13. Flux density distribution for σ_{Ftan} = 40 kPa; a) no-load, b) on-load. (Jara et al., 2014)

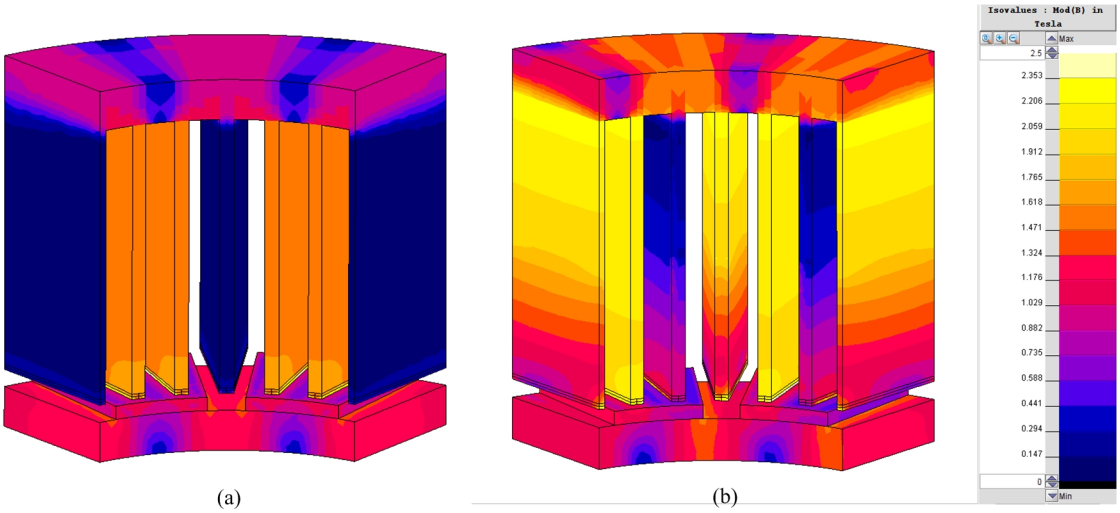

Fig. 1.14. Flux density distribution for $\sigma_{\mathrm{Ftan}} = 80$ kPa; a) no-load, b) on-load. (Jara et al., 2014)

A comparison between the ideal and non-ideal cases of torque estimation by using Eqs. (1.9) and (1.28) and the FEA results is illustrated in Fig. 1.15.

As expected, a direct proportional variation of torque is presented by Eq. (1.9), which deviates significantly from the FEA results as the tangential stress increases. At low σ_{Ftan}, both torque estimations are similar, since the stator teeth are short with a minimum effect of saturation and leakage flux. As the σ_{Ftan} increases, these effects become more

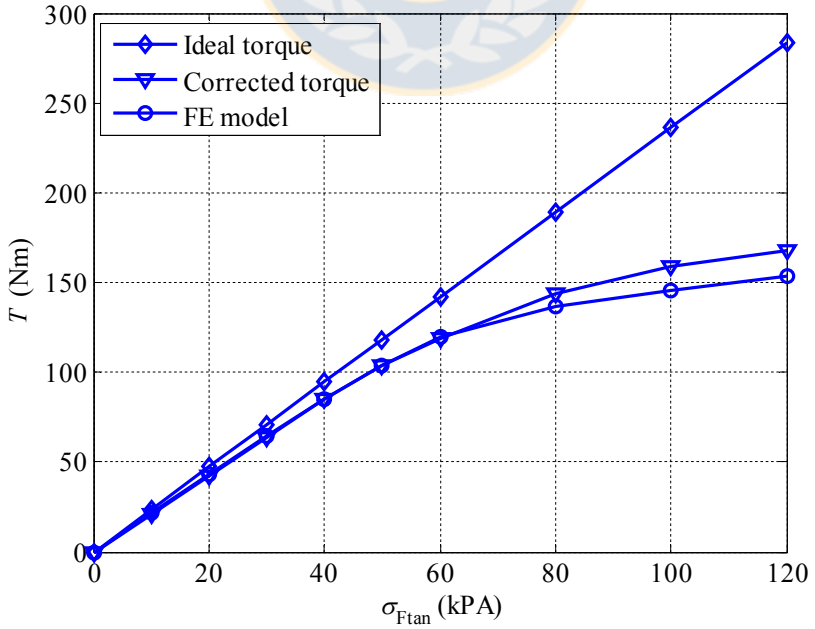

Fig. 1.15. Comparison of torque calculation based on ideal and non-ideal cases and the FEA. (Jara et al., 2014)

important with a continuous increment between the results. On the other hand, the corrected value of the torque estimation calculated by Eq. (1.28) results in a better estimation compared with the FEA results. Since Eq. (1.28) takes into account both the leakage flux and iron saturation, the geometric variation is traced in a better manner as the tangential stress increases. For extremely high values of tangential stress, Eq. (1.28) is in disagreement with the FEA calculation but still provides an improved approximation for the torque compared with Eq. (1.9). This difference may be due to magnetic phenomena not considered in the calculation of the flux density in the magnetic circuit; these phenomena are described below.

1.5 Slot leakage flux

According to the load condition depicted from Fig. 1.12(b) to Fig. 1.14(b), the magnetic flux distribution in different teeth is asymmetrical. This asymmetry can be explained by analyzing the magnetic flux distribution shown in Fig. 1.16. The dashed line indicates the magnetic flux produced by the slot current considering a distributed winding (DW) with $q = 1$, while the solid line in the air gap represents the magnetic flux imposed by the PM.

For teeth 1-4-1, the magnetic flux density is given mainly by adding the leakage flux produced by adjacent slots. In teeth 2-5, the leakage flux produced by adjacent slots is not cancelled out completely, and the resultant is added to the flux imposed by the PM. In teeth 3-6, the resultant component of the leakage flux produced by the slot current is in the opposite direction to the flux produced by the PM, and therefore, the leakage flux is subtracted to the PM flux. This could cause a greater magnetic voltage drop in the teeth, and consequently, a decrease in the torque developed by the machine.

A similar analysis can be made for an AFPM machine with a tooth-coil winding. It is expected that depending on the winding configuration, the developed torque can be increased or decreased.

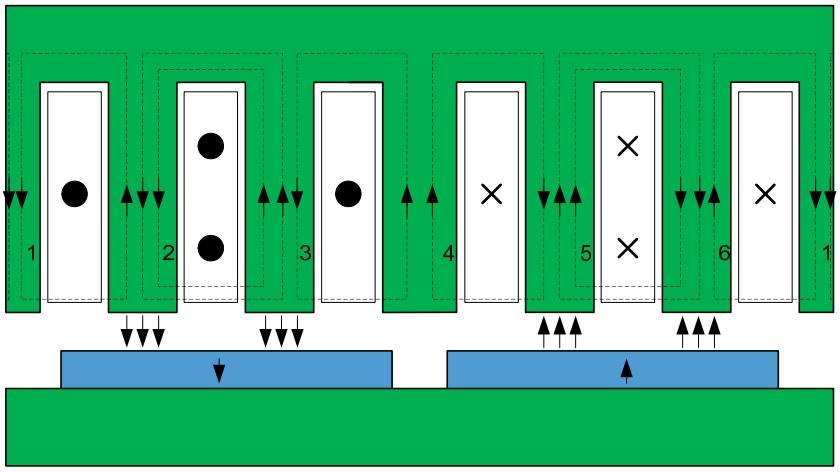

Fig. 1.16. Magnetic flux distribution of the winding (armature reaction) and the permanent magnet. (Source: own elaboration)

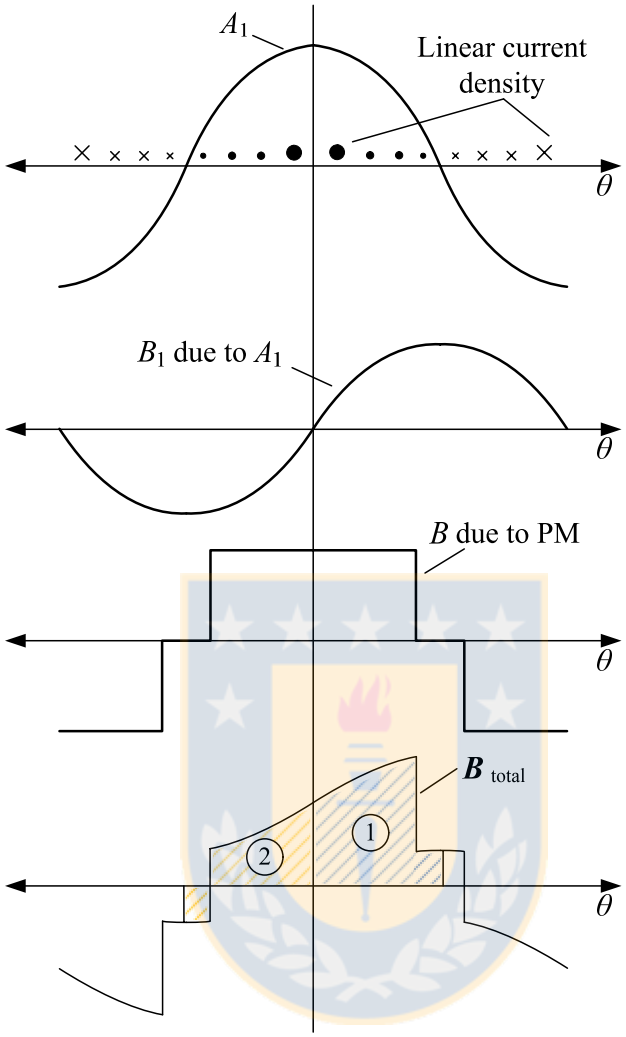

Fig. 1.17. Air-gap magnetic flux density produced by the stator winding linear current density fundamental and the permanent magnets, and the total air-gap magnetic flux density. (Source: own elaboration)

1.6 Effect of armature reaction

The distribution of stator currents generates a magnetic field of its own. In some parts of the air gap, the magnetic field is added to the magnetic field produced by the magnets, and in other parts it is subtracted as shown in Fig. 1.17.

An increase or decrease in the air-gap flux produced by the slot current can be calculated from Ampère's law and considering the permanent magnet demagnetized.

The variation in the flux density in the air gap will produce a higher saturation of the teeth facing the area 1 (dashed in blue) and demagnetization in the teeth facing the area 2

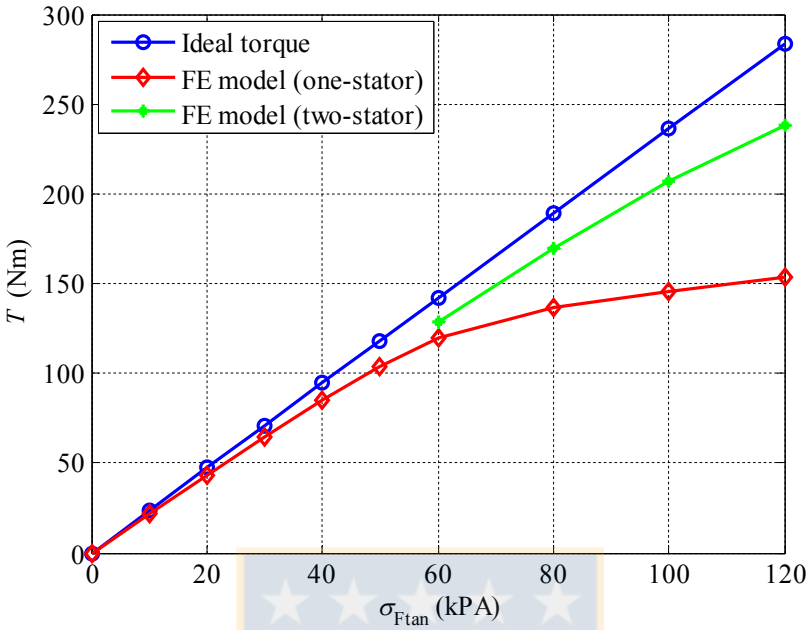

Fig. 1.18. FE comparison of the torque production of a one-stator one-rotor and a two-stator one-rotor AFPM machine. (Source: own elaboration)

(dashed in orange) as shown in Fig. 1.17. This will result in a greater magnetic voltage drop in the magnetic circuit thereby degrading the torque capability of the machine. In (Jara et al., 2014), an analysis is presented of the torque estimation in an AFPM machine with a DW taking into account the effect of slot leakage and armature reaction considering a one-dimensional model of the air-gap flux density, whereas in (Jara et al., 2015), the model is implemented considering the two-dimensional model presented in Chapter 2. To implement the torque correction factor in a machine with the TCW, the author recommends the use of a reluctance network because of the complexity of the flux paths (Gerada et al., 2005; Rottach et al., 2012).

1.7 Selecting the number of stators

In the literature review, it has been observed that the selection of the number of rotors and stators is mainly based on mechanical requirements. However, in the course of the dissertation work, it was observed that the selection of the number of stators significantly affects the torque capability of the machine. A comparison between the torque developed by a one-stator one-rotor and a two-stator one-rotor for the previous design example is shown in Fig. 1.18. The volume of slots is the same in both cases.

For tangential stress values below 60 kPA, both configurations produce a similar torque. However, for high values of tangential stress, the difference increases considerably. For 120 kPA, the difference between both configurations is close to 90 Nm.

1.8 Outline of the doctoral dissertation

This doctoral dissertation focuses on developing design strategies for AFPM machines with a distributed winding (DW) and a tooth coil winding (TCW). With these strategies it will be possible to set different design characteristics, such as geometrical dimensions, number of stators and rotors, magnetic induction levels, electrical circuit characteristics, and operating waveforms for a given application.

The first chapter introduces the design equation for dimensioning an axial flux permanent magnet machine as a function of tangential stress, external diameter, and diameter ratio, where an idealized expression for torque has been developed. Then, with the introduction of a torque correction factor, non-ideal parameters such as the iron saturation and the stator leakage flux can be included. The established model allows to obtain the main geometrical dimensions of the machine as a function of magnetic and electric load considered in the design. Optimization is carried out for the maximum developed torque. The torque correction factor will also make it possible to evaluate the effect of armature reaction and slot leakage fluxes produced by the winding on the torque capability of an axial flux machine. Further, the torque correction factor will allow to evaluate and decide quickly and accurately the tangential stress value at which it is convenient to use more than one stator in order to optimize the torque produced by the machine.

The second chapter addresses the 2D modelling of the air-gap flux density distribution. The model consists of a linear representation of the axial flux machine at a given diameter. The presented magnetic field equations for the armature reaction can be used in a DW and a TCW. The main advantage is the simplicity of the model, which facilitates its implementation to any kinds of windings.

The third chapter provides inductance equations for the axial flux machine. These equations are generalized and can be used in a DW and a TCW. The equations of the slot leakage inductance and the tooth tip leakage inductance are written as a function of number of slots per pole and phase, pole pitch expressed in the number of slots, and the coil pitch expressed in the number of slots resulting in the traditional expression used to determine the leakage inductance in a DW.

The fourth chapter presents the loss calculation in a two-stator one-rotor axial flux machine and the eddy current loss reduction of permanent magnets for low-speed applications. A new rotor structure is described and analysed, and its impact on the loss reduction is validated in a 100 kW machine prototype.

The conclusions and suggestions for future work are presented in Chapter 5.

1.9 Scientific contributions

The design of axial flux permanent magnet machines, and in general terms, the design of rotating electrical machines is a process that involves different engineering areas, such as

electromagnetism, mechanics, and fluid dynamics, which have to be combined for a proper final product. A fast and accurate dimensioning of the machine to achieve the requirements of the applications is the first step of an iterative process, which is repeated until a suitable solution is achieved.

This doctoral dissertation presents the following scientific contributions:

- A procedure for the electromagnetic design of AFPM machines with either a distributed winding or a tooth coil winding. Compared with similar design tools, the main contribution of the proposed analytical model is its simplicity with a relatively good accuracy, which allows to take into account the non-ideal phenomena in the dimensioning of the machine.

- A 2D analytical model is introduced to determine the air-gap flux density distribution of an AFPM machine. This model can be used in both DW and TCW to make a more accurate analysis of the electrical variables and waveforms.

- A new 2D analytical model is established to determine the air-gap flux density distribution produced by the stator currents. The model is based on the scalar magnetic potential and the star of slots theory.

- Analytic equations are developed to determine the leakage inductance components with the TCW either with vertical coils or horizontal coils. A generalized expression is derived to determine the slot leakage inductance with the TCW from $q = 0.25$ to $q = 0.5$ based on the number of slots per pole and phase, the coil pitch expressed in the number of slots, and the pole pitch expressed in the number of slots. This expression simplifies the computations of the leakage inductance. The equations can also be used in the DW. The slot leakage inductance equations with vertical coils and a horizontal coil distribution are compared showing the values for different slot and pole combinations.

- A detailed 2D finite element analysis and optimization of a new rotor structure are proposed to reduce the eddy current losses induced in the permanent magnets of one-stator two-rotor AFPM machines with a tooth coil winding and an open slot structure. The additional benefits to the torque production are also analysed.

- The effects on manufacturing of the steel lamination layer used in the proposed rotor structure are studied with the conclusion that an alternative joining procedure will be designed to avoid additional losses.

- The results of the numerical computations are validated with a 100 kW machine prototype.

2 Air-gap magnetic field

2.1 Introduction

The air-gap magnetic field that consists of the PM magnetic field and the armature reaction magnetic field must be estimated by the solution of Maxwell's equation. If the induced eddy current is neglected, the scalar magnetic potential can be used to simplify the mathematical solution.

A general analytic solution of the magnetic field for slotted RFPM machines was presented in (Zhu et al., 1993). The authors show that it is possible to estimate the radial component magnetic field produced by radially magnetized PMs and the current slot with a good accuracy. The slotting effect is taken into account by a permeance function (Zhu et al. part III, 1993). This technique was extended in (Zhu et al., 2002) to PMs with parallel magnetization. The analytic equations are easy to implement and the computation time is short. However, the applied permeance function fails in the prediction of the tangential component of the magnetic field. The authors of (Zarko et al., 2006) present a complex permeance function, which shows a good accuracy for the computation of both the radial and tangential components of the air-gap magnetic field for RFPM machines. A similar complex permeance function is presented in (Hemeida and Sergeant, 2014) for AFPM machines. On the other hand, this complex permeance equation consumes a lot of computation time as it is necessary to find a numerical solution for each point of the air gap in the tangential component. In the case of AFPM machines, linear representations of the magnetic field are preferred (Chan et al., 2009; Tiegna et al. 2012; Hemeida and Sergeant, 2014, Jara et al., 2015) because of their low computation time and complexity instead of the quasi 3D analytical model (Azzouzi et al., 2005). In this doctoral dissertation, a linear representation is used to estimate the air-gap magnetic field and the permeance function presented in (Zhu et al., part III, 1993) giving priority to the simplicity of the analytic model.

2.2 Slotless permanent magnet magnetic field

The tangential (x-direction) and axial (y-direction) components of the flux density distribution in the air gap produced by the permanent magnets (PM) for an axial flux machine considered as a linear machine as shown in Fig. 2.1 are given by (Chan et al., 2009).

$$B_{\mathrm{xI}} = \mu_0 \sum_{n=1,3,5\ldots}^{\infty} \frac{M_n}{a_n} \sinh\frac{n\pi h_{\mathrm{PM}}}{\tau_{\mathrm{p}}} \sinh\frac{n\pi(\delta_{\mathrm{PM}} - y)}{\tau_{\mathrm{p}}} \sin\frac{n\pi x}{\tau_{\mathrm{p}}} \tag{2.1}$$

$$B_{\mathrm{yI}} = \mu_0 \sum_{n=1,3,5\ldots}^{\infty} \frac{M_n}{a_n} \sinh\frac{n\pi h_{\mathrm{PM}}}{\tau_{\mathrm{p}}} \cosh\frac{n\pi(\delta_{\mathrm{PM}} - y)}{\tau_{\mathrm{p}}} \cos\frac{n\pi x}{\tau_{\mathrm{p}}} \tag{2.2}$$

$$B_{\mathrm{xII}} = \mu_{\mathrm{r,PM}} \sum_{n=1,3,5}^{\infty} \frac{M_n}{a_n} \sinh\frac{n\pi(\delta_{\mathrm{PM}} - h_{\mathrm{PM}})}{\tau_{\mathrm{p}}} \sinh\frac{n\pi y}{\tau_{\mathrm{p}}} \sin\frac{n\pi x}{\tau_{\mathrm{p}}} \tag{2.3}$$

$$B_{\mathrm{yII}} = \mu_0 \sum_{n=1,3,5}^{\infty} \frac{M_n}{a_n} \left[a_n - \mu_{\mathrm{r}} \sinh\frac{n\pi(\delta_{\mathrm{PM}} - h_{\mathrm{PM}})}{\tau_{\mathrm{p}}} \cosh\frac{n\pi y}{\tau_{\mathrm{p}}}\right] \cos\frac{n\pi x}{\tau_{\mathrm{p}}}, \tag{2.4}$$

where a_{n} is defined as

$$a_n = \cosh\frac{n\pi(\delta_{\mathrm{PM}} - h_{\mathrm{PM}})}{\tau_{\mathrm{p}}} \sinh\frac{n\pi h_{\mathrm{PM}}}{\tau_{\mathrm{p}}} + \mu_{\mathrm{r}} \sinh\frac{n\pi(\delta_{\mathrm{PM}} - h_{\mathrm{PM}})}{\tau_{\mathrm{p}}} \cosh\frac{n\pi h_{\mathrm{PM}}}{\tau_{\mathrm{p}}} \tag{2.5}$$

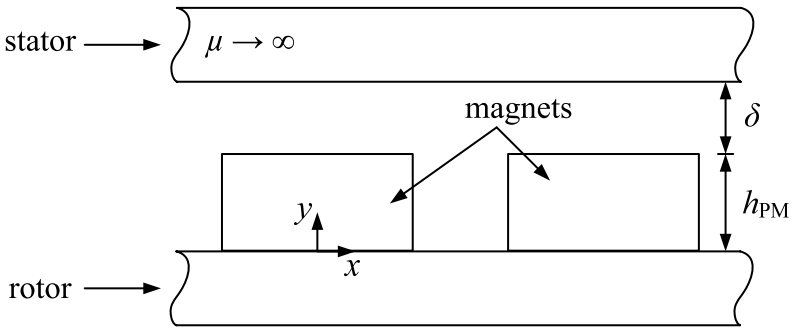

Fig. 2.1. Model for the computation of the permanent magnet magnetic field considering a cutting plane at the mean diameter. (Source: own elaboration)

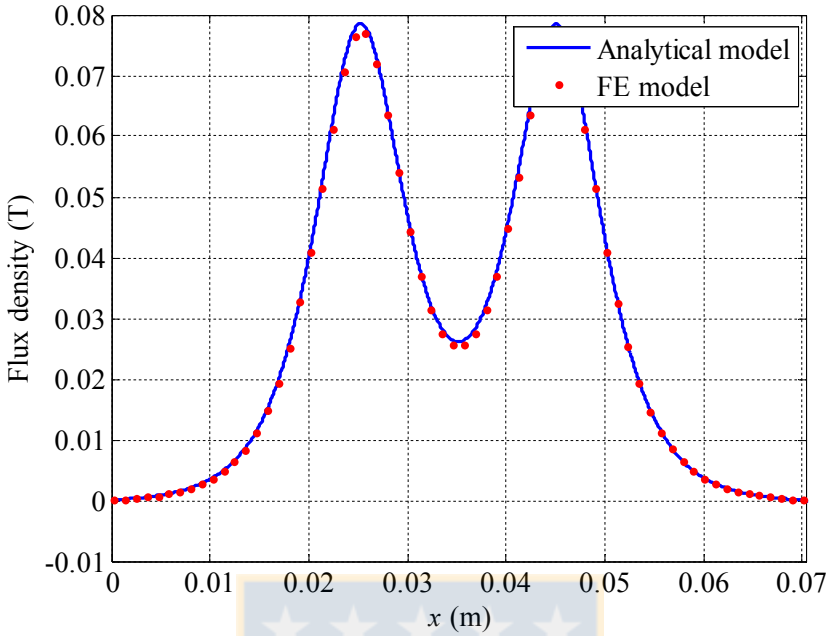

(a)

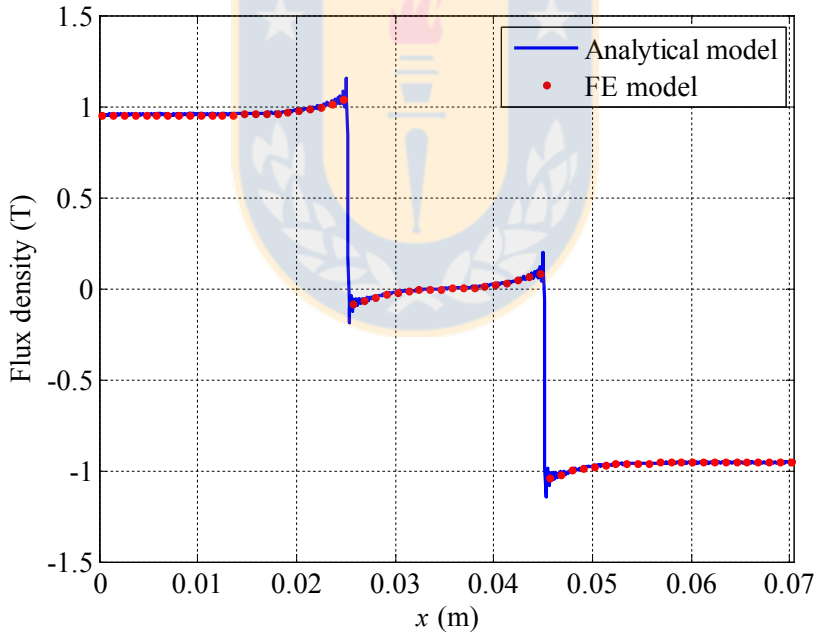

(b)

Fig. 2.2. No-load flux density distribution in the permanent magnet region computed by the analytical method for $y = h_{PM}/2$, where $h_{PM} = 7.5$ mm and $\delta = 2.5$ mm; (a) tangential component, (b) axial component. (Source: own elaboration)

and M_n is the magnetization of the PM given by

$$M_n = 2\frac{B_\mathrm{r}\alpha_\mathrm{PM}}{\mu_0}\frac{\sin\frac{n\pi\alpha_\mathrm{PM}}{2}}{\frac{n\pi\alpha_\mathrm{PM}}{2}}. \tag{2.6}$$

Fig. 2.2 and Fig. 2.3 illustrate the tangential and axial components of the flux density distribution at different heights of the air-gap region for a 12-slot 10-pole machine. The mean diameter of the machine is 284 mm, and the relative permanent magnet width is equal to 0.72. A good agreement with the FE results can be observed.

2.3 Slotless armature reaction field

The armature reaction field can be derived from the scalar magnetic potential following a similar procedure as presented in (Chan et al., 2009). The representation of one coil phase (phase U) by means of an equivalent armature current sheet is shown in Fig. 2.4(a).

A Fourier expansion of the linear current density A (see Fig. 2.4(b)) produced by a single coil of N_slot turns, carrying a current I, a slot opening width b_0, and a coil pitch τ_c is given by

$$A = \sum_{u=1}^{\infty}\frac{4iz_\mathrm{Q}}{u\pi b_0}\sin\left(\frac{ub_0}{2r_\mathrm{m}}\right)\sin\left(\frac{u\tau_\mathrm{c}}{2r_\mathrm{m}}\right)\sin\left(\frac{ux}{r_\mathrm{m}}\right). \tag{2.7}$$

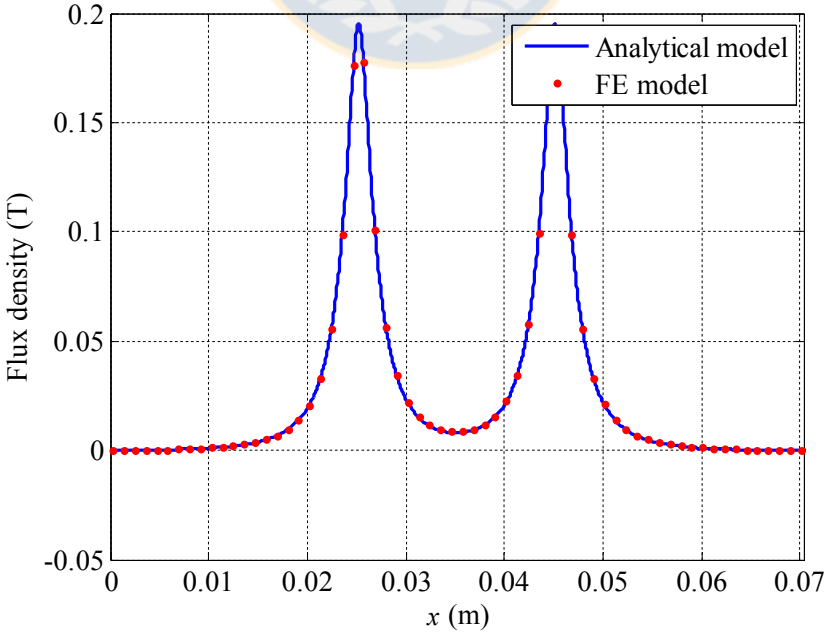

(a)

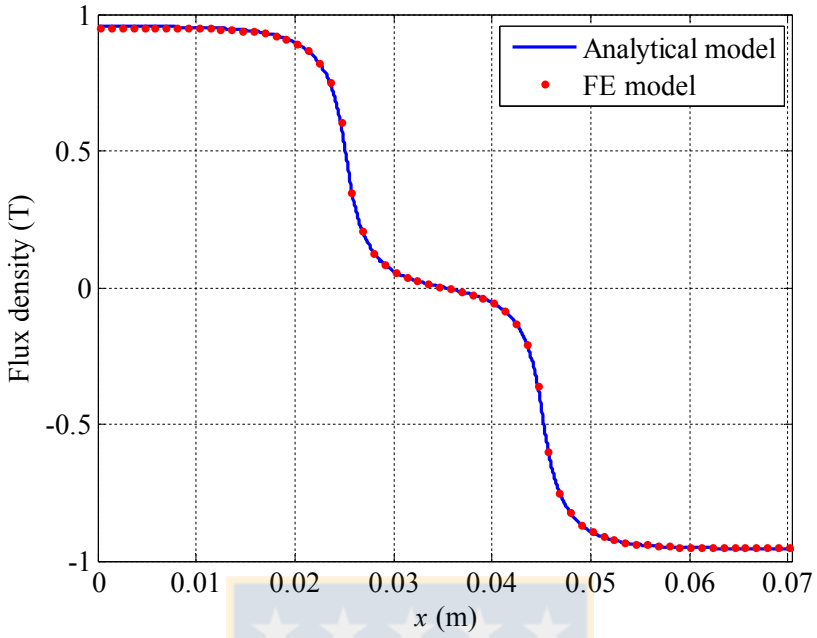

(b)

Fig. 2.3. No-load flux density distribution in the air-gap region computed by the analytical method for $y = h_{PM} + \delta/2$, where h_{PM} = 7.5 mm and δ = 2.5 mm; (a) tangential component, (b) axial component. (Source: own elaboration)

The scalar magnetic potential resulting from the current is described by Laplace's equation in rectangular coordinates. Because the current density only contains sine terms, the scalar magnetic potential in the air gap is thus

$$\varphi(x,y) = \sum_{u=1}^{\infty} \left(C_1 e^{\frac{uy}{2r_m}} + C_2 e^{-\frac{uy}{2r_m}} \right) \cos\left(\frac{ux}{r_m}\right). \tag{2.8}$$

The boundary conditions to be satisfied are

$$H_x|_{y=0} = 0 \tag{2.9}$$

$$H_x|_{y=\delta_{PM}} = -A\,. \tag{2.10}$$

By using Eqs. (2.7) to (2.10), the tangential and normal components of the air-gap flux density produced by the current of one coil phase are given by

$$B_x = -\mu_0 \sum_{u=1,2,3\ldots}^{\infty} a_u b_u \, k_{pu} \sinh\frac{uy}{r_m} \sin\frac{ux}{r_m} \tag{2.11}$$

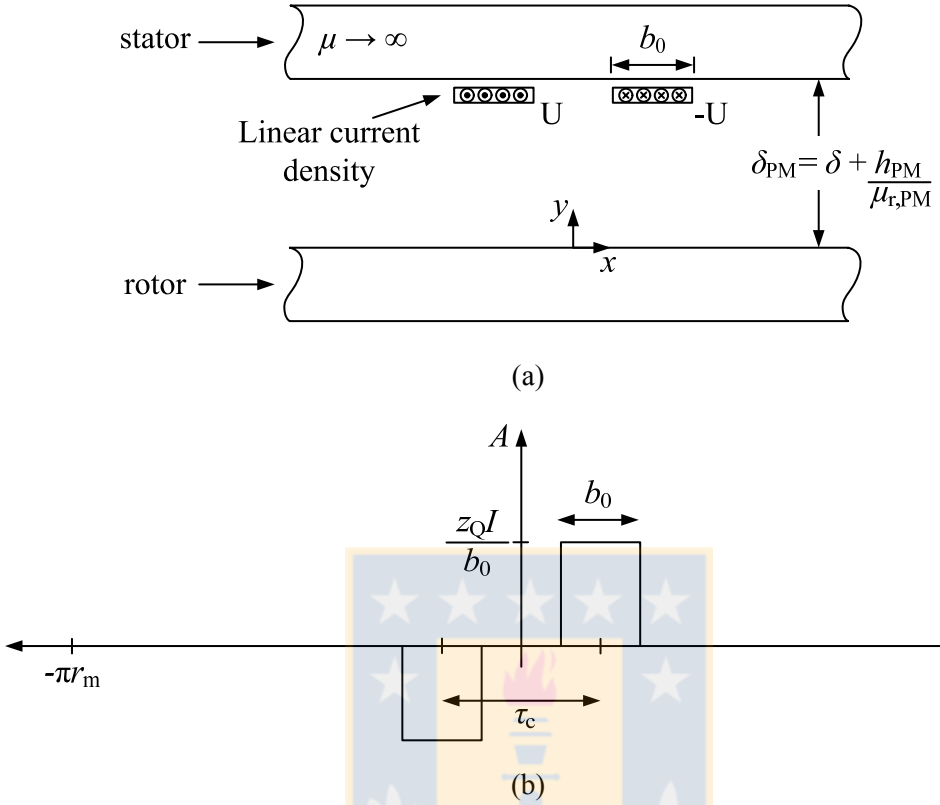

Fig. 2.4. Model for the computation of the armature reaction field; (a) cutting plane at the mean diameter, (b) current density waveform. (Source: own elaboration)

$$B_y = \mu_0 \sum_{u=1,2,3\ldots}^{\infty} a_u b_u k_{pu} \cosh\frac{uy}{r_m} \cos\frac{ux}{r_m}, \tag{2.12}$$

where

$$a_u = \frac{1}{\sinh\frac{u\delta_{PM}}{r_m}} \tag{2.13}$$

$$b_u = 2N_{slot} I \frac{\sin\frac{ub_0}{2r_m}}{\frac{u\pi b_0}{2}} \tag{2.14}$$

$$k_{pu} = \sin\left(\frac{u\tau_c}{2r_m}\right). \tag{2.15}$$

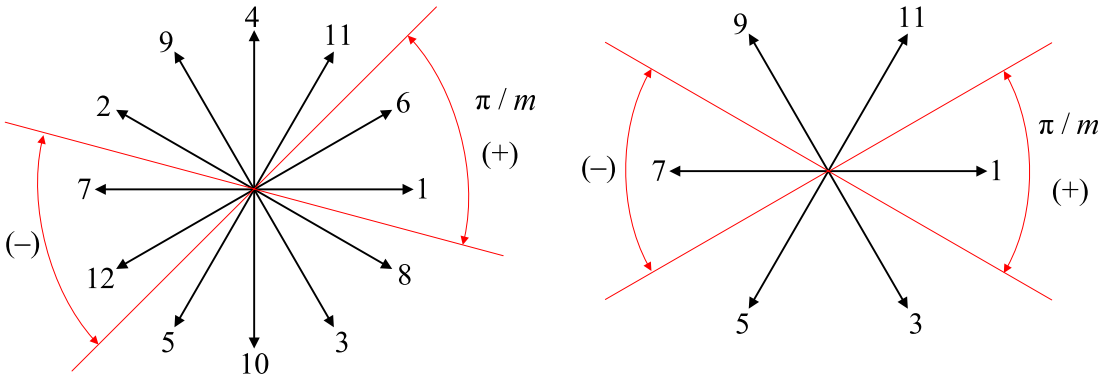

(a) (b)

Fig. 2.5. Voltage phasor graph for the main harmonic order (HO) of the 12-slot 10-pole machine; a) with the DL winding, b) with the SL winding. (Source: own elaboration)

In order to derive the air-gap flux density distribution for a given phase, it is necessary know the winding arrangement. It can be determined based on the of star slots theory

$$B_{\mathrm{x}} = -\mu_0 \sum_{S_1} S_2 \sum_{u=1,2,3\ldots}^{\infty} a_u b_u \, k_{\mathrm{pu}} \sinh\left(\frac{uy}{r_{\mathrm{m}}}\right) \sin\left[\frac{u}{r_{\mathrm{m}}}(x - S_1 \tau_{\mathrm{s}})\right] \tag{2.16}$$

$$B_{\mathrm{y}} = \mu_0 \sum_{S_1} S_2 \sum_{u=1,2,3\ldots}^{\infty} a_u b_u \, k_{\mathrm{pu}} \cosh\left(\frac{uy}{r_{\mathrm{m}}}\right) \cos\left[\frac{u}{r_{\mathrm{m}}}(x - S_1 \tau_{\mathrm{s}})\right], \tag{2.17}$$

where S_1 and S_2 are vectors related to the position and sign of a given phase coil. This expression can be applied either to the DW, DL-TCW, or SL-TCW. For instance, Eqs. (2.16), (2.11), and (2.17) are used to find the tangential and normal components of the air-gap flux density for a 12-slot 10-pole machine with a DL winding (q = 0.4) and a 12-slot 10-pole machine with a single-layer winding (q = 0.4). The results for the DW are reported in (Jara et al., 2015).

For the 12-slot 10-pole machine with the DL and SL, the star of slots is shown in Fig. 2.5(a) and Fig. 2.5(b). The respective vectors S_1 and S_2 for DL winding are

$$S_1 = [1\ 6\ 7\ 12] \quad ; \quad S_2 = [1\ 1 - 1 - 1]$$

By substituting the vectors S_1 and S_2 into Eqs. (2.16) and (2.17), the tangential and axial components of the air-gap flux density are obtained as shown in Fig. 2.6.

For the 12-slot 10-pole machine with the SL, the respective vectors S_1 and S_2 are

$$S_1 = [1\ \ 7] \qquad ; \qquad S_2 = [1 - 1]$$

and the air-gap flux density prediction is shown in Fig. 2.7.

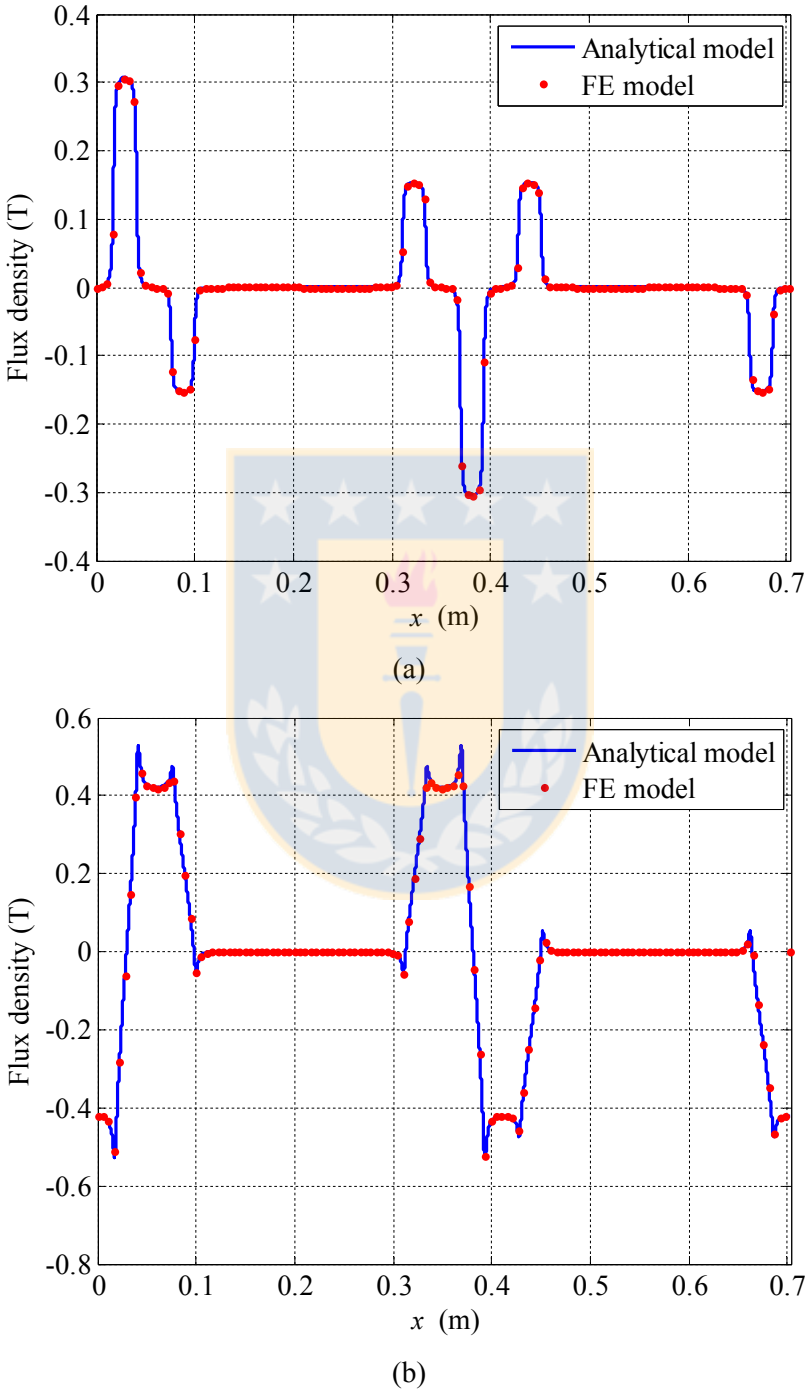

Fig. 2.6. Flux density distribution for the armature reaction of the 12-slot 10-pole machine with the DL winding at the middle of the air gap computed by the analytical method; (a) tangential component, (b) axial component. (Source: own elaboration)

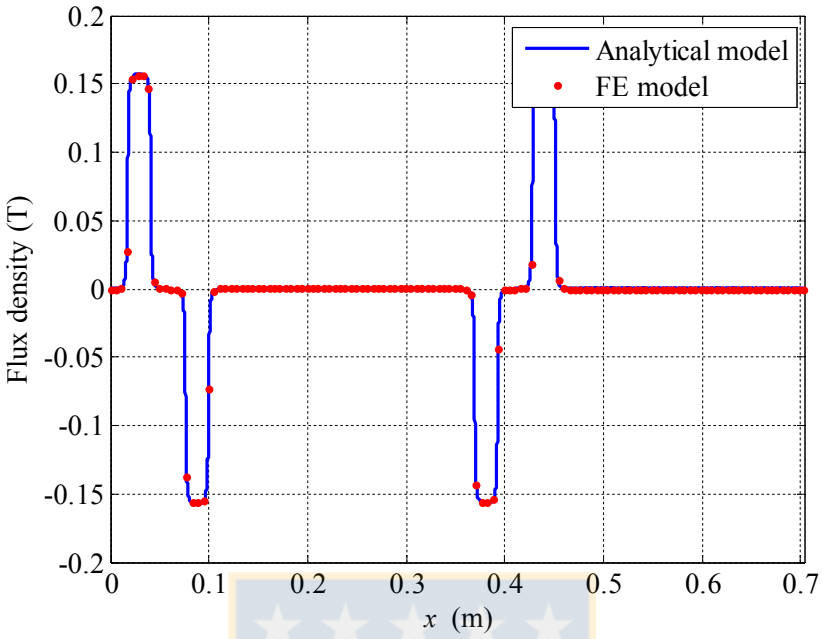

(a)

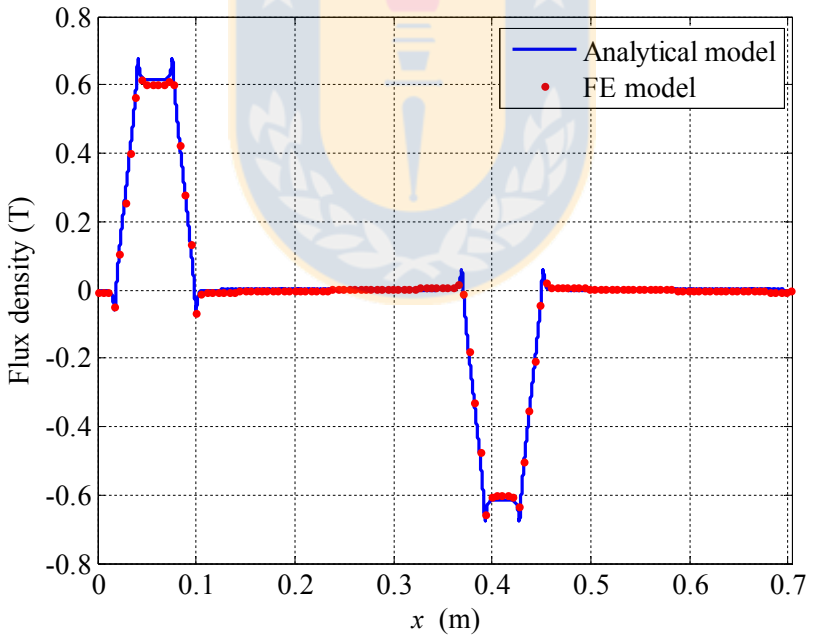

(b)

Fig. 2.7. Flux density distribution for the armature reaction of the 12-slot 10-pole machine with the SL winding in the middle of the air gap computed by the analytical method; (a) tangential component, (b) axial component. (Source: own elaboration)

For a three-phase winding supply with balanced current, the air-gap magnetic field for

phases U, V, and W can be found by substituting I in Eqs. (2.16) and (2.17) by $I_{\mathrm{u}} = \hat{I}\cos(\omega_{\mathrm{r}}t)$, $I_{\mathrm{v}} = \hat{I}\cos(\omega_{\mathrm{r}}t - 2\pi/3)$ and $I_{\mathrm{w}} = \hat{I}\cos(\omega_{\mathrm{r}}t - 4\pi/3)$, respectively.

2.4 Relative permeance function

The relative permeance of the slotted air-gap/magnet region can be calculated by the conformal transformation method presented in (Zhu and Howe, 1993). Considering the linear model shown in Fig. 2.1(a), the permeance function can be expressed as

$$\tilde{\lambda}(x,y) = \begin{cases} 1 - \beta(y) - \beta(y)\cos\dfrac{\pi}{0.8b_0}x & 0 < x < 0.8b_0 \\ 1 & 0.8b_0 < x < \tau_{\mathrm{s}} \end{cases}, \tag{2.18}$$

where

$$\beta(y) = \frac{1}{2}\left[1 - \frac{1}{\sqrt{1 + \left(\dfrac{b_0}{2\delta_{\mathrm{PM}}}\right)^2 (1+c)}}\right], \tag{2.19}$$

and c is determined from

$$y\frac{\pi}{b_0} = \frac{1}{2}\ln\left(\frac{\sqrt{a^2+c^2}+c}{\sqrt{a^2+c^2}-c}\right) + \frac{2\delta_{\mathrm{PM}}}{b_0}\tan^{-1}\frac{2\delta_{\mathrm{PM}}}{b_0}\frac{c}{\sqrt{a^2+c^2}} \tag{2.20}$$

and

$$a^2 = 1 + \left(\frac{2\delta_{\mathrm{PM}}}{b_0}\right)^2. \tag{2.21}$$

This is expressed in the Fourier series form,

$$\tilde{\lambda}(x,y) = \lambda_0(y) + \sum_{u=1}^{\infty} \lambda_u(y)\cos\frac{u2\pi x}{\tau_{\mathrm{s}}} \tag{2.22}$$

where

$$\lambda_0 = 1 - 1.6\beta(y)b_0/\tau_{\mathrm{s}} \tag{2.23}$$

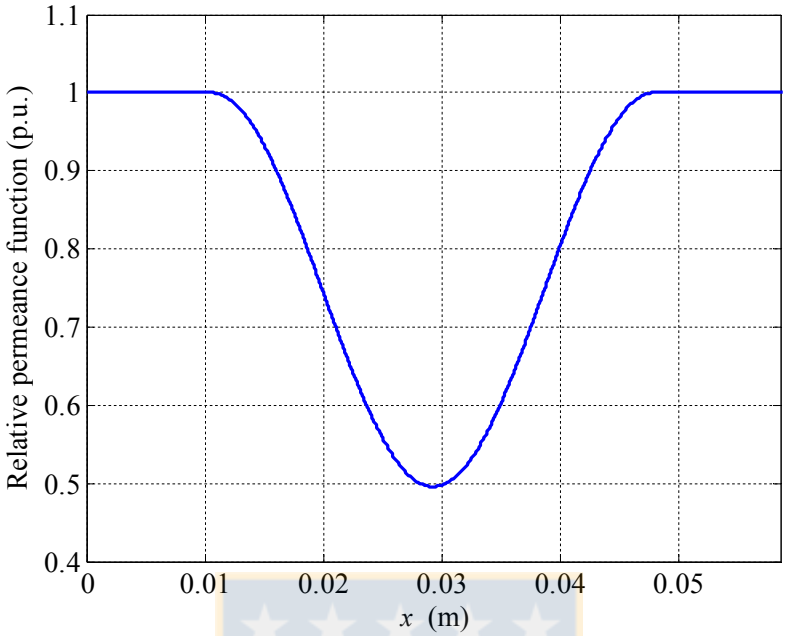

Fig. 2.8. Relative permeance function for one slot pitch of the 12-slot 10-pole machine with b_s = 23.5 mm and G_t = 0.6. (Source: own elaboration)

$$\lambda_u = \frac{4\beta(y)}{u\pi}\left[0.5 + \frac{\left(\frac{u1.6b_0}{\tau_s}\right)^2}{2-2\left(\frac{u1.6b_0}{\tau_s}\right)^2}\right]\sin\left(\frac{u1.6\pi b_0}{\tau_s}\right). \tag{2.24}$$

In Fig. 2.8 the relative permeance function for one slot pitch is shown considering a slot width of 23.5 mm.

2.5 Magnetic field of a slotted PM

The axial component of the magnetic field produced by the PMs in a slotted machine can be calculated as in (Zhu et al., part III, 1993)

$$B_{\mathrm{y,PM}}(x,y) = B_{\mathrm{PM}}(x,y)\tilde{\lambda}(x,r), \tag{2.25}$$

where B_{PM} must be replaced by B_{yI} or B_{yII} depending of the air-gap region, where it is necessary to know the magnetic field. By developing Eq. (2.25), we obtain

$$B_{\mathrm{y,PM}}(x,y) = \lambda_0 \sum_{n=1,3,5}^{\infty} \hat{B}_n \cos\frac{n\pi x}{\tau_p} + \sum_{n=1,3,5}^{\infty}\sum_{u=1}^{\infty} \hat{B}_n\lambda_u \cos\frac{u2\pi x}{\tau_s}\cos\frac{n\pi x}{\tau_p}. \tag{2.26}$$

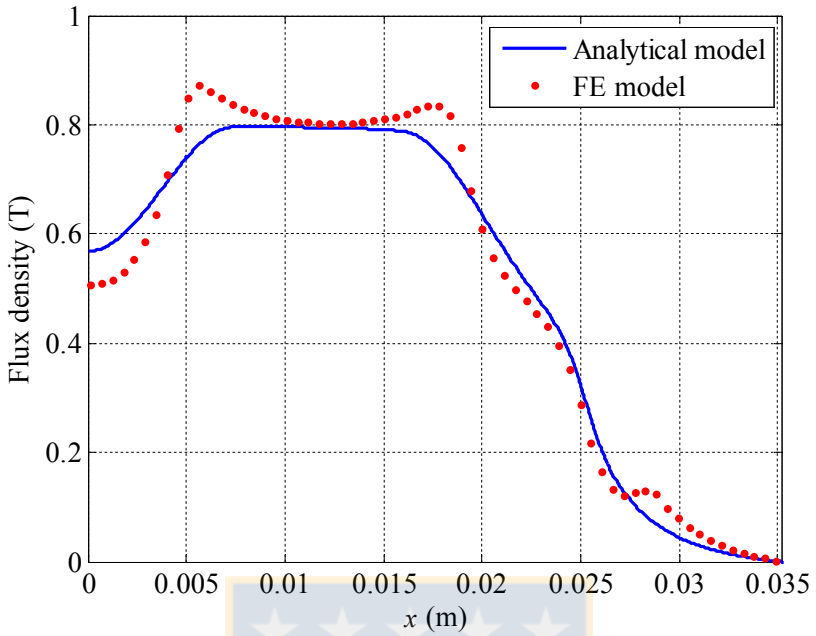

Fig. 2.9. Slotted PM magnetic field in the middle of air gap $y = h_{PM} + \delta/2$ considering $G_t = 0.6$ and the DW. (Source: own elaboration)

As can be seen in Fig. 2.9, prediction of the magnetic field given by Eq. (2.26) shows a good agreement compared with the FE result. However, Eq. (2.26) is somewhat unclear in terms of the orders of the harmonic spectrum. An alternative solution is to apply an FFT algorithm to Eq. (2.25) to obtain the different components of the slotted PM magnetic field, resulting in

$$B_{y,PM}(\theta, y) = \sum_{v}^{\infty} \hat{B}_v \cos(v\theta - \phi_v), \tag{2.27}$$

where $\hat{B}_v$ is the magnitude of the vth harmonic order of the air-gap magnetic field produced by the PM, and ϕ_v is the respective phase angle that assumes the value 0 or π depending on the given harmonic order.

Additionally, it is possible to identify the order of harmonics by means of the machine periodicity t defined as

$$t = \text{G. C. D.}\{Q_s, p\}. \tag{2.28}$$

If the ratio Q_s/t is even, Eq. (2.27) has a quarter-wave symmetry, and consequently, only contains harmonics of odd order multiplied by t. On the other hand, if Q_s/t is odd, Eq. (2.27) contains harmonics of even and odd orders multiplied by t.

In the case of the tangential component of the magnetic field, the permeance function given by Eq. (2.22) does not produce a good prediction, and therefore, a complex permeance function should be used (Zarko et al., 2006).

2.6 Back EMF

The back EMF can be determined using Faraday's law in a single-turn coil considering the magnetic field produced by the PMs at the stator surface (Zhu and Howe, 1993, Zarko et al., 2006).

$$e(t) = -\frac{\mathrm{d}\Phi}{\mathrm{d}t}\bigg|_{y=h_{\mathrm{PM}}+\delta}. \tag{2.29}$$

The magnetic flux Φ can be determined considering the flux density given by Eq. (2.27). It is pointed out that the magnetic field changes with the radial position. For simplicity, the field is calculated at the mean diameter and assuming a constant value with respect to the radial position. This simplification can be removed by dividing the radial length into a finite number i of concentrical rings of length l_e/i as in (Parviainen et al., 2004; Parviainen, 2005; Kurronen and Pyrhönen, 2007; Bianchini et al., 2013).

$$B_{\mathrm{y,PM}}(\theta, t) = \sum_{v}^{\infty} \hat{B}_v \cos[v(\theta - \omega_{\mathrm{r}} t) - \phi_v]\,. \tag{2.30}$$

Integrating Eq. (2.30) across one coil pitch θ_{c}, the expression of magnetic flux becomes

$$\Phi(\theta, t) = \frac{(D_{\mathrm{o}}^2 - D_{\mathrm{i}}^2)}{4} \sum_{v}^{\infty} \frac{\hat{B}_v}{v} k_{\mathrm{p}v} \cos\phi_v \cos v\omega_{\mathrm{r}} t\,, \tag{2.31}$$

where $\cos(\phi_v)$ assumes the value 1 or -1, and $k_{\mathrm{p}v}$ is the winding pitch factor given by

$$k_{\mathrm{p}v} = \sin\left(v\frac{\theta_{\mathrm{c}}}{2}\right). \tag{2.32}$$

Considering Eq. (2.29) and (2.31), the EMF induced in a single-turn coil phase is

$$e(t) = \frac{(D_{\mathrm{o}}^2 - D_{\mathrm{i}}^2)}{4} \omega_{\mathrm{r}} \sum_{v}^{\infty} \cos(\phi_v)\, \hat{B}_v k_{\mathrm{p}v} \cos(v\omega_{\mathrm{r}} t)\,. \tag{2.33}$$

Hence, the induced EMF in a phase winding of N conductors connected in series is obtained as

$$E(t) = \frac{(D_o^2 - D_i^2)}{4} \omega_r N \sum_{v}^{\infty} \cos(\phi_v)\, \hat{B}_v k_{dv} k_{pv} \cos(v\omega_r t), \tag{2.34}$$

where k_{dv} is the distributed factor for the vth harmonic order. By knowing k_{dv} and k_{pv}, the expression of the induced EMF given by Eq. (2.34) can be used in an integer slot distributed winding and a fractional slot concentrated winding.

In Fig. 2.10, a comparison is given of the induced voltage obtained by the analytical model and the 2D finite element model showing a good agreement either with the DW or the TCW winding.

2.7 Winding factor

The winding factor k_w is an important parameter in the electrical machine design as it is directly related to the induced EMF and the electromagnetic torque capability (Magnussen, 2003). Therefore, various authors have put their efforts into determining winding factor expressions for different winding configurations. The winding factor is typically divided into three different factors

$$k_{wv} = k_{pv} k_{dv} k_{sqv}, \tag{2.35}$$

where k_{sqv} is defined as the skewing factor for the vth harmonic order. Skewing is a technique used to reduce the cogging torque (Gonzalez et al., 2007, Letelier et al., 2007; Aydin and Gulec, 2014).

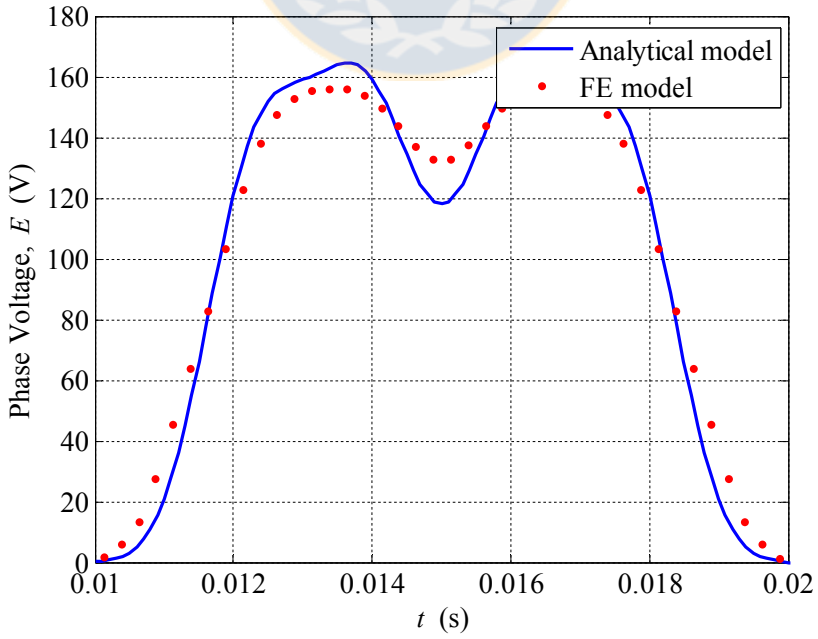

(a)

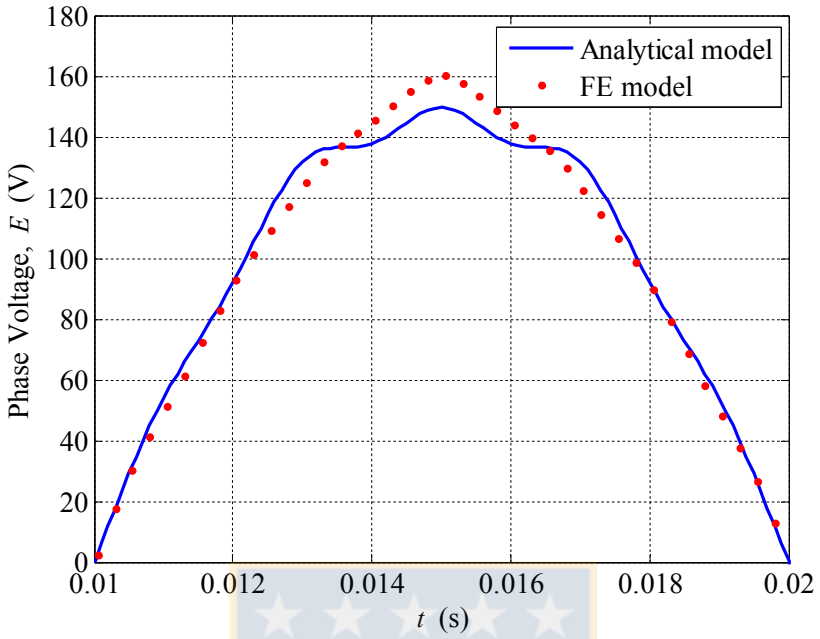

(b)

Fig. 2.10. No-load phase-induced voltage; (a) 30-slot 10-pole machine, (b) 12-slot 10-pole machine with the DL winding. (Source: own elaboration)

For an integer slot distributed winding, the factors $k_{\mathrm{p}v}$, $k_{\mathrm{d}v}$, and $k_{\mathrm{sq}v}$ are defined by generalized expressions (Pyrhönen, Jokinen, and Hrabovcová, 2008). However, for a tooth coil winding, $k_{\mathrm{d}v}$ cannot be defined by generalized expressions for each slot and pole configuration.

Regardless of the winding type, $k_{\mathrm{p}v}$ and $k_{\mathrm{sq}v}$ can be defined as in (Pyrhönen, Jokinen, and Hrabovcová, 2008):

$$k_{\mathrm{p}v} = \sin\left(v\frac{W}{y_{\mathrm{Q}}}\frac{\pi}{2}\right) \tag{2.36}$$

$$k_{\mathrm{sq}v} = \frac{\sin\left(v\frac{s_{\mathrm{sq}}}{\tau_{\mathrm{p}}}\frac{\pi}{2}\right)}{v\frac{s_{\mathrm{sq}}}{\tau_{\mathrm{p}}}\frac{\pi}{2}}, \tag{2.37}$$

where y_{Q} is the pole pitch measured in the number of slots, $s_{\mathrm{sq}}/\tau_{\mathrm{p}}$, is the skewing pitch ratio to the pole pitch, and y is the winding step defined as in (Bianchi et al., 2007):

$$W = round\{Q_{\mathrm{s}}/(2p)\}. \tag{2.38}$$

It can be shown that Eqs. (2.32) and (2.36) are equivalent. Furthermore, for the DW, $Q_s/2p$ is an integer number.

To determine k_{dv}, some authors propose the use of a voltage phasor graph (Magnussen and Sadarangani, 2003; Jussila, 2009), also known as the star of slots theory (Bianchi et al., 2006). The star of slots theory can be used to determine the best winding configuration that maximizes the main winding factor (Bianchi et al., 2007). Another method to determine the winding configuration based on the number of slots per pole and phase q was proposed in (Cros and Viarouge, 2002). In (Yokoi et al., 2016), the authors put their efforts into developing a generalized expression for the winding factor, but this expression does not cover all the slot and pole combinations either.

A particular case for the tooth coil machine with a DL winding is when the number of spokes per phase q_{ph} is an integer number. In such cases, it is possible to define a generalized expression for k_{dv}. These kinds of slot and pole configurations also produce symmetrical phase coils (Cros and Viarouge, 2002), (Magnussen and Sadarangani, 2003), (Bianchi et al., 2007).

The star of slots is formed by Q_s/t spokes, each spoke containing t phasors. According to (Bianchi et al., 2007)

$$q_{ph} = \frac{Q_s}{mt}, \tag{2.39}$$

for the 12-slot 10-pole machine with the DL winding $t = 1$ and $q_{ph} = 4$ as shown in Fig. 2.5(a).

The analytic expressions for the distributed factor can be divided into two different cases depending on whether q_{ph} is an even or odd number.

a) Distribution factor with an even q_{ph}

When q_{ph} is even, the distribution factor for the DL TCW is written as in (Bianchi et al., 2007):

$$k_{dv} = \frac{\sin\left(q_{ph}\frac{\alpha_{phv}}{4}\right)}{\frac{q_{ph}}{2}\sin\left(\frac{\alpha_{phv}}{2}\right)} \tag{2.40}$$

with

$$\alpha_{phv} = \alpha_{ph}\left(1 + \delta_{ph}\frac{v-p}{t}\right), \tag{2.41}$$

where α_{ph} is defined as the angle between two spokes

$$\alpha_{\mathrm{ph}} = \frac{2\pi}{(Q_{\mathrm{s}}/t)} \tag{2.42}$$

and

$$\delta_{\mathrm{ph}} = \frac{kQ_{\mathrm{s}}/t + 1}{p/t}. \tag{2.43}$$

The constant k is the smallest natural number that makes δ_{ph} an integer number (Bianchi et al., 2007).

b) Distribution factor with an odd q_{ph}

When q_{ph} is an odd number, the distribution factor is given by (Bianchi et al., 2007)

$$k_{\mathrm{d}v} = \frac{\sin\left(q_{\mathrm{ph}}\frac{\alpha_{\mathrm{ph}v}}{4}\right)}{q_{\mathrm{ph}}\sin\left(\frac{\alpha_{\mathrm{ph}v}}{4}\right)}. \tag{2.44}$$

3 Inductance

3.1 Introduction

The winding inductance is an important parameter in rotational electrical machines. The electromagnetic torque, the fault current, the ripple torque, and the field weakening capability are related to the inductance (El-Refaie et al., 2008). This parameter depends on the geometrical dimensions, the winding arrangement, and the material properties of the machine (Pyrhönen, Jokinen, and Hrabovcová, 2008). Considering a PMSM machine, the synchronous inductance L_s can be divided into two components; the magnetizing inductance (L_m) that represents the flux linkage produced by the slot current, which is involved in the electromagnetic torque production, and the leakage inductance (L_σ), which does not participate in the torque production of the machine

$$L_s = L_m + L_\sigma. \tag{3.1}$$

The leakage inductance can be divided into different components as

$$L_\sigma = L_h + L_u + L_{tt} + L_{ew}, \tag{3.2}$$

where L_h is the air-gap harmonic leakage inductance, L_u is the slot leakage inductance, L_{tt} is the tooth tip leakage inductance, and L_{ew} is the end-winding leakage inductance. The air-gap harmonic leakage inductance is the only leakage inductance component that crosses the air gap from the stator winding to the rotor and depends mainly on the winding configuration (Ponomarev, 2013). The other leakage inductance components do not cross the air gap and depend on the geometrical parameters, stator material, and winding configuration.

3.2 Magnetizing inductance

The magnetizing inductance of a TCW-PMSM can be derived considering a slotless machine as shown in Fig. 2.1(a). In such a machine, the linear current density of a balanced three-phase winding can be written as in (Bianchi et al., 2007)

$$A_{3\Phi} = \sum_{v=1}^{\infty} \hat{A}_v \cos\left(\frac{2v}{D}x - \omega_r t\right), \tag{3.3}$$

where $\hat{A}_v$ is the amplitude of linear current density for the AFPMM defined by

$$\hat{A}_v = \frac{2mk_{wv}N\hat{I}}{\pi D}. \tag{3.4}$$

The flux density produced by the main harmonic ($v = p$) can be calculated from Ampere's law as

$$\oint H\mathrm{d}l = \int_{-\frac{\pi D}{4p}}^{\frac{\pi D}{4p}} \hat{A}_p \cos\left(\frac{2p}{D}x\right)\mathrm{d}x. \tag{3.5}$$

Assuming an infinitely permeable iron, Eq. (3.5) results in

$$\hat{B}_p = \frac{\mu_0 \hat{A}_p}{\delta_{PM}} \frac{D}{2p}. \tag{3.6}$$

For a single-turn coil, the maximum value of the main harmonic component of the flux is

$$\hat{\Phi}_m = l_{ef} \int_{-\frac{\pi D}{2Q_s}}^{\frac{\pi D}{2Q_s}} \hat{B}_p \cos\left(\frac{2p}{D}x\right)\mathrm{d}x, \tag{3.7}$$

where l_{ef} is the effective stator core length defined in (Pyrhönen et al., 2010). Developing Eq. (3.7) results in

$$\hat{\Phi}_m = \frac{Dl_{ef}}{p}\hat{B}_p \sin\left(p\frac{\pi}{Q_s}\right) = \frac{Dl_{ef}}{p}\hat{B}_p k_{pp}, \tag{3.8}$$

where k_{pp} is the pitch factor for the main harmonic order. The flux linkage of the phase winding with N conductors connected in series is

$$\hat{\psi}_m = \frac{Dl_{ef}}{p}\hat{B}_p k_{pp} k_{dp} N = \frac{Dl_{ef}}{p}\hat{B}_p k_{wp} N. \tag{3.9}$$

By substituting Eq. (3.6) into Eq. (3.9) and considering that $L = \psi/I$, the magnetizing inductance for a TCW-PMSM is written as

$$L_{\mathrm{m}} = \mu_0 \frac{D l_{\mathrm{ef}}}{\pi p^2} \frac{m}{\delta_{\mathrm{PM}}} \left(k_{\mathrm{w}p} N\right)^2 = \mu_0 \frac{2m\tau_{\mathrm{p}}}{\pi^2 p} \frac{l_{\mathrm{ef}}}{\delta_{\mathrm{PM}}} \left(k_{\mathrm{w}p} N\right)^2. \tag{3.10}$$

if the slotting effect and the magnetic voltage drop in the iron is to be taken into account then δ_{ef} has be used instead of δ_{PM}. The expression given by Eq. (3.10) is similar to the expression of the magnetizing inductance for the DW. The difference lies in the main winding factor for each winding configuration.

3.3 Air-gap harmonic leakage inductance

Owing to the discrete distribution of the stator slots, the currents on conductors produce various harmonic contents in the air-gap flux density distribution. These harmonics are linked by the winding, thereby increasing the leakage inductance of the machine. In the DW-PMSM, the air-gap harmonic leakage inductance component is generally neglected because of its small value with respect to the other inductance sources. However, in the TCW-PMSM characterized by a strong harmonic content of current linkage, the air-gap harmonic leakage inductance must be considered. The total air-gap inductance (L_δ) defined by

$$L_\delta = L_{\mathrm{m}} + L_{\mathrm{h}} \tag{3.11}$$

can be determined by following the same procedure used for the magnetizing inductance considering all the harmonic orders of Eq. (3.3). The total air-gap inductance is written as

$$L_\delta = \mu_0 \frac{2m\tau_{\mathrm{p}}}{\pi^2 p} \frac{l_{\mathrm{ef}}}{\delta_{\mathrm{ef}}} \sum_{v=1}^{\infty} \left(\frac{p}{v} k_{\mathrm{w}p} N\right)^2. \tag{3.12}$$

By substituting Eq. (3.10) and Eq. (3.12) into Eq. (3.11), the air-gap harmonic leakage inductance is

$$L_{\mathrm{h}} = \mu_0 \frac{2m\tau_{\mathrm{p}}}{\pi^2 p} \frac{l_{\mathrm{ef}}}{\delta_{\mathrm{ef}}} \sum_{\substack{v=1 \\ v \neq p \\ v \neq 3k}}^{\infty} \left(\frac{p}{v} k_{\mathrm{w}v} N\right)^2, \tag{3.13}$$

where $k = 1, 2, \ldots \mathbb{N}$. The third-order harmonics were omitted from Eq. (3.13) because of the three-phase winding connection of the stator (Ponomarev, 2013). Expressing Eq. (3.13) in terms of magnetizing inductance gives

$$L_{\mathrm{h}} = \sigma_{\delta} L_{\mathrm{m}}, \tag{3.14}$$

where σ_{δ} is defined as the leakage factor of the air-gap harmonic inductance (Pyrhönen, Jokinen, and Hrabovcová, 2008) given by

$$\sigma_{\delta} = \sum_{\substack{v=1 \\ v \neq p \\ v \neq 3k}}^{\infty} \left(\frac{p}{v} \frac{k_{\mathrm{w}v} N}{k_{\mathrm{w}p}} \right)^2. \tag{3.15}$$

3.4 Slot leakage inductance

To determine the slot leakage inductance, it is assumed that the iron of the teeth is infinitely permeable and the current is evenly distributed into the slot area. Thus, the flux path goes from one slot side to the other side following a straight line. Depending on the winding configuration, that is, the SLW, DLW, or multilayer winding, the slot leakage inductance can be changed because of the self- and mutual inductance components between the coil sides of the different phases in the slots. It is pointed out that even though this doctoral dissertation considers the DLW, the procedure could be used also for multilayer windings. For the SLW, the solution is trivial.

The slot leakage inductance expression is estimated considering the simplified geometry of the slot shown in Fig. 3.1(a) where h_{hs} is the head slot height and z_{c} is the number of conductors per coil side. Depending on the arrangement of the coils into the slots, it is possible to have the coil side configuration as shown in Fig. 3.1(b) or Fig. 3.1(c). The first configuration, vertical coils, is generally adopted in DW-PMSMs, whereas the second one, horizontal coils, is most commonly used in the TCW-PMSMs.

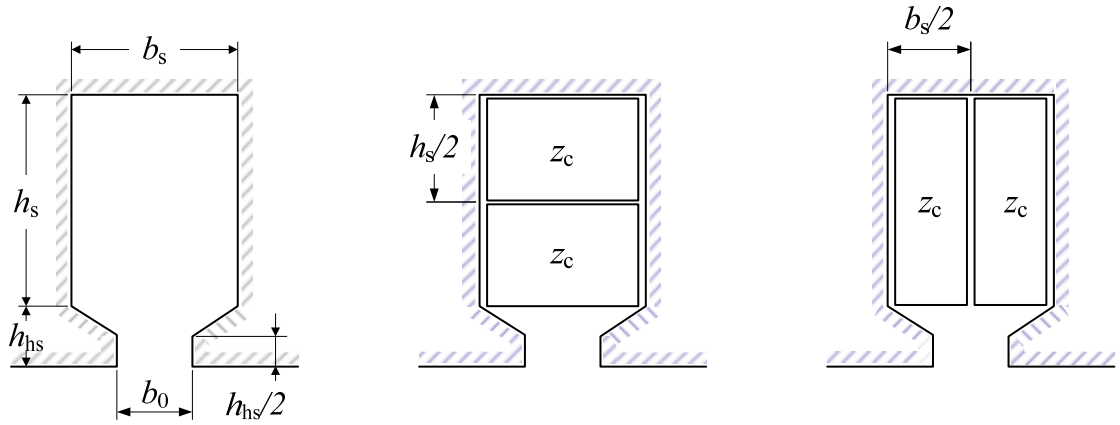

(a) (b) (c)

Fig. 3.1. (a) Slot geometry dimensions, (b) double-layer winding (vertical coils), and (c) double-layer winding (horizontal coils). (Source: own elaboration)

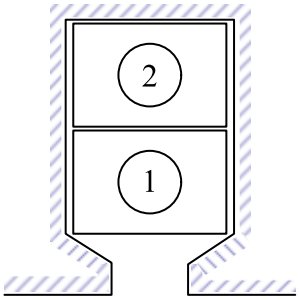

Fig. 3.2. Coil side distribution of two different phases in a slot considering a vertical coil arrangement. (Source: own elaboration)

3.4.1 Vertical coils

If the coils arranged into the slot shown in Fig. 3.1(b) belong to the same phase, there is only a self-inductance component given by (see Appendix A)

$$L = \mu_0 l_{\text{ef}} \lambda (2z_{\text{c}})^2, \tag{3.16}$$

where λ is

$$\lambda = \frac{h_{\text{s}}}{3b_{\text{s}}} + \frac{h_{\text{hs}}}{2(b_{\text{s}} - b_0)} \ln \frac{b_{\text{s}}}{b_0} + \frac{h_{\text{hs}}}{2b_0}. \tag{3.17}$$

In the case when the coil sides in the slot belong to different phases as shown in Fig. 3.2, there are self- and mutual inductance components given by

$$L_1 = \mu_0 l_{\text{ef}} \lambda_1 z_{\text{c}}^2 \tag{3.18}$$

$$L_2 = \mu_0 l_{\text{ef}} \lambda_2 z_{\text{c}}^2 \tag{3.19}$$

$$M = M_{21} = M_{12} = \mu_0 l_{\text{ef}} \lambda_{\text{M}} z_{\text{c}}^2, \tag{3.20}$$

where λ_1, λ_2, and λ_{M} are derived in Appendix A and can be written as

$$\lambda_1 = \frac{h_{\text{s}}}{6b_{\text{s}}} + \frac{h_{\text{hs}}}{2(b_{\text{s}} - b_0)} \ln \frac{b_{\text{s}}}{b_0} + \frac{h_{\text{hs}}}{2b_0} \tag{3.21}$$

$$\lambda_2 = \frac{2h_{\text{s}}}{3b_{\text{s}}} + \frac{h_{\text{hs}}}{2(b_{\text{s}} - b_0)} \ln \frac{b_{\text{s}}}{b_0} + \frac{h_{\text{hs}}}{2b_0} \tag{3.22}$$

$$\lambda_{\text{M}} = \frac{h_{\text{s}}}{4b_{\text{s}}} + \frac{h_{\text{hs}}}{2(b_{\text{s}} - b_0)} \ln \frac{b_{\text{s}}}{b_0} + \frac{h_{\text{hs}}}{2b_0}. \tag{3.23}$$

The slot leakage inductance for the phase winding considering the coils arranged into the slots as shown in Fig. 3.2 is given by Eq. (3.24), and is derived in Appendix A:

$$L_{\mathrm{uv}} = \frac{4m}{Q_{\mathrm{s}}}\mu_0 l_{\mathrm{ef}} N^2 \lambda_{\mathrm{uv}}\,, \tag{3.24}$$

where λ_{uv} is the permeance factor of the slot leakage flux for a double-layer winding

$$\lambda_{\mathrm{uv}} = k_{1\mathrm{v}}\frac{h_{\mathrm{s}}}{3b_{\mathrm{s}}} + k_2\left[\frac{h_{\mathrm{hs}}}{2(b_{\mathrm{s}}-b_0)}\ln\frac{b_{\mathrm{s}}}{b_0} + \frac{h_{\mathrm{hs}}}{2b_0}\right], \tag{3.25}$$

with

$$k_{1\mathrm{v}} = \frac{5+3g}{8} \tag{3.26}$$

and

$$k_2 = \frac{1+g}{2}, \tag{3.27}$$

where g is defined as

$$g = \frac{m}{Q_{\mathrm{s}}}\sum_{n=1}^{Q_{\mathrm{s}}/m}\cos 2\gamma \tag{3.28}$$

and γ is the phase shift between the currents of the coil sides in the slot. For a single-layer winding $g = 1$.

3.4.2 Horizontal coils

If the coil sides arranged into the slot belong to the same phase, the self-inductance expression is equal to Eq. (3.16). However, if the coil sides in the slot belong to different phases as shown in Fig. 3.3, λ_1, λ_2, and λ_{M} are given by

$$\lambda_1 = \lambda_2 = \lambda_{\mathrm{M}} = \frac{h_{\mathrm{s}}}{3b_{\mathrm{s}}} + \frac{h_{\mathrm{hs}}}{2(b_{\mathrm{s}}-b_0)}\ln\frac{b_{\mathrm{s}}}{b_0} + \frac{h_{\mathrm{hs}}}{2b_0}\,. \tag{3.29}$$

The slot leakage inductance for the phase winding considering the coils arranged into the slots as shown in Fig. 3.3 is given by Eq. (3.30), and is derived in Appendix A

$$L_{\mathrm{uh}} = \frac{4m}{Q_{\mathrm{s}}}\mu_0 l_{\mathrm{ef}} N^2 \lambda_{\mathrm{uh}}\,, \tag{3.30}$$

where λ_{uh} is given by

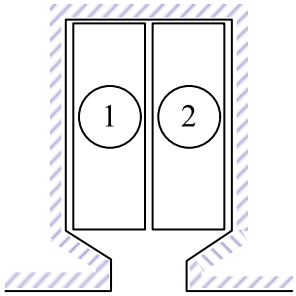

Fig. 3.3. Coil side distribution of two different phases in a slot considering a horizontal coil arrangement. (Source: own elaboration)

$$\lambda_{\mathrm{uv}} = k_{1\mathrm{h}} \frac{h_{\mathrm{s}}}{3b_{\mathrm{s}}} + k_2 \left[\frac{h_{\mathrm{hs}}}{2(b_{\mathrm{s}} - b_0)} \ln \frac{b_{\mathrm{s}}}{b_0} + \frac{h_{\mathrm{hs}}}{2b_0} \right], \tag{3.31}$$

and

$$k_{1\mathrm{h}} = k_2 \tag{3.32}$$

3.4.3 Slot leakage inductance from q = 0.25 to q = 0.5

The slot leakage inductance can be written in terms of the number of slots per pole and phase (q), the pole pitch expressed in the number of slots (y_{Q}), and the coil pitch expressed in the number of slots (W) for a given combination of slots and poles from q = 0.25 to q = 0.5.

Defining t' as the G.C.D(Q_{s},2p), the winding arrangement will have $q' - |y_{\mathrm{q}}' - W'|$ slots with coil sides of the same phase, and $2|y_{\mathrm{q}}' - W'|$ slots with coil sides of different phases per each $2p/t'$ pole of the machine. The variables q', y_{Q}', and W' are given by

$$q' = q\left(\frac{2p}{t'}\right) \tag{3.33}$$

$$y_{\mathrm{Q}}' = y_{\mathrm{Q}}\left(\frac{2p}{t'}\right) \tag{3.34}$$

$$W' = W\left(\frac{2p}{t'}\right), \tag{3.35}$$

For the DW, t' is always equal to 2p, whereas for the TCW, t' can take different values depending on the slot and pole combination. Furthermore, for the TCW, the coil pitch is equal to 1.

For the vertical coil arrangement, the slot leakage inductance is written as

$$L_{\mathrm{uv}} = \mu_0 l_{\mathrm{ef}} \frac{h_{\mathrm{s}} z_{\mathrm{c}}^2}{b_{\mathrm{s}}} t' \left(\frac{4}{3} q' - \frac{1}{4} \left| {y_{\mathrm{q}}}' - W' \right| \right) + \mu_0 l_{\mathrm{ef}} \lambda_{\mathrm{hs}} z_{\mathrm{c}}^2 t' \left(4q' - \left| {y_{\mathrm{q}}}' - W' \right| \right), \tag{3.36}$$

where λ_{hs} is defined as the slot head leakage permeance factor

$$\lambda_{\mathrm{hs}} = \frac{h_{\mathrm{hs}}}{b_{\mathrm{s}} - b_0} \ln \frac{b_{\mathrm{s}}}{b_0} + \frac{h_{\mathrm{hs}}}{2b_0}. \tag{3.37}$$

Considering Eq. (3.33) to Eq. (3.35), it is possible to write Eq. (3.36) as

$$L_{\mathrm{uv}} = \mu_0 \frac{h_{\mathrm{s}} l_{\mathrm{ef}} z_{\mathrm{c}}^2}{b_{\mathrm{s}}} 2p \left(\frac{4}{3} q - \frac{1}{4} \left| y_{\mathrm{Q}} - W \right| \right) + \mu_0 l_{\mathrm{ef}} \lambda_{\mathrm{hs}} z_{\mathrm{c}}^2 2p \left(4q - \left| y_{\mathrm{Q}} - W \right| \right), \tag{3.38}$$

and taking into account that the number of conductors per coil side is related to the number of turns per phase by

$$z_{\mathrm{c}} = \frac{N}{2pq}. \tag{3.39}$$

The slot leakage inductance for the phase winding can be written as

$$L_{\mathrm{uv}} = \frac{4\mu_0 h_{\mathrm{s}} l_{\mathrm{ef}} N^2}{3b_{\mathrm{s}}} \frac{m}{Q_{\mathrm{s}}} \left(1 - \frac{3}{16} \frac{\left| y_{\mathrm{Q}} - W \right|}{q} \right) + 4\mu_0 l_{\mathrm{ef}} \lambda_{\mathrm{hs}} N^2 \frac{m}{Q_{\mathrm{s}}} \left(1 - \frac{\left| y_{\mathrm{Q}} - W \right|}{4q} \right). \tag{3.40}$$

The expression given by Eq. (3.40) is equivalent to the expression presented in (Wallace et al., 2012) for the DW, and therefore, it can be used to estimate the slot leakage inductance for the DL-TCW and the DL-DW.

For the horizontal coil arrangement, the corresponding slot leakage inductance for the phase winding is given by

$$L_{\mathrm{uh}} = \frac{4\mu_0 l_{\mathrm{ef}} h_{\mathrm{s}} N^2}{3b_{\mathrm{s}}} \frac{m}{Q_{\mathrm{s}}} \left(1 - \frac{\left| y_{\mathrm{Q}} - W \right|}{4q} \right) + 4\mu_0 l_{\mathrm{ef}} \lambda_{\mathrm{hs}} N^2 \frac{m}{Q_{\mathrm{s}}} \left(1 - \frac{\left| y_{\mathrm{Q}} - W \right|}{4q} \right). \tag{3.41}$$

3.4.4 Discussion

To compare the slot leakage inductance of horizontal coils with that of vertical coils for the TCW, we can assume a rectangular slot geometry ($\lambda_{\mathrm{hs}} = 0$). Dividing Eq. (3.41) by Eq. (3.40) results in

$$k_{\mathrm{u}} = \frac{1 - \frac{|y_{\mathrm{Q}} - W|}{4q}}{1 - \frac{3}{16}\frac{|y_{\mathrm{Q}} - W|}{q}}, \tag{3.42}$$

Table 3.1. Slot leakage flux factors from q = 0.25 to q = 0.5. (Source: own elaboration)

Q_s \ $2p$		4	6	8	10	12	14	16	18	20
6	q	1/2		1/4						
	y_Q	3/2		3/4						
	k_u	**0.923**		**0.923**						
9	q		1/2	3/8	3/10	1/4				
	y_Q		3/2	9/8	9/10	3/4				
	k_u		**0.923**	**0.978**	**0.978**	**0.923**				
12	q			1/2	2/5		2/7	1/4		
	y_Q			3/2	6/5		6/7	3/4		
	k_u			**0.923**	**0.966**		**0.966**	**0.923**		
15	q				1/2		5/14	5/16		1/4
	y_Q				3/2		15/14	15/16		3/4
	k_u				**0.923**		**0.987**	**0.987**		**0.923**
18	q					1/2	3/7	3/8		3/10
	y_Q					3/2	9/7	9/8		9/10
	k_u					**0.923**	**0.952**	**0.978**		**0.978**
21	q						1/2	7/16		7/20
	y_Q						3/2	21/16		21/20
	k_u						**0.923**	**0.948**		**0.991**
24	q							1/2		2/5
	y_Q							3/2		6/5
	k_u							**0.923**		**0.966**
27	q								1/2	9/20
	y_Q								3/2	27/20
	k_u								**0.923**	**0.943**

Unbalanced magnetic pull.

The number of poles is a multiple of phase number; unsymmetrical phase coil.

High value of the main winding factor (k_{wp} > 0.9).

where k_u is defined as the slot leakage flux factor. Considering that for the tooth coil winding $W = 1$, the slot leakage flux factor is written as

$$k_u = \frac{16q - 4|y_Q - 1|}{16q - 3|y_Q - 1|}. \tag{3.43}$$

The values of the slot leakage flux factor for different slot and pole combinations are shown in Table 3.1. The minimum value of k_u is 0.923 with $q = 0.25$ or $q = 0.5$. This means that the slot leakage inductance of vertical coils is 8 % lower compared with the horizontal coil distribution. The difference between the inductance expressions for slot and pole combinations with a high value of the main winding factor varies approximately between a minimum value close to zero and a maximum value of 8 %.

For $q < 0.25$ and $q > 0.5$, the factor k_u can be obtained by dividing Eq. (3.30) by Eq. (3.24). Assuming a rectangular slot geometry, the slot leakage flux factor is

$$k_u = \frac{4 + 4g}{5 + 3g}. \tag{3.44}$$

Equation (3.44) is also valid from $q = 0.25$ to $q = 0.5$.

3.5 Tooth tip leakage inductance

The tooth tip leakage inductance, also known as zig-zag leakage inductance, is produced by the flux travelling between adjacent slots through the air gap. This leakage inductance can be calculated considering the tooth tip leakage permeance factor. Different expressions for the tooth tip permeance factor can be found in the literature (Wallace et al., 2012; Richter and Brüderlink, 1964; Voldek, 1974). Considering the Richter expression

$$\lambda_{tt} = k_2 \left(\frac{5\delta'_{PM}}{5b_0 + 4\delta'_{PM}} \right), \tag{3.45}$$

the tooth tip leakage inductance is given by

$$L_{tt} = \frac{4m}{Q} \mu_0 l_{ef} \lambda_{tt} N^2 \tag{3.46}$$

The tooth tip leakage inductance for $q = 0.25$ to $q = 0.5$ can be written as

$$L_{tt} = \frac{4m}{Q} \mu_0 l_{ef} \lambda_{tt} N^2 \left[1 - \frac{(\tau - W)}{4q} \right]. \tag{3.47}$$

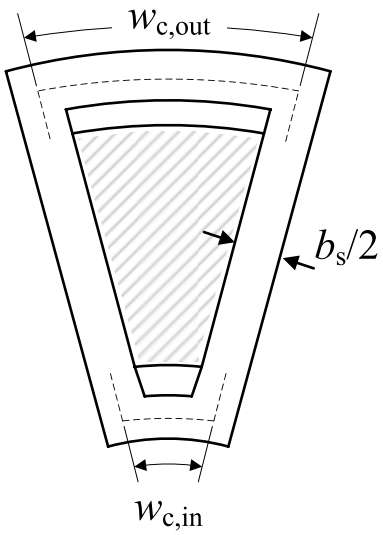

Fig. 3.4. End-winding geometry for a DL-TCW. (Source: own elaboration)

3.6 End-winding leakage inductance

The end-winding leakage inductance produced by the end-winding connection can have a significant effect on the total leakage inductance in the AFPM machines. As a result of the relatively short length of the stack, which is limited by the diameter ratio, the length of the end winding can be large compared with the total length of the coil as shown in Fig. 3.4. Considering the trapezoidal geometry of the coils in the AF machines, the end-winding connections at the outer and inner diameters have different sizes, and therefore, the analytical expression for RF machines cannot be applied without making some adjustments.

According to (Gieras et al., 2008), the end-winding leakage inductance for AF machines can be estimated by the following expression

$$L_{\mathrm{ew}} = 4\mu_0 N^2 \frac{m}{Q_{\mathrm{s}}}\left(l_{\mathrm{ew,in}}\lambda_{\mathrm{w,in}} + l_{\mathrm{ew,out}}\lambda_{\mathrm{w,out}}\right), \tag{3.48}$$

where $l_{\mathrm{ew,in}}$ is the length of the inner end winding, $l_{\mathrm{ew,out}}$ is the length of the outer end winding, and $\lambda_{\mathrm{w,in}}$, $\lambda_{\mathrm{w,out}}$ are the permeance factors of the inner and outer end windings, respectively, given by

$$\lambda_{\mathrm{w,in}} = 0.17q\left(1 - \frac{2}{\pi}\frac{w_{\mathrm{c,in}}}{l_{\mathrm{ew,in}}}\right) \tag{3.49}$$

$$\lambda_{\mathrm{w,out}} = 0.17q\left(1 - \frac{2}{\pi}\frac{w_{\mathrm{c,out}}}{l_{\mathrm{ew,out}}}\right), \tag{3.50}$$

where $w_{\mathrm{c,in}}$ is the inner coil span and $w_{\mathrm{c,out}}$ is the outer coil span.

4 Power losses

Owing to the structural characteristics of electrical machines, power losses play a critical role in the machine operation. Electrical machines are typically manufactured as semi-enclosed or totally enclosed configurations to protect the winding, bearings, and other parts of the machine from ambient factors, such as moisture, abrasion, and mechanical damage. These factors affect the power dissipation capacity of the machine, and therefore, a complex cooling system must be used. To avoid the problem of power dissipation, thermal modelling of electrical machines is necessary, and therefore, detailed knowledge of loss distributions is required (Wrobel et al., 2016).

4.1 Winding losses

From the design point of view, winding losses can be estimated by

$$P_{\mathrm{Cu}} = 3R_{\mathrm{AC}}I^2, \tag{4.1}$$

where R_{AC} is the electrical resistance of the phase winding for a given working temperature, and I is the phase current in RMS. The resistance expression for a low-speed machine is given by

$$R_{\mathrm{AC}} = k_{\mathrm{R}}\frac{\rho_{\mathrm{Cu}}l_{\mathrm{c}}}{S_{\mathrm{c}}}, \tag{4.2}$$

where ρ_{Cu} is the resistivity of the conductor at a given temperature, S_{c} is the cross-sectional area of the conductor, k_{R} is the skin effect factor (Pyrhönen, Jokinen, and Hrabovcová, 2008) and l_{c} is the total length of the conductor, given by

$$l_{\mathrm{c}} \approx N\left[2l_{\mathrm{e}} + l_{\mathrm{ew,in}} + l_{\mathrm{ew,out}}\right]. \tag{4.3}$$

4.2 Core power losses

Core losses produced in the rotor and stator cores are computed by the 2D FEA using a commercial package (Flux by Cedrat). According to the model used by the software (based on Bertotti's method), the iron losses per unit volume can be divided into hysteresis losses, P_{h}', classical eddy current losses P_{c}', and excess losses P_{e}'

$$P_{\mathrm{Fe}}' = P_{\mathrm{h}}' + P_{\mathrm{c}}' + P_{\mathrm{e}}'. \tag{4.4}$$

Writing Eq. (4.4) in terms of average power over an electrical period T results in

Table 4.1. Iron loss coefficients obtained from the manufacturer data. (Source: own elaboration)

Frequency (Hz)	k_h $\left(\frac{W \cdot s}{m^3 T^2}\right)$	k_e $\left(\frac{W \cdot s}{m^3 T^2}\right)$
50	125.85	0.765
100	165.48	0.361
200	185.47	0.311

$$P'_{Fe} = k_{Fe}\left\{k_h B^2 f + \frac{1}{T}\int_0^T \left[\sigma_{Fe}\frac{d^2}{12}\left(\frac{dB(t)}{dt}\right)^2 + k_e\left(\frac{dB(t)}{dt}\right)^{1.5}\right]dt\right\}, \quad (4.5)$$

where k_{Fe} is the lamination stack factor, k_h is the hysteresis loss coefficient, and k_e is the loss in the excess coefficient. The coefficients k_h and k_e can be determined from the measurement loss curve of the magnetic steel manufacturer data. Figure 4.1 compares the measurement-specific iron losses of laminated steel M400-50A provided by the manufacturer with the analytical prediction considering the estimated coefficient k_h and k_e for three different frequencies of Table 4.1. This frequency range is selected around the nominal frequency (125 Hz) to ensure a good estimation of iron losses in the machine using Bertotti's method (Juergens et al., 2015).

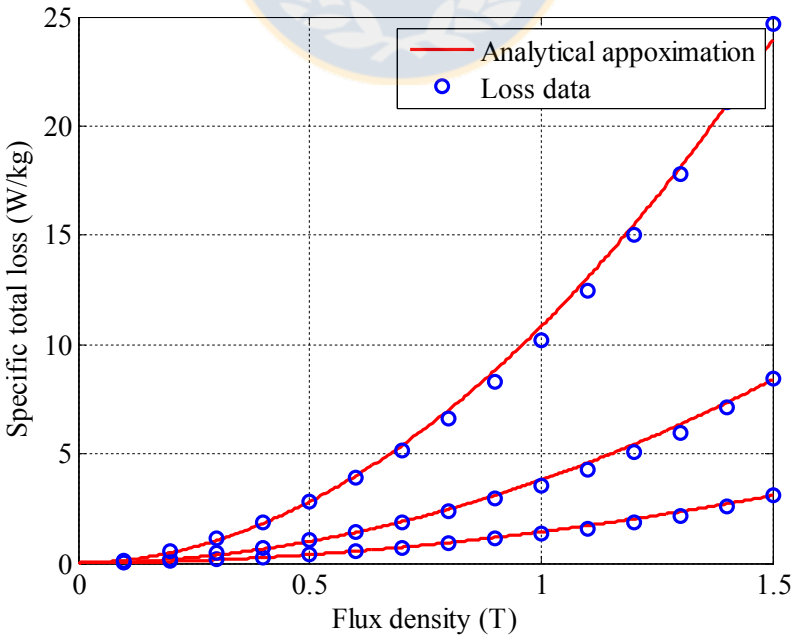

Fig. 4.1. Specific iron loss of laminated steel M400-50A. (Source: own elaboration)

The average power dissipated in a volume region V is obtained from

$$P_{\mathrm{Fe}} = \iiint_V P'_{\mathrm{Fe}} \mathrm{d}V. \tag{4.6}$$

4.3 Rotational losses

Rotational losses, also defined as mechanical losses, can be divided into windage losses $P_{\rho\mathrm{w}}$, ventilation losses P_{vent}, and bearing losses $P_{\rho\mathrm{b}}$

$$P_{\rho} = P_{\rho\mathrm{w}} + P_{\mathrm{vent}} + P_{\rho\mathrm{b}}. \tag{4.7}$$

According to (Gieras et al., 2008), the windage losses for a disk-type rotating machine can be estimated by

$$P_{\rho\mathrm{w}} = \frac{1}{64} C_{\mathrm{M}} \rho \omega_{\mathrm{r}}^3 \left(D_{\mathrm{se}}^5 - D_{\mathrm{sh}}^5\right), \tag{4.8}$$

where D_{sh} is the shaft diameter, ρ is the specific density of the coolant medium, and C_{M} is the torque coefficient, which depend on the tip Reynolds number (Pyrhönen, Jokinen, and Hrabovcová, 2008)

$$C_{\mathrm{M}} = \frac{3.87}{Re_{\mathrm{r}}^{0.5}}, \qquad Re_{\mathrm{r}} < 3 \times 10^5 \tag{4.9}$$

$$C_{\mathrm{M}} = \frac{3.87}{Re_{\mathrm{r}}^{0.2}}, \qquad Re_{\mathrm{r}} > 3 \times 10^5. \tag{4.10}$$

The tip Reynolds number for a rotating disc is given by

$$Re_{\mathrm{r}} = \frac{\rho \omega_{\mathrm{r}} D_{\mathrm{o}}^2}{4\mu}, \tag{4.11}$$

where μ is the dynamic viscosity of the coolant. Considering an air-cooled AFPM machine, $\rho_{\mathrm{air,20°C}} = 1.2$ kg/m^3 and $\mu_{\mathrm{air,20°C}} = 1.8 \times 10^{-5}$ Pa · s.

The bearing losses for small machines can be estimated using the expression given in (Gieras et al., 2008):

$$P_{\rho\mathrm{b}} = \frac{3 k_{\mathrm{b}} m_{\mathrm{r}} \omega_{\mathrm{r}}}{100\pi}, \tag{4.12}$$

where $k_{\mathrm{b}} = 1$ to 3 and m_{r} is the mass of the rotating part.

The bearing losses calculated by Eq. (4.12) take into account the radial load over the bearing produced by the weight of the rotor structure, the permanent magnets, the lamination steel layer, and the shaft. On the other hand, in an axial flux machine, the axial load over the bearing produced by the magnetic attraction of permanent magnets and the stator steel should be considered. The axial force can be compensated for in a two-stator one-rotor topology and reduced to zero by aligning the rotor with the symmetry plane of the machine. However, a perfect alignment is difficult to reach, and a net axial force over the bearing is present. For example, Fig. 4.2(b) shows the axial force for a two-stator one-

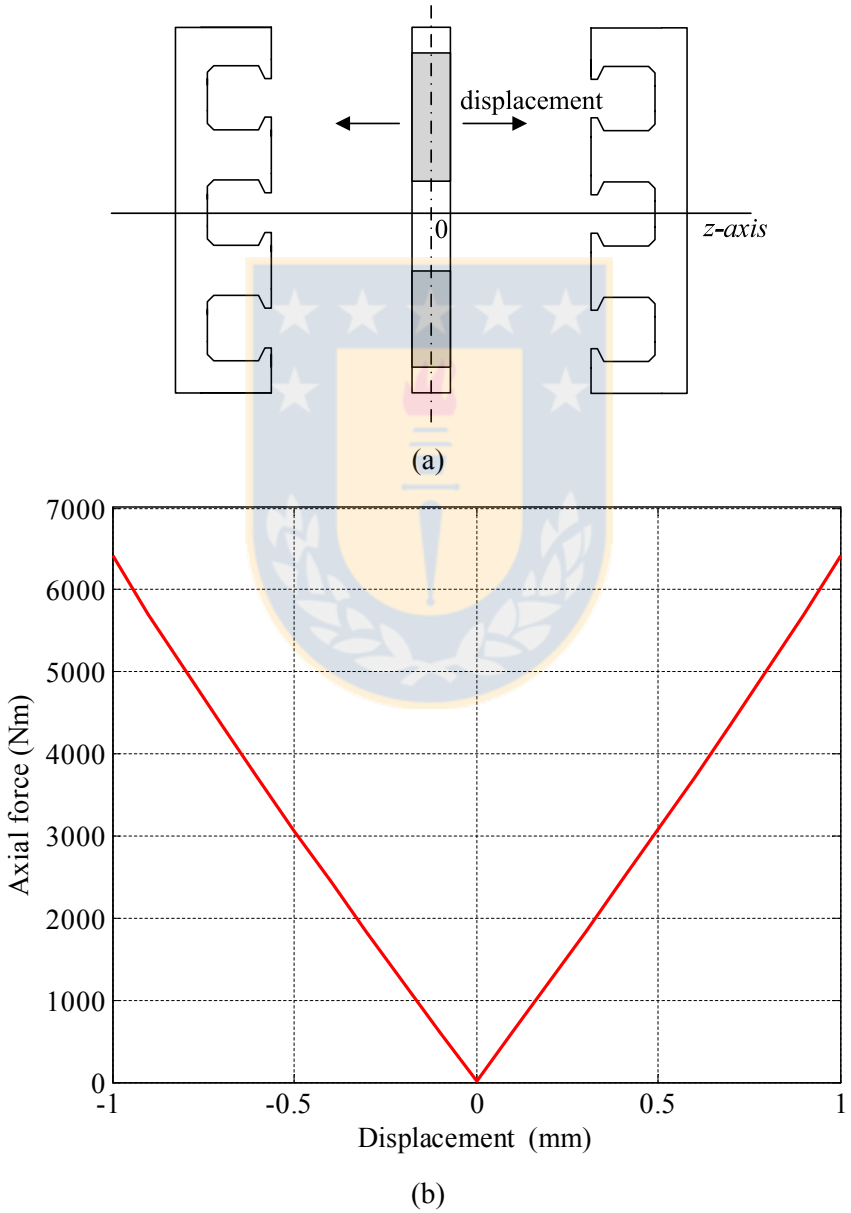

Fig. 4.2. Axial force in an AFPM machine; (a) schematic illustration, (b) axial net force over the rotor as a function of the position of the rotor with respect to the symmetry plane. (Source: own elaboration)

rotor AFPM machine of Fig. 4.2(a) considering the data of Table 4.2. A small displacement of 0.1 mm in the axial direction (z-axis) produces a net axial force of 610 Nm equivalent to 61 kg_F, and a displacement of 1 mm produces a net axial force of 6400 Nm equivalent to 650 kg_F.

The ventilation losses depend on the cooling fan system. In our case, the prototype is designed without a cooling fan, and therefore, $P_{\text{vent}} = 0$.

4.4 Permanent magnet losses

The losses in the PMs of synchronous machines are produced by the flux density variation over the entire volume of the magnet. In rotational electrical machines it is possible to identify three different main sources of flux density variation: the permanence harmonics produced by the irregular surface of the stator because of the slot opening, the current linkage harmonics produced by the discrete distribution of the current in the stator slots, and the time harmonics related to the inverter used to supply the machine. Because of the relatively high conductivity of sintered rare-earth PM materials, the dominant mechanism of loss production is the eddy current effect. Hysteresis losses also occur in PMs as shown in (Fukama et al., 2005), but according to (Pyrhönen et al., 2015), the hysteresis losses in sintered NdFeB PM can be negligible in correctly designed machines.

In the past, the study of eddy current losses in the PMs was often neglected because of the use of a distributed winding configuration in the stator, which produces almost a sinusoidal current linkage distribution rotating in synchronism with the rotor (Toda et al.,

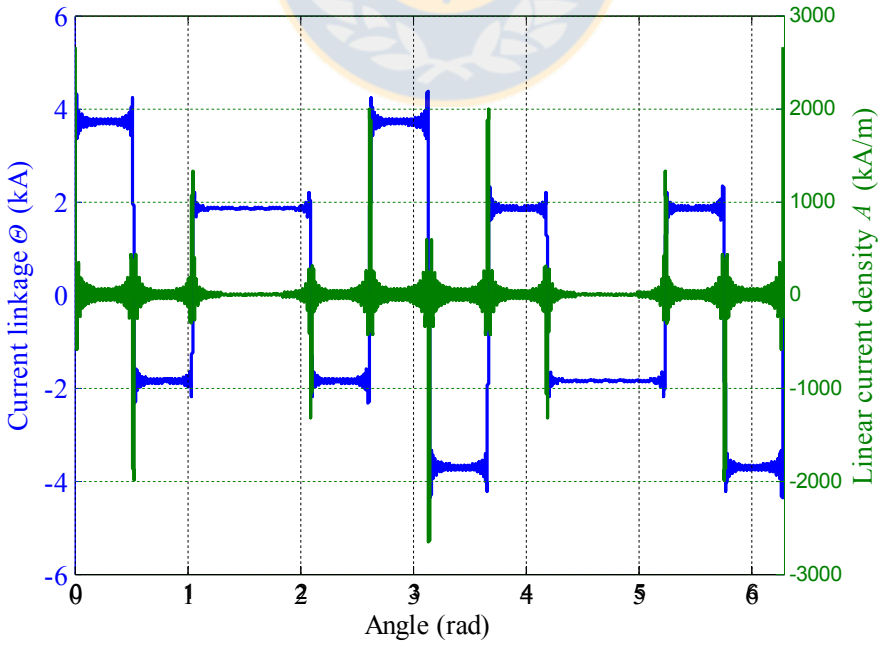

Fig. 4.3. Linear current density and current linkage for a 12-slot 10-pole machine with a double-layer winding at rated current. (Source: own elaboration)

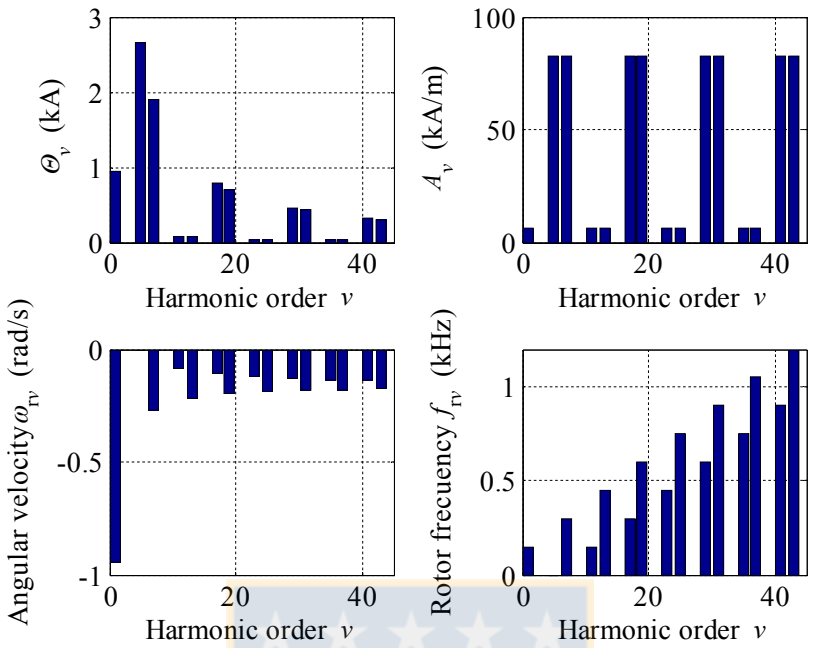

Fig. 4.4. Harmonic analysis of a 12-slot 10-pole machine with a double-layer winding, rotating at 1500 rpm at rated current. (Source: own elaboration)

2004). However, because of the increasing adoption of TCW, the eddy current losses have received growing interest over the last 20 years. The TCW machines produce strong current linkage harmonic components rotating at different speeds with respect to the rotor.

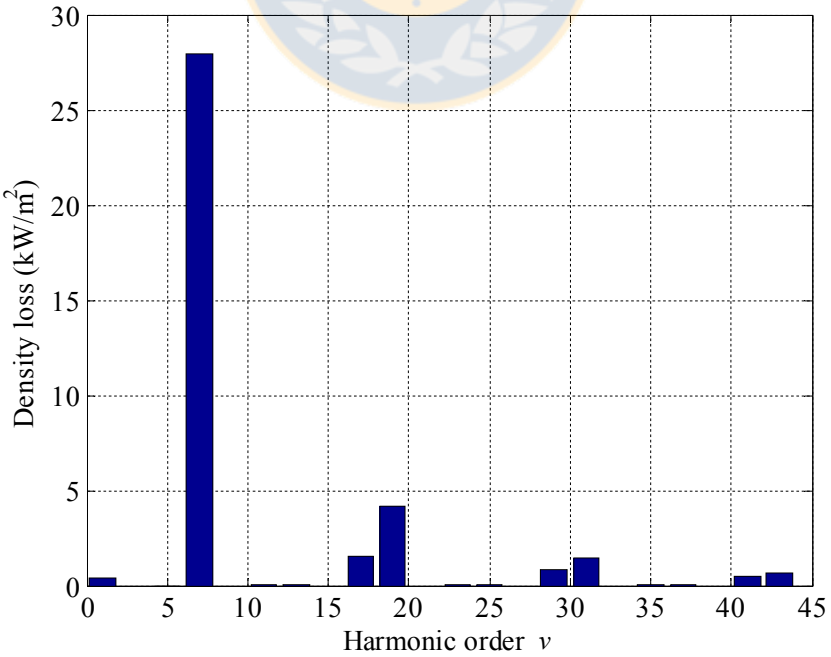

Fig. 4.5. Harmonic analysis of loss density in the permanent magnet, the machine rotating at 1500 rpm at rated current. (Source: own elaboration)

Several analytical and numerical techniques can be found that focus on the eddy current losses in PMs. The analytical approaches differ in terms of assumptions made to simplify the mathematical solution of problems, at the cost of the model accuracy. Using the principle of superposition, the sources of eddy losses are studied separately. Some analytical approaches focus on the effects of permeance harmonics (Markovic and Perriard, 2008; Alberti et al., 2008, Wills and Kamper, 2010; Alexandrova et al., 2010; Fang et al., 2012; Sharkh et al., 2011; Wu et al., 2012; Pyrhönen et al., 2014), whereas other approaches concentrate on the effect of the armature reaction (Atallah et al., 2000; Ishak et al., 2005; Bianchi et al., 2007, Bianchi et al., 2010; Wang et al., 2010; Huang et al. 2010; Mirzaei et al., 2012; Pyrhönen et al., 2014). Nevertheless, in this doctoral dissertation, the analysis of eddy current losses was made mainly by the FE computation. This is due to the fact that the geometry applied to reduce the losses in the PMs (Jara et al., 2016) has saturated areas and a complex shape, which complicates an analytical analysis. Alternatively, the analytical models described in (Alberti et al., 2008) and (Bianchi et al., 2007) were used in the first stage during the dimensioning of the machine to estimate the losses caused by the slotting effect and the current linkage, respectively. The analytical model is based on a linear representation of the machine along a cylindrical cutting plane at the mean diameter, at which Maxwell's equations are solved (Alberti et al., 2008).

For instance, we can consider the data of Table 4.2 to draw the linear current density given by Eq. (3.3) of a double-layer 12-slot 10-pole machine as shown in Fig. 4.3.

The current linkage is obtained by (Ponomarev et al., 2013)

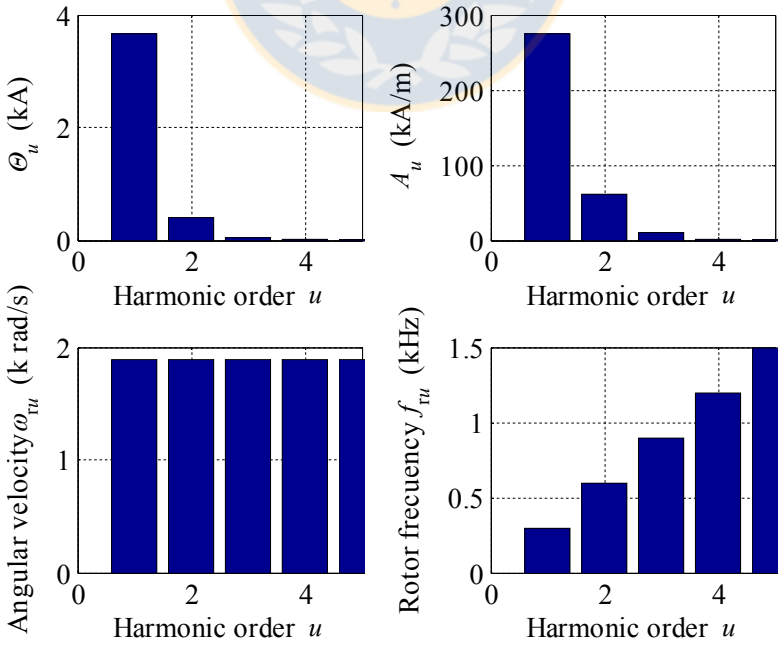

Fig. 4.6. Harmonic analysis of the slotting effect of a 12-slot 10-pole machine with a double-layer winding, the machine rotating at 1500 rpm at no load. (Source: own elaboration)

$$\Theta(\theta) = \int A(\theta)\, d\theta. \tag{4.13}$$

The harmonic components of current linkage and linear current density are presented in Fig. 4.4. The angular velocity of a given harmonic in the rotor reference frame is given by

$$\omega_{rv} = 2\pi f \left(\frac{\mathrm{sgn}_v}{v} - \frac{1}{p}\right), \tag{4.14}$$

where sgn_v is the sign function defined in (Bianchi and Fornasiero, 2009). The corresponding frequency induced in the rotor is

$$f_{rv} = f\left|\mathrm{sgn}_v - v/p\right|. \tag{4.15}$$

The angular velocity and the induced frequency for each current linkage harmonic of the 12-slot 10-pole machine considering a rotational velocity of 1500 rpm are shown in Fig. 4.4.

The eddy current loss density computed analytically for each harmonic considering a sintered NdFeB magnet with a resistivity of 180×10^{-8} Ω·m and a relative permeability of 1.03 is shown in Fig. 4.5. The harmonic component of the current linkage that produces the higher loss density corresponds to $v = 7$. Considering the total area of the PMs, the mean value of the eddy losses is 3.9 kW.

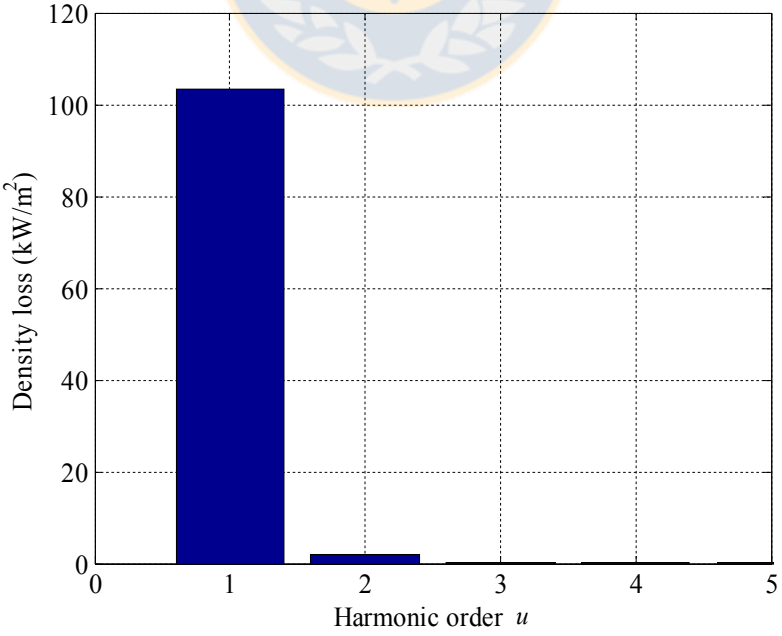

Fig. 4.7. Harmonic analysis of the loss density produced by the slotting effect in the permanent magnet, the machine rotating at 1500 rpm. (Source: own elaboration)

To estimate the losses produced by the permeance harmonics, we can determine an equivalent linear current density that produces the same flux density drop in front of the slots (Alberti et al., 2008).

$$\Delta B_u = \frac{B_{\mathrm{r,PM}}}{1 + \dfrac{\mu_{\mathrm{r,PM}}\delta}{h_{\mathrm{PM}}}} \tilde{\lambda}_u \,, \tag{4.16}$$

with the relative permeance function given by Eq. (2.24) computed at the bored stator.

The peak value of the linear current density for the uth harmonic is

$$A_u = \frac{\pi \Delta B_u}{\tau_{\mathrm{s}} \mu_0} \left(\delta + \frac{h_{\mathrm{PM}}}{\mu_{\mathrm{r,PM}}} \right), \tag{4.17}$$

The angular rotor velocity is given by

$$\omega_{\mathrm{r}u} = 2\pi f Q_{\mathrm{s}}/p \,, \tag{4.18}$$

and the corresponding frequency induced in the rotor is

$$f_{\mathrm{r}u} = fuQ_{\mathrm{s}}/p \,. \tag{4.19}$$

In Fig. 4.6, Θ_u A_u, $\omega_{\mathrm{r}u}$ and $f_{\mathrm{r}u}$ considering the slot width of Table 4.2 are shown. The harmonic component of the loss density is depicted in Fig. 4.7. For the slotting effect, the

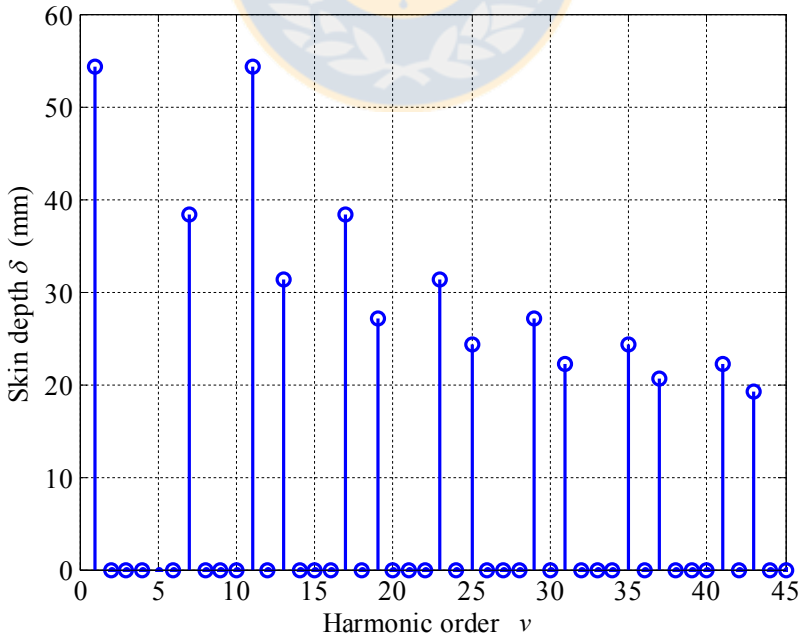

Fig. 4.8. Skin depth calculation for an NdFeB magnet for different harmonic orders. (Source: own elaboration)

higher loss density corresponds to u = 1. The mean value of eddy current losses on the PMs is 10.4 kW. The total losses in the PMs are approx. 14.3 kW.

For the FE model, the mesh density in the PM region can be obtained from the skin depth calculation (Sharkh et al., 2011)

$$\delta_{\mathrm{PM}} = \sqrt{\frac{\rho_{\mathrm{PM}}}{\pi f_{rv} \mu_{\mathrm{r,PM}} \mu_0}}, \tag{4.20}$$

where ρ_{pm} is the resistivity of the permanent magnet, $\mu_{\mathrm{r,PM}}$ is the relative permeability of the permanent magnet, and f_{rv} is the frequency of the highest most significant space or time harmonic. However, in low-speed applications, the frequencies induced in the rotor have relatively low values, and the mesh elements are much smaller than the skin depth.

The skin depth for each harmonic can be estimated introducing the induced frequency values into Eq. (4.20). Figure 4.8 shows the skin depth for the sintered NdFeB magnet used in the machine. We may assume that for the high-order harmonics, the skin depth is still greater compared with the dimensions of the applied permanent magnet. However, when modelling high-speed machines, this consideration should be taken into account to have a correct estimation of PM losses.

4.5 Reduction of permanent magnet eddy current losses

Because of the heat dissipation and permanent magnet demagnetization problems, bulky magnets cannot be used in the TCW machines without the implementation of loss reduction techniques such as the use of soft magnetic wedges (Donato et al., 2012). However, the losses in the soft magnetic wedges can increase the total losses in the machine (Donato et al., 2013). Permanent magnet segmentation provides an effective

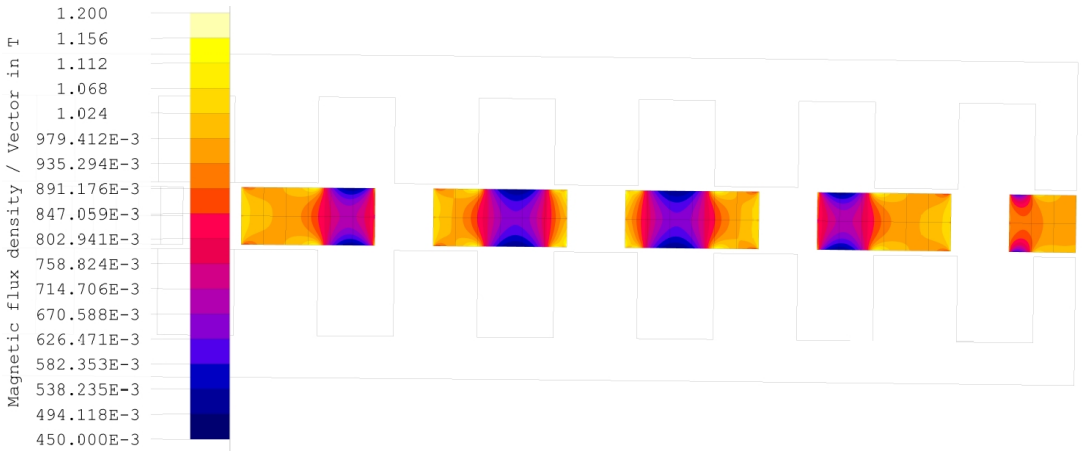

(a)

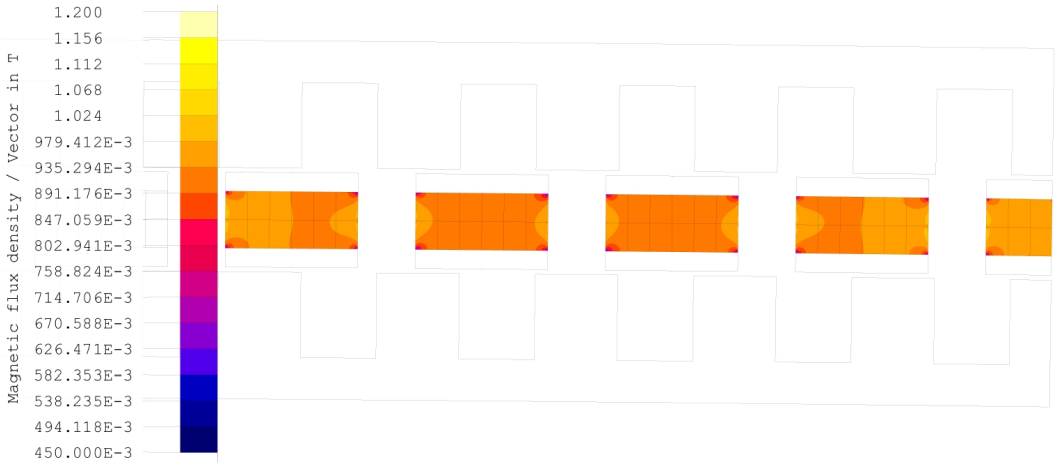

(b)

Fig. 4.9. No-load flux density variation in the permanent magnets for different rotor positions; (a) no steel lamination, (b) 10 mm of steel lamination. (Source: own elaboration)

method to reduce the eddy current losses in low-speed machines (Wu et al., 2012). Considering the RF topology, the axial and circumferential segmentation and a combination of both can be used (Atallah et al., 2000; Huang et al. 2010; Yamazaki and Fukushima, 2011; Wu et al., 2012; Mirzaei et al., 2012). Permanent magnet segmentation can also be used in AF machines (Jussila et al., 2008; Jussila, 2009; Jussila et al., 2010;

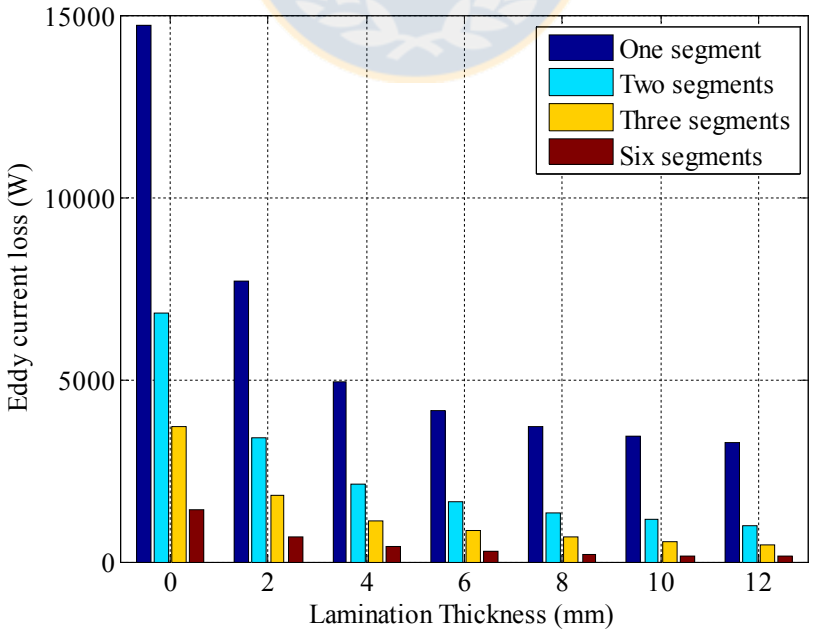

Fig. 4.10. Eddy current losses in permanent magnets as a function of rotor surface lamination thickness. (Jara et al., 2016)

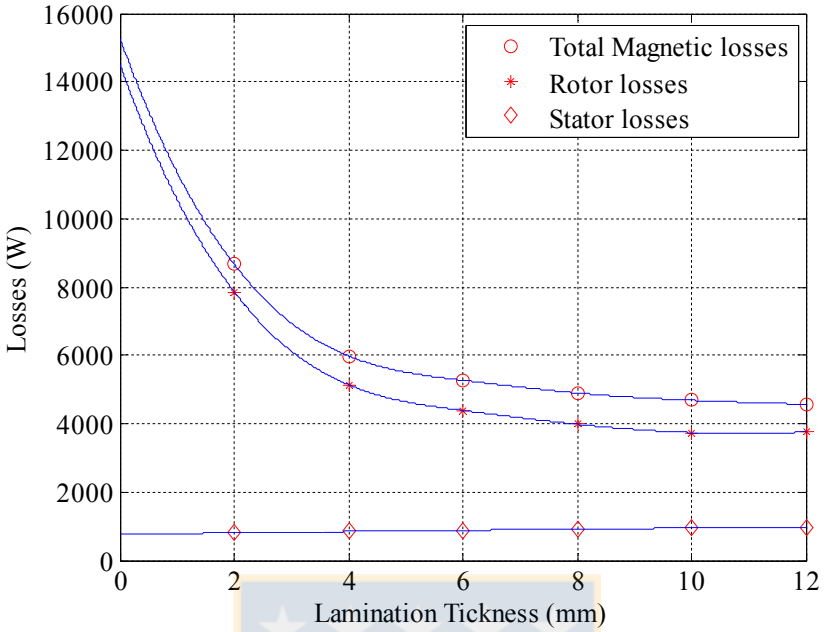

Fig. 4.11. Total electromagnetic losses as a function of lamination thickness. (Jara et al., 2016)

Lindh et al., 2015; Jara et al., 2016). On the other hand, a high number of magnet segments per magnet piece increases the manufacturing cost (Yamazaki and Fukushima, 2011), and therefore, the magnet segmentation should be combined with the optimization of the stator and rotor structures.

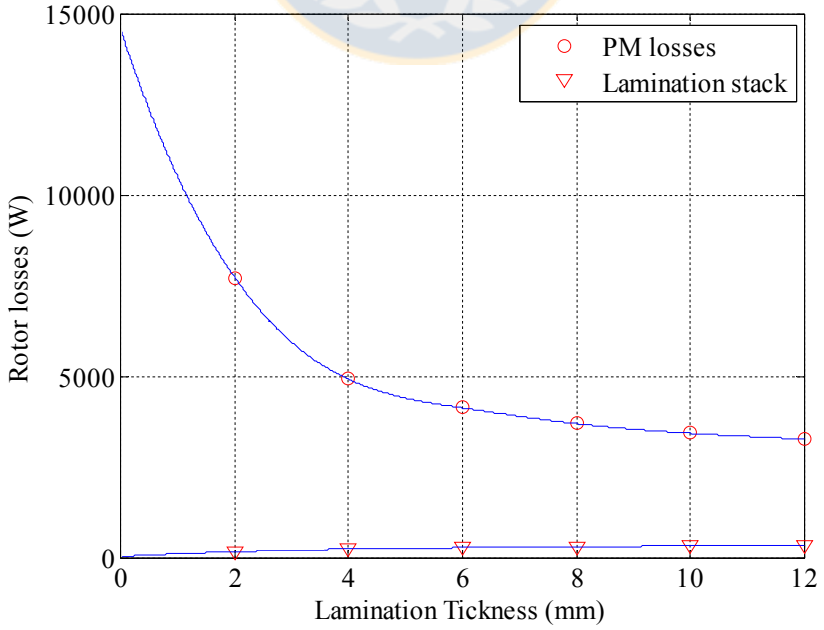

Fig. 4.12. Rotor loss distribution as a function of laminate thickness. (Jara et al., 2016)

The use of an open slot structure to achieve a high copper space factor and to reduce the manufacturing cost of the winding may produce excessive heat generation as was shown in the previous section, which can degrade the magnet properties. Adding a steel lamination layer (radially laminated) to the rotor structure of the AFPM machines with the TCW enables operation with low rotor losses even when an open-slot structure is used (Lindh et al., 2015; Jara et al., 2016). In effect, lamination helps to reduce the air-gap reluctance variations, which results in less flux density variation of the PM as shown in Fig. 4.9, and therefore, a reduction in the iron and PM losses. Without the lamination, Fig. 4.9(a), the magnets are exposed directly to the air-gap reluctance variation with the corresponding high flux density variation, whereas when the lamination is present as shown in Fig. 4.9(b), the flux path travels across the lamination reducing the flux density variation of the PMs. Combination of both techniques (magnet segmentation and steel lamination) results in a significant reduction in eddy current losses of the PM as shown in Fig. 4.10. It can be seen that the steel lamination can also be used to reduce the required PM segments with respect to a given value of eddy current losses.

On the other hand, the total magnetic losses (iron parts + PM losses) of the machine are at the minimum close to 10 mm of the lamination height as shown in Fig. 4.11. This is due to the reduction in the rotor losses. In effect, it can be seen in Fig. 4.11 and Fig. 4.12 that the reduction in losses in permanent magnets is greater compared with the increase in losses in the stator core and in the steel lamination when the lamination height increases.

The steel lamination layer provides additional benefits in terms of induced voltage and torque production. The maximum value of induced voltage is found close to 10 mm of

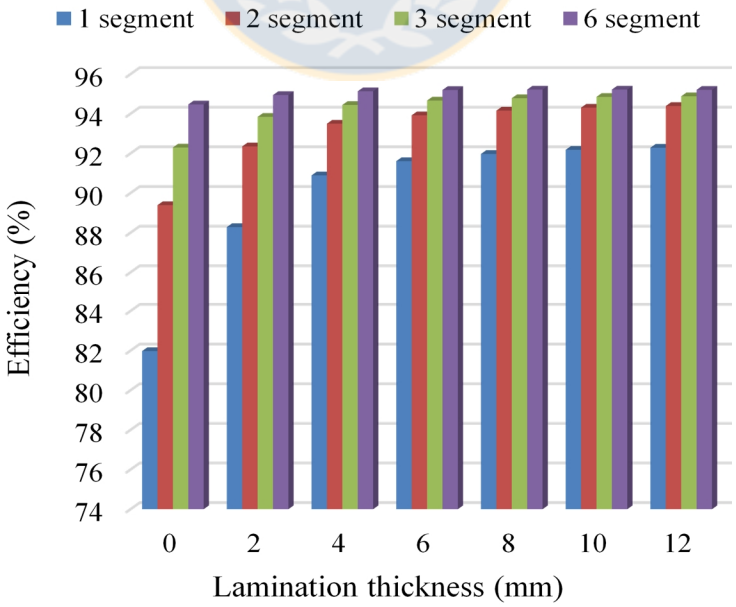

Fig. 4.13. Machine efficiency as a function of rotor surface lamination thickness. (Source: own elaboration)

the lamination height. When the lamination layer reaches the height of 9 to 10 mm, the flux crossing the stator is at the maximum, and later, the leakage flux between the poles becomes more significant, reducing the useful flux. These results are analysed in detail in (Jara et al., 2016).

The effect of the iron lamination on the efficiency of the machine is shown in Fig. 4.13. The Joule losses in the stator winding and the mechanical losses are included. It can be seen that the laminations have a favourable effect on the machine efficiency, and the total electromagnetic losses can be effectively decreased by the addition of iron lamination on the rotor structure. It can be seen that the iron laminations have a higher impact in the case of low numbers of segments per pole-arc.

4.6 Manufacturing effect

Despite the advantages presented of the use of iron lamination, such as the reduction of eddy current losses or the increase in the induced voltage and torque, care must be taken in the manufacturing to avoid extra losses in the rotor laminations. In effect, the welding used for the stacking process of the steel laminations produces a solid electrical connection between each sheet, as illustrated in Fig. 4.14. In the case of this particular machine, because of the open-slotted stator, the flux paths have an axial component (y-axis) and a tangential component (x-axis) as shown in Fig. 4.15. The tangential component alternates at a high frequency as a function of stator tooth position. When the stator tooth is located on the left side of the rotor pole, the flux lines in the lamination stack are directed to the left, as presented in Fig. 4.15 (a), but when the stator tooth is located on the right, as shown in Fig. 4.15 (b), the flux lines are directed to the right. A 2-D FE model was used to estimate the additional losses. The welding was considered a solid conductor with an isotropic resistivity of $10.3 \times 10^{-3}\ \Omega \cdot \mathrm{m}$. Resistivity was experimentally determined in the laboratory test set-up shown in Fig. 4.16. The

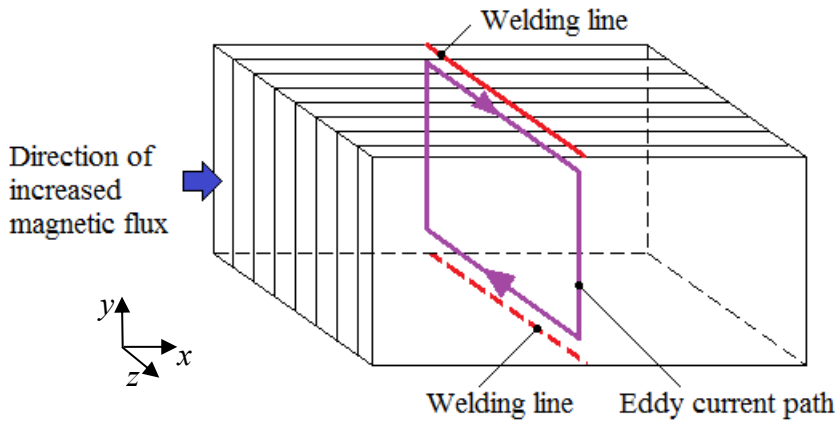

Fig. 4.14. Generation of eddy currents due to alternating flux through the lamination stack. The principal direction of the flux does not travel through the welding loop but as the rotor travels under open slots also the direction marked in the figure becomes effective. (Jara et al., 2016)

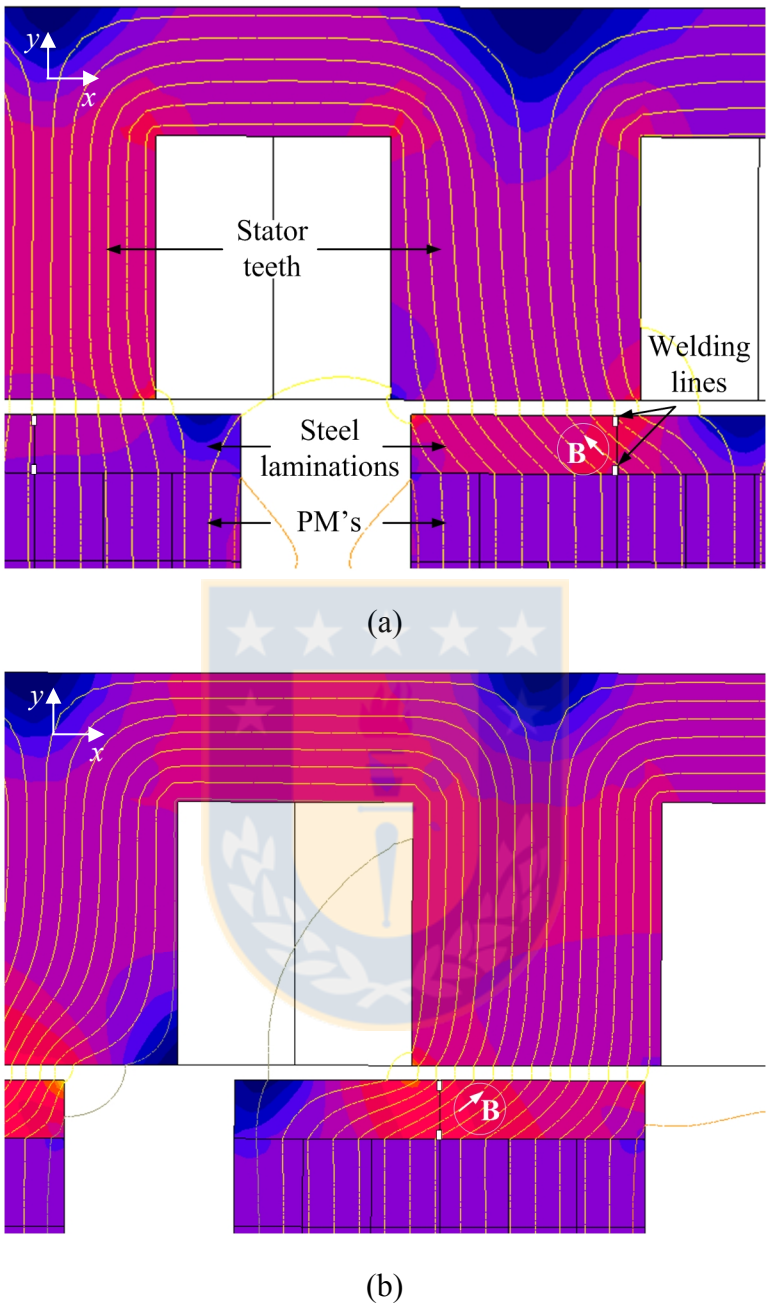

Fig. 4.15. Alternation of the flux path in the lamination stack close to the permanent magnets; a) left position of the tooth, b) right position of the tooth. (Jara et al., 2016)

lamination resistance was neglected because it has a low resistance compared with the welding lines. The mean value of welding losses per pole is 120 W, which results in welding losses of 1200 W in the 10-pole machine. This is, naturally, a very disappointing result, and an improved motor using an alternative joining procedure will be designed.

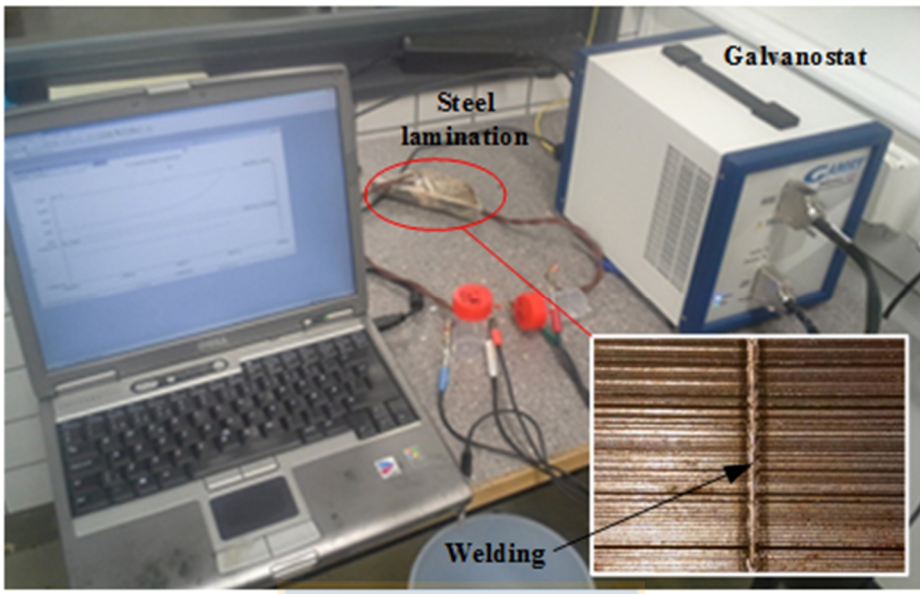

Fig. 4.16. Test set-up to measure the resistance of the lamination welding lines. (Jara et al., 2016)

4.7 Machine prototype and test results

The AFPM machine analysed in this study is a two-stator one-rotor one as shown in Fig. 4.17. The double-side topology yields balanced axial forces (ideally) and reduces the complexity of the bearing compared with a single-side configuration (Parviainen, 2005).

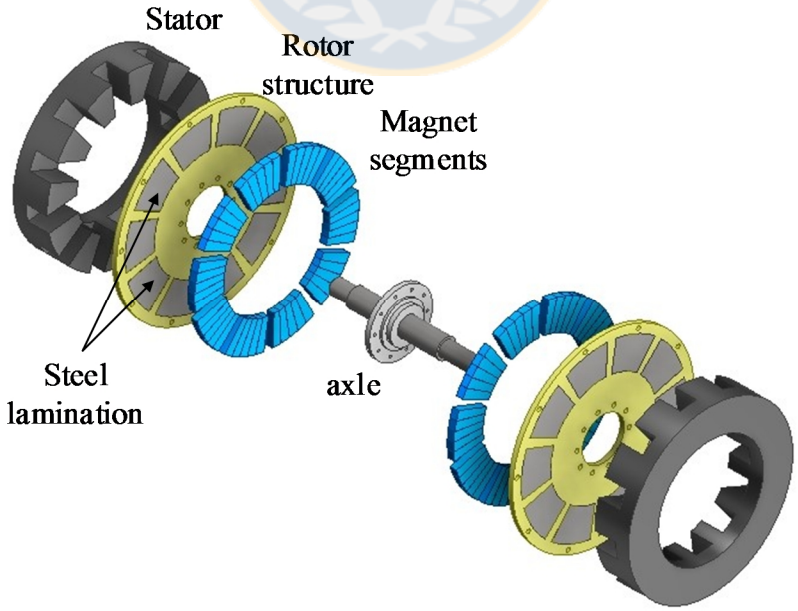

Fig. 4.17. Two-stator one-rotor axial flux machine topology with segmented magnets, the steel lamination layer and the non-ferromagnetic rotor structure. (Source: own elaboration)

Table 4.2. Main dimensions of the machine. (Source: own elaboration)

Symbol	Quantity	Value	Unit
P_{out}	Output power	100	kW
n_{r}	Rotational speed	1500	rpm
U	Line-to-line voltage	380	V
T_{N}	Rated torque	635	Nm
I	Rated current	164	A
D_{o}	Stator outer diameter	390	mm
D_{i}	Stator inner diameter	250	mm
Q	Slot number	12	
p	Pole pair number	5	
δ	Air-gap length	1.5	mm
h_{PM}	Permanent magnet height	30	mm
h_{s}	Slot height	48	mm
b_{s}	Slot width	40	mm
N_{s}	Series turns number per stator	64	
$B_{\mathrm{r,PM}}$	Permanent magnet remanence	1.15	T
$\mu_{\mathrm{r,PM}}$	Relative recoil permeability	1.03	
α_{PM}	Magnet to pole ratio	0.7	

The use of external stators facilitates fixing of the stator to the housing and promotes heat dissipation from the winding losses. The rotor body is made of impregnated fibreglass, which guarantees sufficient mechanical strength and the absence of eddy currents and decreases the leakage flux. The permanent magnets are segmented to reduce the eddy current losses. Two ferromagnetic steel lamination layers per magnet module were added to each face of the PM, and their effect on the machine performance is analysed in detail in (Jara et al., 2016; Jara and Lindh, 2016).

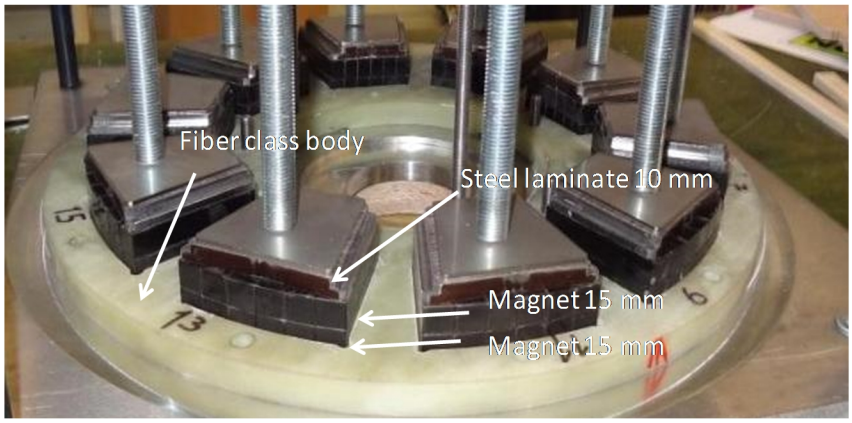

(a)

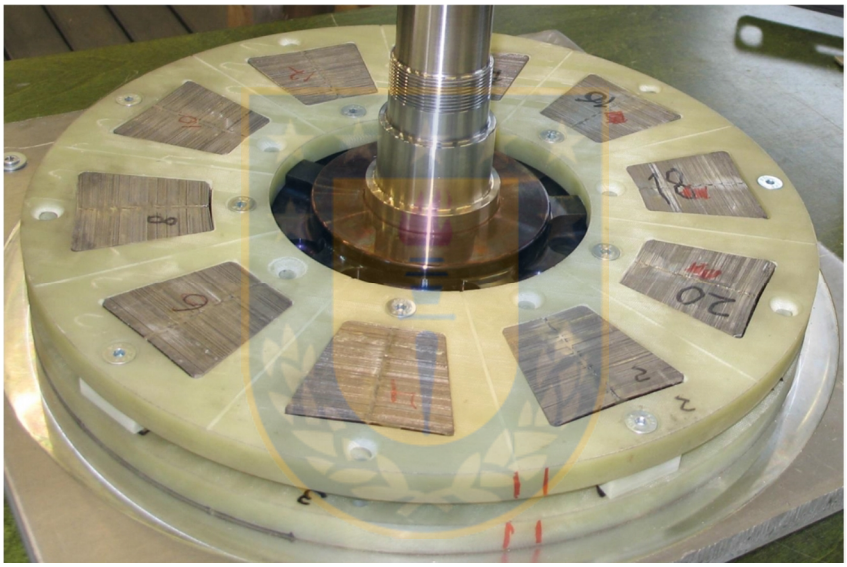

(b)

Fig. 4.18. Rotor structure of the 100 kW axial flux machine. (a) Prototype manufacturing: One permanent magnet module consists of a 10 mm stack of steel lamination, in total 30 mm of permanent magnet (two segmented magnets on top of each other) and another 10 mm stack of steel lamination. (b) Rotor assembly. (Jara et al., 2016)

The required rater power is 100 kW at the rated speed of 1500 rpm. The main parameters and geometrical dimensions are given in Table 4.2.

The high value of tangential stress (σ_{Ftan} = 76.5 kPa) makes it necessary to use a two-stator configuration to avoid a deeper slot with the corresponding increase in the leakage inductance and saturation effect (Jara et al., 2014).

Fig. 4.19. Stator core with a double-layer TCW. (Jara et al., 2016)

A 100 kW prototype machine with 12 slots and 10 poles was constructed as depicted in Fig. 4.18 in order to obtain practical experience of the manufacturing of the tooth coil machine and to verify the computed losses.

The rotor components are shown in Fig. 4.18(a) while the rotor assembly is presented in Fig. 4.18(b). The permanent magnet was made of 12 isolated segments arranged as two-layer modules for each pole. The rotor was made of laminated steel M400-50A.

Each 12-slot stator was made of coiled M400-50A steel band of 70 mm in width. A double-layer TCW was used in the winding arranment with rectangular slots to allow the use of a pre-wound coil. The stator core and the TCW are shown in Fig. 4.19.

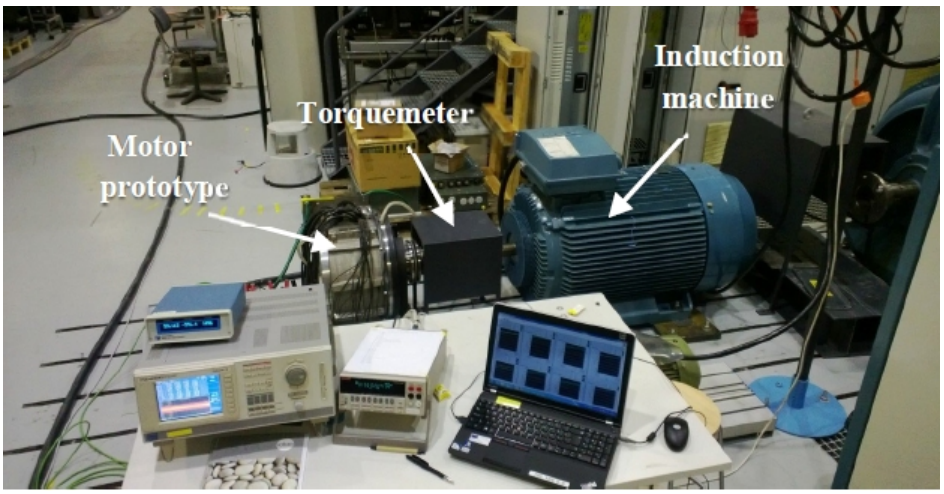

Fig. 4.20. Test set-up to measure the resistance of the lamination welding lines. (Jara et al., 2016)

Table 4.3. Computed and measured values of the 100 kVA prototype. (Source: own elaboration)

	Computed 2D linear model	Measured
Output power, kW	105	100.4
Efficiency, %	95.2	93.9
P copper, W	2260	2100
P stator iron, W	945	
PM loss + steel on top of PM, W	480	
Welding losses	1200	
P no-load (add+mech), W	1600	2200
P total, W	6485	6500
d-axis inductance, p.u.	0.49	0.41
q-axis inductance, p.u.	0.87	0.72
Phase resistance, Ω		0.025

The laboratory set-up and measurement instruments are shown in Fig. 4.20, and the computed and measured values are summarized in Table 4.3.

Figure 4.21 presents the flux density distribution of the machine computed by the 3D FE model. The maximum flux density values of the magnetic circuit are found in the lamination steel layer from 1.7 to 1.9 T. This is due to the flux concentration effect produced by the iron lamination, which produces high-permeability paths for the flux lines from the permanent magnets. The maximum value of the flux density on the stator core is found between 1.3 T and 1.5 T; this value is relatively low and the stator core height will be reduced to improve the power density of the machine. The maximum value of the flux density on the stator teeth is between 1.2 T and 1.4 T. This value is low considering that the saturation point of the stator sheet is close to 1.8 T. However, the stator teeth dimensions were selected based on a second design that includes a hybrid cooling system in order to improve the power dissipation capability of the machine. In this cooling system, cooper bars are inserted into the stator teeth to provide a high thermal

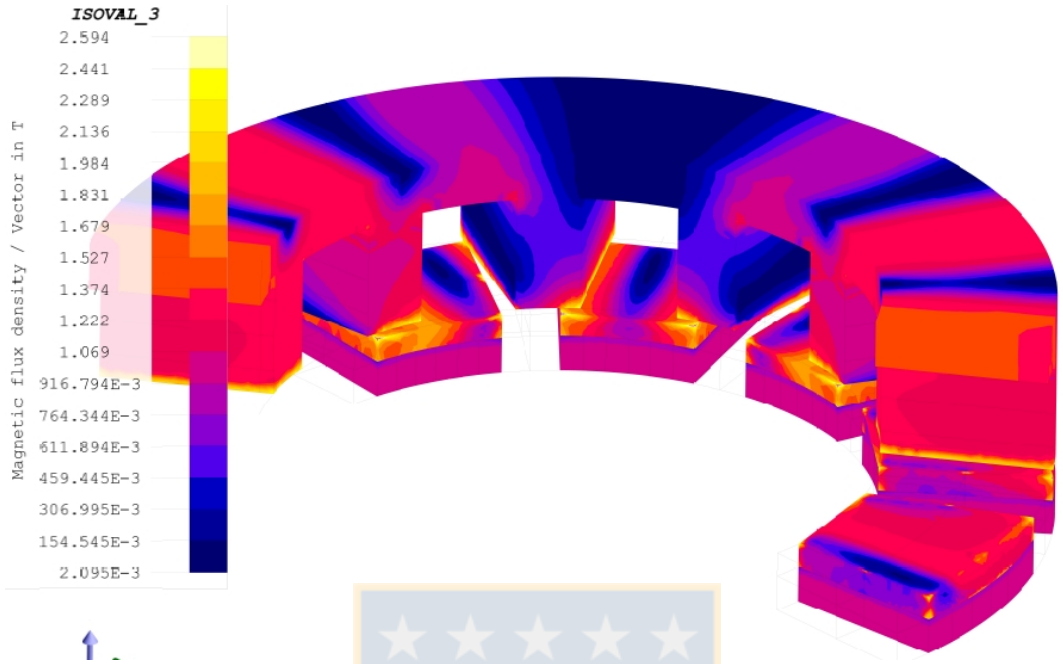

Fig. 4.21. Flux density distribution in the 3D FE model of the machine prototype.

conductivity path for the heat produced in the stator winding (Polikarpova et al., 2015).

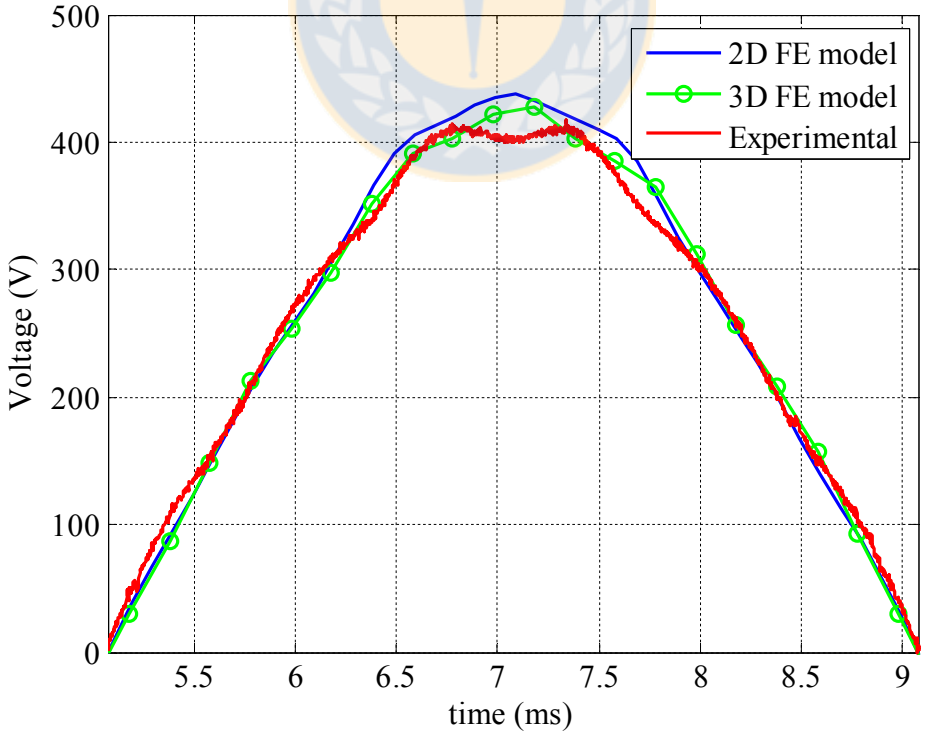

Fig. 4.22. Phase voltage comparison of the machine rotating at nominal speed. (Source: own elaboration)

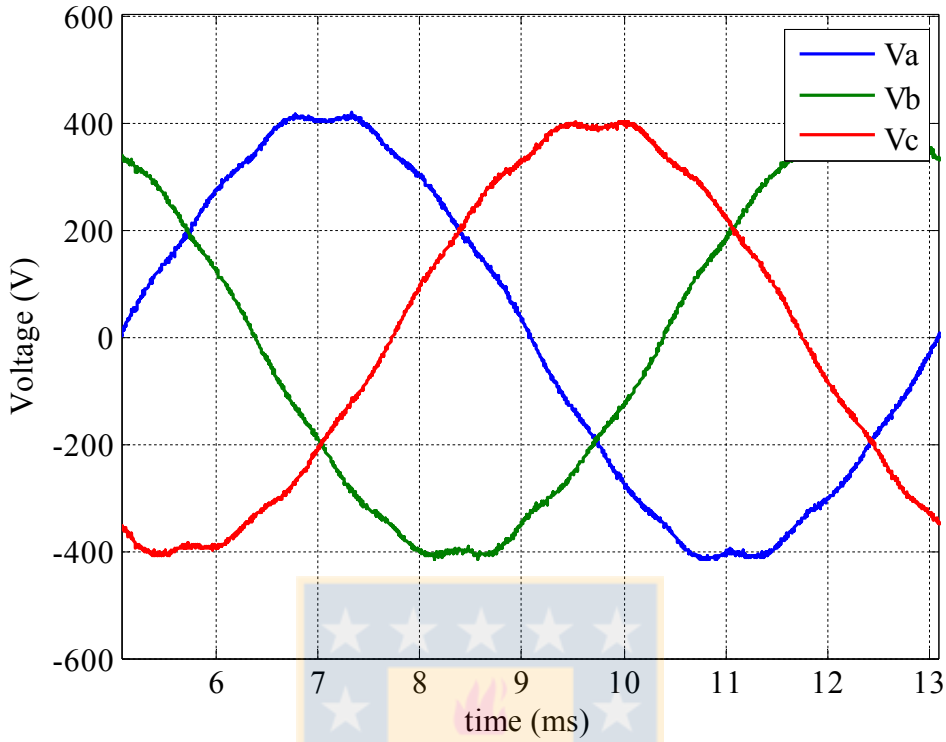

Fig. 4.23. Phase voltage of the machine prototype operating at nominal speed. (Source: own elaboration)

However, the thermal analysis of the machine is outside the scope of this doctoral dissertation.

The measured and computed no-load induced voltages of the machine prototype running at 1500 rpm are compared in Fig. 4.22, showing a good agreement. A better estimation is reached by the 3D finite element computation. However, the 3D simulation takes a lot of computation time compared with the 2D simulation. The induced voltages of the three-phase winding are depicted for a full period (8 ms), which represents a balanced voltage.

The measurement values of input power, output power, and total losses of the machine operating as a motor are shown in Fig. 4.24 for different values of load currents. The output power (measurement on the shaft) increases almost linearly up to the nominal current value, and after that point, the rate of change of power decreases as a result of an increase in the Joule losses in the winding.

The machine efficiency as a function of load current is depicted in Fig. 4.25. The maximum machine efficiency is obtained between 0.6 and 1 p.u. of the nominal current. The machine efficiency decreases to 92% at 1.5 p.u. of the nominal current.

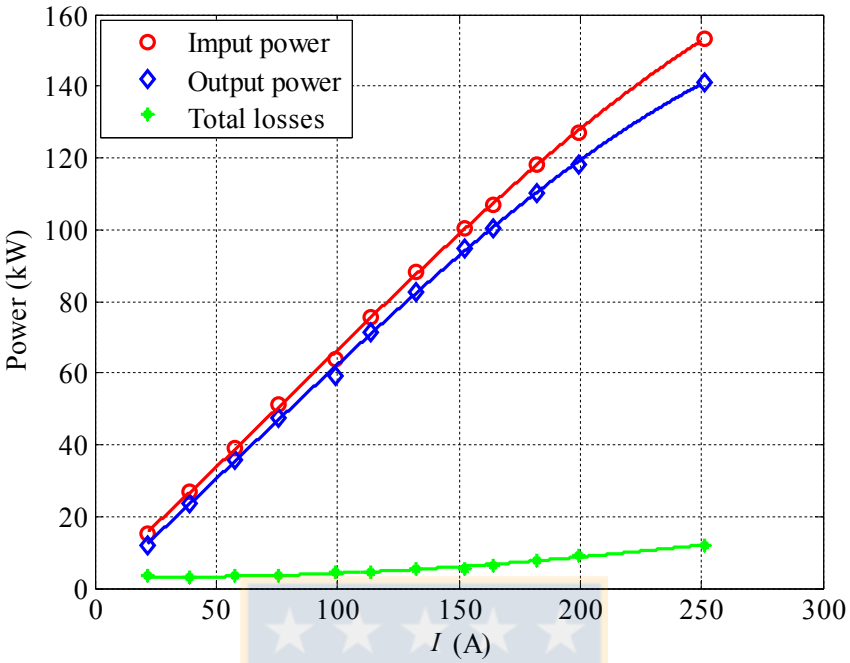

Fig. 4.24. Power balance of the machine prototype as a function of load current when operating at nominal speed. (Source: own elaboration)

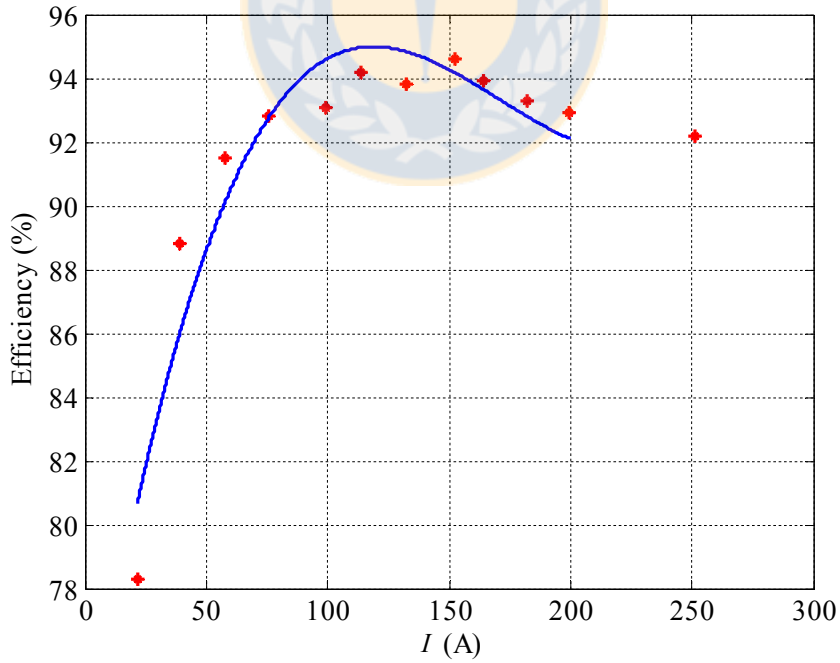

Fig. 4.25 Machine efficiency of the machine prototype as a function of load current when operating at nominal speed. (Source: own elaboration)

5 Conclusions

The aim of this doctoral dissertation was to develop design procedures for the optimal design of axial flux permanent magnet machines.

In the doctoral dissertation, a simple and accurate analytical method to design axial flux permanent magnet machines considering the saturation and leakage flux effects was presented. The design equation can be used during the dimensioning step of the machine to find the maximum electromagnetic torque developed by the machine for given values of tangential stress and outer diameter. Based on the analytical model and 3D FEM results, it was demonstrated that the slot height is a key parameter in the torque capability of a given machine. A deep slot increases the leakage flux and the magnetic voltage drop, which degrades the machine torque capacity. This disadvantage can be addressed using a multistage structure with two or more stators.

A 2D analytical model of the flux density waveform was developed for an axial flux permanent magnet machine considering the permanent magnet magnetic field, armature reaction magnetic field, and the slotting effect. The estimation of the armature reaction field is a novel method based on the magnetic field produced by a single phase coil and on the star of slots theory. The model shows an excellent agreement with the 2D finite element computations and was used to analyse the machine behaviour and to improve the accuracy of the design methodology.

In the optimization stage of the work, a novel rotor topology for a two-stator one-rotor axial flux permanent magnet machine was analysed and optimized to reduce the rotor losses when a tooth coil winding and an open-slot stator are used. Based on the finite element results, it is concluded that by adding steel lamination layers to each side of the permanent magnets, the losses can be effectively reduced. The steel lamination layers along with the non-ferromagnetic rotor structure allow to increase the no-load magnetic field thereby increasing the torque capability of the machine.

The electrically non-conductive material and the non-ferromagnetic material used in the rotor structure provide adequate mechanical strength, reduce the leakage flux between the poles, and guarantee the absence of eddy current losses.

Based on studies on the manufacturing effects, it was concluded that an alternative joining procedure will be designed to avoid additional losses. As a recommendation, different pole shapes should be studied, and a rectangular geometry could be an attractive solution to simplify the manufacture of the steel lamination layers. In such a case, the steel lamination can be made of I-shape steel magnetic sheets similarly as the manufacture of transformer cores. Furthermore, it is necessary to analyse the effect of the soft magnetic material to manufacture the magnetic layer.

A 100 kW prototype machine was manufactured to verify that the computed losses and machine efficiency are in good agreement.

References

Akita H., Nakahara Y., Miyake N., and Oikawa T., "New Core Structure and Manufacturing Method for High Efficiency of Permanent Magnet Motors," in *Rec. of 2003 IEEE Industry Applications Society Annual Meeting*, vol. 1, Salt Lake City, UT, October 2003, pp. 367–372.

Alberti L., Fornasiero E., Bianchi N., and Bolognani S., "Impact of rotor losses in a 12-slot 10-pole axial flux PM machine," in *Proc. IEEE IAS Annu. Meeting*, Oct. 5–9, 2008, pp. 1–8.

Alexandrova, J. and Jussila, H., "Comparison between models for eddy current loss calculations in rotor surface-mounted permanent magnets," in *Proc. IEEE ICEM*, 2010, pp. 978–982.

Atallah K., Howe D., Mellor P. H., and Stone D. A., "Rotor loss in permanent-magnet brushless AC machines," *IEEE Trans. Ind. Appl.*, vol. 36, no. 6, pp. 1612–1618, Nov./Dec. 2000.

Aydin M. and Güven M., "Comparing various PM synchronous generators: a feasible solution for high-power, off-highway, series hybrid, electric traction applications," *IEEE Veh. Technol. Mag.*, vol. 9, no. 1, pp. 36–45, Mar. 2014.

Aydin M. and Gulec M., "Reduction of cogging torque in double-rotor axial-flux permanent-magnet disk motors: A review of cost-effective magnet-skewing techniques with experimental verification," *IEEE Trans. Ind. Electron.*, vol. 61, no. 9, pp. 5025–5034, Sep. 2014.

Aydin M., Surong H., and Lipo T. A., "Torque quality and comparison of internal and external rotor axial flux surface-magnet disc machines," *IEEE Trans. Ind. Electron.*, vol. 53, no. 3, pp. 822–830, Jun. 2006.

Azzouzi J., Barakat G., and Dakyo B., "Quasi-3-D analytical modeling of the magnetic field of an axial flux permanent-magnet synchronous machine," *IEEE Trans. Energy Convers.*, vol. 20, no. 4, pp. 746–752, Dec. 2005.

Bianchi N. and Dai Pre M., "Use of the star of slots in designing fractional-slot single-layer synchronous motors," in *Proc. Inst. Elect. Eng.—Elect. Power Appl.*, vol. 153, no. 3, pp. 459–466, May 2006.

Bianchi N. and Fornasiero E., "Impact of MMF space harmonic on rotor losses in fractional-slot permanent-magnet machines," *IEEE Trans. Energy Convers.*, vol. 24, no. 2, pp. 323–328, Jun. 2009.

Bianchi N., Bolognani S., and Fornasiero E., “An overview of rotor losses determination in three-phase fractional-slot PM machines,” *IEEE Trans. Ind. Appl.*, vol. 46, no. 6, pp. 2338–2345, Nov./Dec. 2010.

Bianchi N., Dai Pre M., Alberti L., and Fornasiero E., “Theory and design of fractional-slot PM machines,” in *Conf. Rec. IEEE IAS Annu. Meeting*, New Orleans, LA, Sep. 23, 2007.

Bianchini C., Immovilli F., Lorenzani E., Bellini A., and Felici L., “Axial flux permanent magnet machine desing and optimization using multilayer 2-D simulation,” in *Proc. 39th Annu. Conf. IEEE Ind. Electron. Soc. (IECON)*, Vienna, Austria, Nov. 2013, pp. 2620–2625.

Campbell P., "Principles of a permanent-magnet axial-field d.c. machine," in *Proc. of the Institution of Electrical Engineers,* vol. 121, pp. 1489–1494, 1974.

Chan C. C., "Axial-Field Electrical Machines - Design and Applications," *IEEE Trans. Energy Convers.*, vol. EC-2, pp. 294–300, 1987.

Chan T. F., Lai L. L., and Shuming X., “Field computation for an axial flux permanent-magnet synchronous generator,” *IEEE Trans. Energy Convers.*, vol. 24, no. 1, pp. 1–11, Mar. 2009.

Crescimbini F., Lidozzi A., and Solero L., “High-speed generator and multilevel converter for energy recovery in automotive systems,” *IEEE Trans. Ind. Electron.*, vol. 59, no. 6, pp. 2678–2688, Jun. 2012.

Cros J. and Viarouge P., "Synthesis of high performance PM motors with concentrated windings," *IEEE Trans. Energy Convers.*, vol. 17, pp. 248–253, 2002.

Cros J., Viarouge P., and Gelinas C., "Design of PM brushless motors using iron-resin composites for automotive applications," in *The 1998 IEEE Industry Applications Conference, 1998, Thirty-Third IAS Annual Meeting*, 1998, pp. 5–11 vol. 1.

Cros J., Viarouge P., and Halila A., “Brush dc motors with concentrated windings and soft magnetic composites armatures,” in *Proc. IEEE IAS*, vol. I, Oct. 2001, pp. 2549–2556.

Donato G., Capponi F., and Caricchi F., “Fractional-slot concentrated-winding axial-flux permanent magnet machine with core wound coils,” *IEEE Trans. Ind. Appl.*, vol. 48, no. 2, pp. 630–641, Mar./Apr. 2012.

Donato G., Capponi F., and Caricchi F., “On the use of magnetic wedges in axial flux permanent magnet machines,” *IEEE Trans. Ind. Electron.*, vol. 60, no. 11, pp. 4831–4840, Nov. 2013.

El-Refaie A. M., "Fractional-slot concentrated-windings synchronous permanent magnet machines: Opportunities and challenges," *IEEE Trans. Ind. Electron.*, vol. 57, no. 1, pp. 107–121, Jan. 2010.

El-Refaie A. M., "Fractional-slot concentrated-windings: A paradigm shift in electrical machines," in *Proc. IEEE Workshop Elect. Mach. Design Control Diagnosis*, Paris, France, Mar. 2013, pp. 24–32.

El-Refaie A. M., Zhu Z. Q., Jahns T. M., and Howe D., "Winding inductances of fractional slot surface-mounted permanent magnet brushless machines," in *Conf. Rec. IEEE IAS Annu. Meeting*, Oct. 5–9, 2008, pp. 1–8.

Fang Z. X., Zhu Z. Q., Wu L. J., and Xia Z. P., "Simple and accurate analytical estimation of slotting effect on magnet loss in fractional-slot surface-mounted PM machines," in *Proc. 20th Int. Conf. Elect. Mach.*, Marseille, France, Sep. 2012, pp. 464–470.

Fukuma A., Kanazawa S., Miyagi D., and Takahashi N., "Investigation of AC loss of permanent magnet of SPM motor considering hysteresis and eddy-current losses," *IEEE Trans. Magn.*, vol. 41, no. 5, pp. 1964–1967, May 2005.

Gerada C., Bradley K.J., Sumner M., Asher G.; "Non-Linear Dynamic Modelling of Vector Controlled PM Synchronous Machines," in *EPE Conference*, Dresden 2005.

Gieras F., Wang R., and Kamper, M. 2008. *Axial Flux Permanent Magnet Machines*, Second edition, Dordrecht: Springer Science + Business Media B.V.

Gonzalez D. A., Tapia J. A., and Bettancourt A. L., "Design consideration to reduce cogging torque in axial flux permanent-magnet machines," *IEEE Trans. Magn.*, vol. 43, no. 8, pp. 3435–3440, Aug. 2007.

Hemeida A. and Sergeant P., "Analytical modeling of surface PMSM using a combined solution of Maxwell's equations and magnetic equivalent circuit," *IEEE Trans. Magn.*, vol. 50, no. 12, Dec. 2014.

Huang W., Bettayeb A., Kaczmarek R., and Vannier J., "Optimization of magnet segmentation for reduction of eddy-current losses in permanent magnet synchronous machine," *IEEE Trans. Energy Convers.*, vol. 25, no. 2, pp. 381–387, Jun. 2010.

Ishak D., Zhu Z. Q., and Howe D., "Eddy-current loss in the rotor magnets of permanent-magnet brushless machines having a fractional number of slots per pole," *IEEE Trans. Magn.*, vol. 41, no. 9, pp. 2462–2469, Sep. 2005.

Jack A. G., Mecrow B. C., Dickinson P. G., Stephenson D., Burdess J. S., Fawcett J. N., and Evans T., "Permanent magnet machines with powder iron cores and pre-pressed windings," in *Conf. Rec. IEEE-IAS Annu. Meeting*, Oct. 1999, pp. 97–103.

Jafari-Shiadeh S. M. and Ardebili M., "Analysis and comparison of axial-flux permanent-magnet brushless-DC machines with fractional-slot concentrated-windings," in *Power Electronics, Drive Systems and Technologies Conference (PEDSTC)*, 2013 4th, 2013, pp. 72–77.

Jara W., Lindh P., Tapia J. A., Petrov I., Repo A. K., and Pyrhönen J., "Rotor Eddy-Current Losses Reduction in an Axial Flux Permanent-Magnet Machine," *IEEE Trans. Ind. Electron.*, vol. 63, no. 8, pp. 4729–4737, Aug. 2016.

Jara W., Tapia J. A., Bianchi N., Pyrhonen J., and Wallace R., "Procedure for fast electromagnetic design of axial flux permanent magnet machines," in *Proc. 2014 Int. Conf. Elect. Mach.*, pp. 1396–1402, Sep. 2014.

Jara W., Tapia J., Pyrhonen J., and Lindh P., "Analytical electromagnetic torque estimation of an axial flux permanent magnet machine under saturation," in *2015 IEEE International Electric Machines & Drives Conference (IEMDC)*, Coeur d'Alene, ID, USA, 2015, pp. 1124–1130.

Juergens J., Ponick B., Winter O., and Fricassè A., "Influences of iron loss coefficients estimation on the prediction of iron losses for variable speed motors," in *2015 IEEE International Electric Machines & Drives Conference (IEMDC)*, Coeur d'Alene, ID, USA, 2015, pp. 1254–1259.

Jussila H. (2009), *Concentrated Winding Multiphase Permanent Magnet Machine Design and Electromagnetic Properties – Case Axial Flux Machine*, Doctoral dissertation (Acta Universitatis Lappeenrantaensis 374), Lappeenranta University of Technology.

Jussila H., Nerg J., Pyrhönen J., and Parviainen A., "Concentrated winding axial flux permanent magnet motor for industrial use," in *Proc. ICEM*, 2010, pp. 1–5.

Jussila H., Salminen P., Parviainen A., Nerg J., and Pyrhönen J., "Concentrated winding axial flux permanent magnet motor with plastic bonded magnets and sintered segmented magnets," in *Proc. ICEM*, Vilamoura, Portugal, Sep. 2008, pp. 1–5.

Kahourzade S., Mahmoudi A., Ping H. W., and Uddin M. N., "A comprehensive review of axial-flux permanent-magnet machines," *Can. J. Elect. Comput. Eng.*, vol. 37, no. 1, pp. 19–33, 2014.

Kim J. H., Choi W., and Sarlioglu B., "Closed-Form Solution for Axial Flux Permanent-Magnet Machines With a Traction Application Study," *IEEE Trans. Ind. Appl.*, vol. 52, no. 2, pp. 1775–1784, Mar/Apr. 2016.

Kurronen P. and Pyrhonen J., "Analytic calculation of axial-flux permanent-magnet motor torque," *Proc. IET – Electr. Power Appl.*, vol. 1, no. 1, pp. 59–63, Jan. 2007.

Letelier A. B., Gonzalez D. A., Tapia J. A., Wallace R., and Valenzuela M. A., “Cogging torque reduction in an axial flux PM machine via stator slot displacement and skewing,” *IEEE Trans. Ind. Appl.*, vol. 43, no. 3, pp. 685–693, May/Jun. 2007.

Lindh P., Montonen J., Jussila H., Pyrhönen J., Jara W., and Tapia J. A., "Axial flux machine structure reducing rotor eddy current losses," in *2015 IEEE International Electric Machines & Drives Conference (IEMDC)*, Coeur d'Alene, ID, USA, 2015, pp. 143–146.

Magnussen F. and Sadarangani C., "Winding factors and Joule losses of permanent magnet machines with concentrated windings," in *IEEE International Electric Machines and Drives Conference IEMDC'03*, vol.1, pp. 333–339, 2003.

Markovic M. and Perriard Y., “A simplified determination of the permanent magnet (PM) eddy current losses due to slotting in a PM rotating motor,” in *Proc. ICEMS, Oct. 2008*, pp. 309–313.

Mirzaei M., Binder A., Funieru B., and Susic M., “Analytical calculations of induced eddy currents losses in the magnets of surface mounted PM machine with consideration of circumferential and axial segmentation effect,” *IEEE Trans. Magn.*, vol. 48, no. 12, pp. 4831–4841, Dec. 2012.

Nakahara A., Deguchi K., Kikuchi S., and Enomoto Y., "Comparative electrical design of radial- and axial-flux permanent magnet synchronous machines under space limitation," in *2014 International Conference on Electrical Machines (ICEM)*, Berlin, 2014, pp. 422–428.

Parviainen A. (2005), *Design of Axial-Flux permanent-Magnet Low-Speed Machines and Performance Comparison between Radial-Flux and Axial-Flux Machines*, Doctoral dissertation (Acta Universitatis Lappeenrantaensis 208), Lappeenranta University of Technology.

Parviainen A., Niemelä M., and Pyrhönen J., “Modeling of axial permanent-magnet machines,” *IEEE Trans. Ind. Appl.*, vol. 40, no. 5, pp. 1333–1340, Sep./Oct. 2004.

Petrov I. (2015), *Cost Reduction of Permanent Magnet Synchronous Machines*, Doctoral dissertation (Acta Universitatis Lappeenrantaensis 638), Lappeenranta University of Technology.

Polikarpova M., Ponomarev P., Lindh P., Petrov I., Jara W., Naumanen V., Tapia J. A., and Pyrhönen J., "Hybrid Cooling Method of Axial-Flux Permanent Magnet Machines for a Vehicle Applications," *IEEE Trans. Ind. Electron.*, vol. 63, no. 12, pp. 7382–7390, Dec. 2015.

Ponomarev P., Lindh P., and Pyrhonen J., “Effect of slot-and-pole combination on the leakage inductance and the performance of tooth-coil permanent-magnet

synchronous machines," *IEEE Trans. Ind. Electron.*, vol. 60, no. 10, pp. 4310–4317, Oct. 2013.

Ponomarev P., Petrov I., and Pyrhonen J., "Influence of travelling current linkage harmonics on inductance variation, torque ripple and sensorless capability of tooth-coil permanent-magnet synchronous machines," *IEEE Trans. Magn.*, vol. 50, no. 1, pp. 1–8, Jan 2014.

Pyrhonen J. et al., "Hysteresis losses in sintered NdFeB permanent magnets in rotating electrical machines," *IEEE Trans. Ind. Electron.*, vol. 62, no. 2, pp. 857–865, Feb. 2015.

Pyrhönen, J., Jokinen, T., and Hrabovcová, V. (2008), *Design of Rotating Electrical Machines*, Chichester: John Wiley & Sons, Ltd.

Pyrhönen J., Jussila H., Alexandrova Y., Rafajdus P., and Nerg J., "Harmonic loss calculation in rotor surface magnets—New analytic approach," *IEEE Trans. Magn.*, vol. 48, no. 8, pp. 2358–2366, Aug. 2012.

Pyrhönen J., Ruuskanen V., Nerg J., Puranen J., and Jussila H., "Permanent-magnet length effects in ac machines," *IEEE Trans. Magn.*, vol. 46, no. 10, pp. 3783–3789, Oct. 2010.

Richter R. and Brüderlink R. (1967), *Elektrische Maschinen:* A*llgemeine Berechnungselemente. Die Gleichstrommaschinen* Electrical Machines: General Calculation Elements. DC Machines], Basle & Stuttgart: Birkhäuser Verlag.

Rottach M., Gerada C., Hamiti T., and Wheeler P. W., "A computationally efficient design procedure for actuator motors using magnetic reluctanceand thermal resistance network models," in *Proc. 20th IEEE Int. Conf. Elect. Mach.*, 2012, pp. 2526–2532.

Sharkh S., Qazalbash A., Irenji N. T., and Wills R. G., "Effect of slot configuration and airgap and magnet thicknesses on rotor electromagnetic loss in surface PM synchronous machines," in *Proc. ICEMS*, Aug. 2011, pp. 1–6.

Surong H., Jian L., Leonardi F., and Lipo T. A., "A comparison of power density for axial flux machines based on general purpose sizing equations," *IEEE Trans. Energy Convers.*, vol. 14, pp. 185–192, 1999.

Tapia J., Pyrhonen J., Puranen J., Nyman S., and Lindh P., "Optimal design of large permanent magnet synchronous generators," *IEEE Trans. Magn.*, vol. 49, no. 1, pp. 642–650, Jan. 2013.

Tiegna H., Bellara A., Amara Y., and Barakat G., “Analytical modeling of the open-circuit magnetic field in axial flux permanent-magnet machines with semi-closed slots,” *IEEE Trans. Magn.*, vol. 48, no. 3, pp. 1212–1226, Mar. 2012.

Voldek A. I. (1974), *Electrical Machines*, (in Russian), Leningrad: Energy.

Wallace R., Alexandrova J., Vera B., Tapia J., Pyrhonen J., and Lindh P., "P.M synchronous generator design analytical method," in *2012 International Symposium on Power Electronics, Electrical Drives, Automation and Motion (SPEEDAM),* 2012, pp. 625–631.

Wang A., Li H., and Liu C.-T., “On the material and temperature impacts of interior permanent magnet machine for electric vehicle applications,” *IEEE Trans. Magn.*, vol. 44, no. 11, pp. 4329–4332, Nov. 2008.

Wang J., Atallah K., Chin R., Arshand V. M., and Lendenmann H., “Rotor eddy-current loss in permanent-magnet brushless AC machines,” *IEEE Trans. Magn.*, vol. 46, no. 7, pp. 2701–2707, Jul. 2010.

Wills D. A. and Kamper M. J., “Reducing PM eddy current rotor losses by partial magnet and rotor yoke segmentation,” in *Proc. ICEM*, 2010, pp. 1–6.

Wrobel R., Mellor P. H., Popescu M., and Staton D. A., "Power Loss Analysis in Thermal Design of Permanent-Magnet Machines—A Review," *IEEE Trans. Ind. Appl.*, vol. 52, no. 2, pp. 1359–1368, March/April 2016.

Wu L. J., Zhu Z. Q., Staton D., Popescu M., and Hawkins D., “Analytical modelling and analysis of open-circuit PM power loss in surface mounted permanent magnet machines,” *IEEE Trans. Magn.*, vol. 48, no. 3, pp. 1234–1247, Mar. 2012.

Yamazaki K. and Fukushima Y., “Effect of eddy-current loss reduction by magnet segmentation in synchronous motors with concentrated windings*,” IEEE Trans. Ind. Appl.*, vol. 47, no. 2, pp. 779–788, Mar./Apr. 2011.

Yang Y.-P. and Chuang D. S., “Optimal design and control of a wheel motor for electric passenger cars,” *IEEE Trans. Magn.*, vol. 43, no. 1, pp. 51–61, Jan. 2007.

Yokoi Y., Higuchi T., and Miyamoto Y., "General formulation of winding factor for fractional-slot concentrated winding design," *IET Electric Power Applications*, vol. 10, no. 4, pp. 231–239, 2016.

Zarko D., Ban D., and Lipo T. A., “Analytical calculation of magnetic field distribution in the slotted air gap of a surface paramagnet-magnet motor using complex relative air-gap permeance,” *IEEE Trans. Magn.*, vol. 42, no. 7, pp. 1828–1837, Jul. 2006.

Zhu Z. Q. and Howe D., "Instantaneous magnetic-field distribution in brushless permanent-magnet dc motors, Part III: Effect of stator slotting," *IEEE Trans. Magn.*, vol. 29, no. 1, pp. 143–151, Jan. 1993.

Zhu Z. Q., Howe D., and Chan C. C., "Improved analytical model for predicting the magnetic field distribution in brushless permanent-magnet machines," *IEEE Trans. Magn*., vol. 38, no. 1, pp. 229–238, Jan. 2002.

Zhu Z. Q., Howe D., Bolte E., and Ackerman B., "Instantaneous magnetic field distribution in brushless permanent magnet dc motors, Part I: Open-circuit field," *IEEE Trans. Magn.*, vol. 29, no. 1, pp. 124–135, Jan. 1993.

Zhu Z. Q., Howe D., Bolte E., and Ackerman B., "Instantaneous magnetic field distribution in brushless permanent magnet dc motors, part IV: Magnetic field on load," *IEEE Trans. Magn.*, vol. 29, no. 1, pp. 152–158, Jan. 1993.

Appendix A: Slot leakage inductance equations

To derive the slot leakage inductance equations for a TCW, two methods are considered. The first one estimates the slot leakage inductance from the definition of the energy stored in a magnetic field

$$W_{\Phi} = \frac{1}{2\mu}\int_{V} B^2 \,\mathrm{d}V = \frac{1}{2}LI^2, \tag{A.1}$$

whereas the second one estimates the slot leakage inductance from the voltage induced in a phase winding

$$E = L\frac{\mathrm{d}I}{\mathrm{d}t}. \tag{A.2}$$

a) Slot leakage inductance for vertical coils from the magnetic energy

Considering the slot geometry and the magnetic flux path shown in Fig. A.1(a) and (b), respectively, and assuming that the iron of the teeth is infinitely permeable, all the leakage magnetic energy is stored in the slot. Neglecting the end effect, the flux density distribution at a given height h is given by

$$B = \begin{cases} 2\dfrac{\mu_0}{b_\mathrm{s}}\dfrac{h}{h_\mathrm{s}}\Theta_1 & 0 < h < \dfrac{h_\mathrm{s}}{2} \\ \dfrac{\mu_0}{b_\mathrm{s}}\left(\Theta_1 + \dfrac{2h}{h_\mathrm{s}}\Theta_2\right) & \dfrac{h_\mathrm{s}}{2} < h < h_\mathrm{s} \\ \dfrac{\mu_0}{\dfrac{2(b_0 - b_\mathrm{s})}{h_\mathrm{hs}}h + b_\mathrm{s}}(\Theta_1 + \Theta_2) & h_\mathrm{s} < h < h_\mathrm{s} + \dfrac{h_\mathrm{hs}}{2} \\ \dfrac{\mu_0}{b_0}(\Theta_1 + \Theta_2) & h_\mathrm{s} + \dfrac{h_\mathrm{hs}}{2} < h < h_\mathrm{s} + h_\mathrm{hs} \end{cases}, \tag{A.3}$$

where Θ_1 and Θ_2 are the total current linkages of the bottom coil and the upper coils, respectively. Substituting Eq. (A.3) into Eq. (A.1) and integrating along the slot, the leakage magnetic energy results in

$$W_{\Phi} = \frac{1}{2}\mu_0 l_\mathrm{ef}\Theta^2\left\{\frac{5+3g}{8}\frac{h_\mathrm{s}}{3b_\mathrm{s}} + \frac{1+g}{2}\left[\frac{h_\mathrm{hs}}{2(b_\mathrm{s}-b_0)}\ln\frac{b_\mathrm{s}}{b_0} + \frac{h_\mathrm{hs}}{2b_0}\right]\right\}, \tag{A.4}$$

where Eq. (A.4) can be defined in terms of the slot permeance factor λ_uv

$$\Theta_1 = \Theta_2 = \frac{\Theta}{2} = \frac{z_\mathrm{Q}I}{2}. \tag{A.5}$$

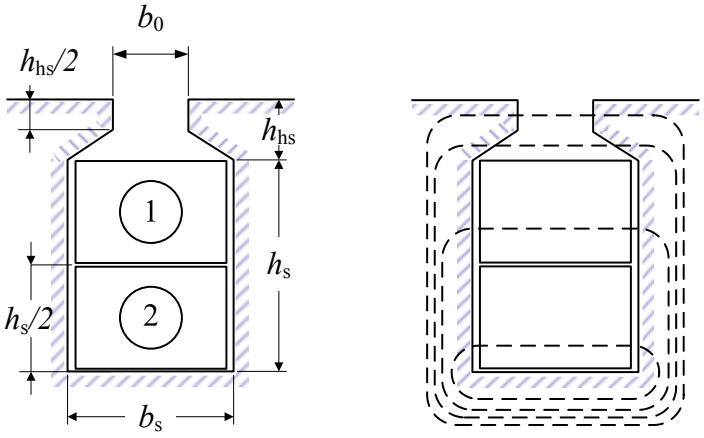

(a) (b)

Fig. A.1. (a) Slot geometry dimensions, (b) flux path in the different sections of the slot for a double-layer winding with vertical coils. (Source: own elaboration)

Equation (A.4) can be defined in terms of the slot permeance factor for vertical coils λ_{uv}

$$\lambda_{uv} = k_{1v}\frac{h_s}{3b_s} + k_2\left(\frac{h_{hs}}{2(b_s - b_0)}\ln\frac{b_s}{b_0} + \frac{h_{hs}}{2b_0}\right), \tag{A.6}$$

where

$$k_{1v} = \frac{5 + 3g}{8} \tag{A.7}$$

and

$$k_2 = \frac{1 + g}{2}. \tag{A.8}$$

Considering the last term of Eq. (A.1), the slot leakage inductance is written as

$$L_{uv} = \frac{2W_\Phi}{I^2} = \mu_0 l_{ef} {z_Q}^2 \lambda_{uv}. \tag{A.9}$$

For a DL winding, the number of conductors in a slot z_Q is related to the number of turns in series in phase N by

$$z_Q = \frac{2mN}{Q_s}, \tag{A.10}$$

and the slot leakage inductance of a phase winding becomes

$$L_{\mathrm{uv}} = \frac{4m}{Q_{\mathrm{s}}}\mu_0 l_{\mathrm{ef}} N^2 \lambda_{\mathrm{uv}}\,. \tag{A.11}$$

b) Slot leakage inductance for vertical coils from the induced voltage

To determine the slot leakage inductance from the induced voltage, it is necessary to estimate the self- and mutual leakage inductances for the coil configurations shown in Fig. A.1.

The flux density distribution produced by coil 1 (bottom coil) along the slot is given by

$$B_1 = \begin{cases} 2\dfrac{\mu_0}{b_{\mathrm{s}}}\dfrac{h}{h_{\mathrm{s}}}\Theta_1 & 0 < h < \dfrac{h_{\mathrm{s}}}{2} \\ \dfrac{\mu_0}{b_{\mathrm{s}}}\Theta_1 & \dfrac{h_{\mathrm{s}}}{2} < h < h_{\mathrm{s}} \\ \dfrac{\mu_0}{\dfrac{2(b_0 - b_{\mathrm{s}})}{h_{\mathrm{hs}}}h + b_{\mathrm{s}}}\Theta_1 & h_{\mathrm{s}} < h < h_{\mathrm{s}} + \dfrac{h_{\mathrm{hs}}}{2} \\ \dfrac{\mu_0}{b_0}\Theta_1 & h_{\mathrm{s}} + \dfrac{h_{\mathrm{hs}}}{2} < h < h_{\mathrm{s}} + h_{\mathrm{hs}} \end{cases} \tag{A.12}$$

and the flux density distribution produced by coil 2 (bottom coil)

$$B_2 = \begin{cases} 0 & 0 < h < \dfrac{h_{\mathrm{s}}}{2} \\ 2\dfrac{\mu_0}{b_{\mathrm{s}}}\dfrac{h}{h_{\mathrm{s}}}\Theta_2 & \dfrac{h_{\mathrm{s}}}{2} < h < h_{\mathrm{s}} \\ \dfrac{\mu_0}{\dfrac{2(b_0 - b_{\mathrm{s}})}{h_{\mathrm{hs}}}h + b_{\mathrm{s}}}\Theta_2 & h_{\mathrm{s}} < h < h_{\mathrm{s}} + \dfrac{h_{\mathrm{hs}}}{2} \\ \dfrac{\mu_0}{b_0}\Theta_2 & h_{\mathrm{s}} + \dfrac{h_{\mathrm{hs}}}{2} < h < h_{\mathrm{s}} + h_{\mathrm{hs}} \end{cases}\,. \tag{A.13}$$

The self-inductance of coil 1 is

$$L_1 = \frac{1}{\mu I^2}\int_V B_1^2\,\mathrm{d}V. \tag{A.14}$$

Integrating Eq. (A.14) results in

$$L_1 = \mu_0 l_{\mathrm{ef}} z_{\mathrm{c}}^2 \lambda_1\,, \tag{A.15}$$

where

$$\lambda_1 = \frac{2h_s}{3b_s} + \frac{h_{hs}}{2(b_s - b_0)} \ln\frac{b_s}{b_0} + \frac{h_{hs}}{2b_0} \tag{A.16}$$

and

$$z_c = \frac{z_Q}{2}. \tag{A.17}$$

Following the same procedure for the self-inductance of coil 2

$$L_2 = \frac{1}{\mu I^2} \int_V B_2^2 \mathrm{d}V, \tag{A.18}$$

the integration results in

$$L_2 = \mu_0 l_{ef} z_c^2 \lambda_2, \tag{A.19}$$

where

$$\lambda_2 = \frac{h_s}{6b_s} + \frac{h_{hs}}{2(b_s - b_0)} \ln\frac{b_s}{b_0} + \frac{h_{hs}}{2b_0}. \tag{A.20}$$

The mutual inductance can be found by

$$M = \frac{1}{\mu I^2} \int_V B_1 B_2 \mathrm{d}V \tag{A.21}$$

By substituting Eq. (A.12) and Eq. (A.13) into Eq. (A.21) the mutual inductance becomes

$$M = \mu_0 l_{ef} z_c^2 \lambda_M, \tag{A.22}$$

where

$$\lambda_M = \frac{h_s}{4b_s} + \frac{h_{hs}}{2(b_s - b_0)} \ln\frac{b_s}{b_0} + \frac{h_{hs}}{2b_0}. \tag{A.23}$$

For the case where the coil sides in the slot belong to the same phase, the self-inductance can be written as

$$L = \mu_0 l_{ef} (2z_c)^2 \lambda, \tag{A.24}$$

Table A.1. Main factors to determine the slot leakage inductance from $q = 0.25$ to $q = 0.5$. (Source: own elaboration)

q	q'	y_q'	W'	a	b
1/4 , 1/2	1	3	2	1	0
2/7 , 2/5	4	12	10 , 14	1	1
3/8 , 3/10	3	9	8, 10	1	2
7/20 , 7/22	7	21	20 , 22	1	6
.	.	.	.	.	.
.	.	.	.	.	.
.	.	.	.	.	.
From 1/4 to 1/2	$q\left(\frac{2p}{t'}\right)$	$y_q\left(\frac{2p}{t'}\right)$	$W\left(\frac{2p}{t'}\right)$	$a = \lvert y_q' - W' \rvert$	$q' - \lvert y_q' - W' \rvert$

where

$$\lambda = \frac{h_s}{3b_s} + \frac{h_{hs}}{2(b_s - b_0)} \ln \frac{b_s}{b_0} + \frac{h_{hs}}{2b_0}. \tag{A.25}$$

To determine the slot leakage inductance of a phase winding, it is necessary to first obtain the coil distribution of different phases in the slots. Therefore, each slot and pole combination has to be analysed individually. This is similar to determining the factor g of Eq. (A.7) and Eq. (A.8). However, it is found that for a given combination of slots and poles from $q = 0.25$ to $q = 0.5$, it is possible to define a generalized expression for the slot leakage inductance. In such configurations, a phase winding has $a = \lvert y_q' - W' \rvert$ slots with coil sides of different phases and $b = q' - \lvert y_q' - W' \rvert$ slots with coil sides of the same phase. For example, Table A.1 shows the values of a and b for the slot and pole configurations shown in Fig A.3.

The voltage induced in a phase winding and produced by the slot leakage flux is given by

$$E = L_{uv} \frac{dI}{dt}. \tag{A.26}$$

For example, for phase W

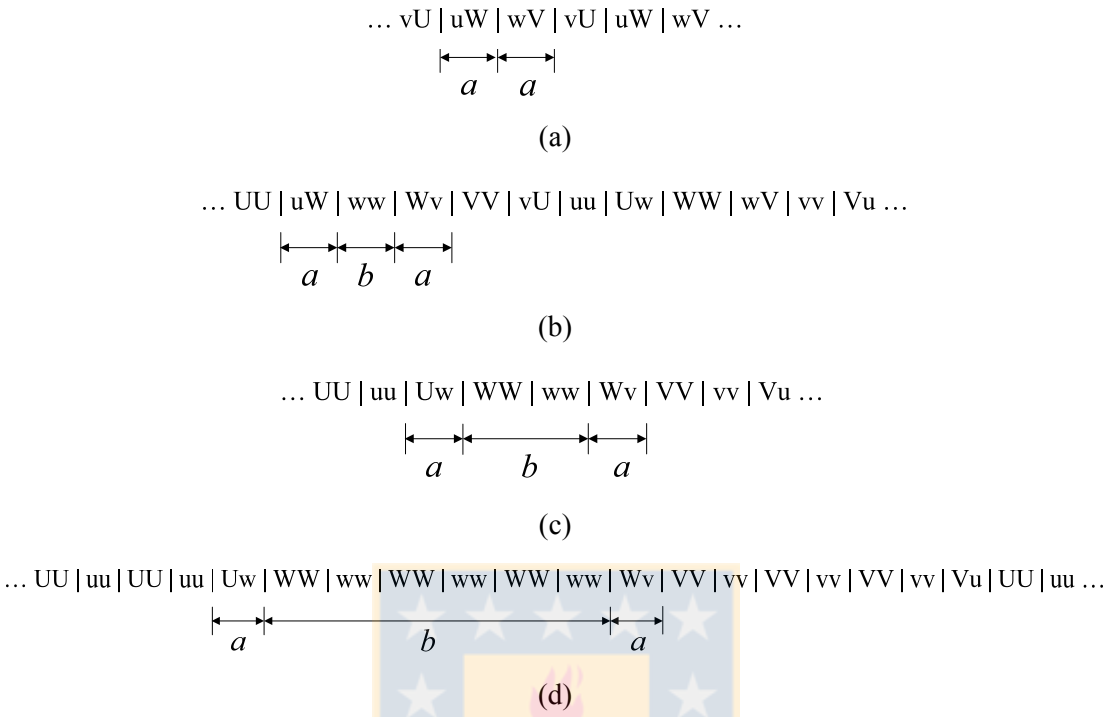

Fig. A.2. Winding layout for the DL-TCW with (a) q = 1/4 and q = 1/2, (b) q = 2/7 and q = 2/5, (c) q = 3/8 and q = 3/10 and (d) q = 7/20 and q = 7/22. (Source: own elaboration)

$$E_{\mathrm{W}} = t'\left[\left(q' - \left|{y_{\mathrm{q}}}' - W'\right|\right)L\frac{\mathrm{d}I_{\mathrm{W}}}{\mathrm{d}t} + \left|{y_{\mathrm{q}}}' - W'\right|L_1\frac{\mathrm{d}I_{\mathrm{W}}}{\mathrm{d}t} + \left|{y_{\mathrm{q}}}' - W'\right|L_2\frac{\mathrm{d}I_{\mathrm{W}}}{\mathrm{d}t}\right] - t'\left|{y_{\mathrm{q}}}' - W'\right|M\frac{\mathrm{d}I_{\mathrm{U}}}{\mathrm{d}t} - t'\left|{y_{\mathrm{q}}}' - W'\right|M\frac{\mathrm{d}I_{\mathrm{V}}}{\mathrm{d}t} \tag{A.27}$$

considering a three-phase winding with balanced currents

$$\frac{\mathrm{d}I_{\mathrm{U}}}{\mathrm{d}t} + \frac{\mathrm{d}I_{\mathrm{V}}}{\mathrm{d}t} + \frac{\mathrm{d}I_{\mathrm{W}}}{\mathrm{d}t} = 0 \tag{A.28}$$

and substituting Eq. (A.15), Eq. (A.19), Eq. (A.22), and Eq. (A.24) into Eq. (A.27)

$$E = 2p\mu_0 l_{\mathrm{ef}} z_{\mathrm{c}}^2\left[\left(\frac{4}{3}\mathrm{q} - \frac{1}{4}\left|y_{\mathrm{Q}} - W\right|\right)\frac{h_{\mathrm{s}}}{b_{\mathrm{s}}} + \left(4\mathrm{q} - \left|y_{\mathrm{Q}} - W\right|\right)\lambda_{\mathrm{hs}}\right]\frac{\mathrm{d}I_{\mathrm{W}}}{\mathrm{d}t}, \tag{A.29}$$

where λ_{hs} is defined as the slot head leakage permeance factor

$$\lambda_{\mathrm{hs}} = \frac{h_{\mathrm{hs}}}{b_{\mathrm{s}} - b_0}\ln\frac{b_{\mathrm{s}}}{b_0} + \frac{h_{\mathrm{hs}}}{2b_0}. \tag{A.30}$$

Comparing Eq. (A.26) with Eq. (A.29), the slot leakage inductance is written as

$$L_{\mathrm{uv}} = \frac{4m}{Q_{\mathrm{s}}}\mu_0 l_{\mathrm{ef}} N^2 \lambda_{\mathrm{uv}}\,, \tag{A.31}$$

where

$$\lambda_{\mathrm{uv}} = \left[\left(1 - \frac{3}{16}\frac{\left|y_{\mathrm{Q}} - W\right|}{q}\right)\frac{h_{\mathrm{s}}}{3b_{\mathrm{s}}} + \left(1 - \frac{\left|y_{\mathrm{Q}} - W\right|}{4q}\right)\lambda_{\mathrm{hs}}\right]. \tag{A.32}$$

Based on Eq. (A.6) and Eq. (A.32), it is found that from q = 0.25 to q = 0.5, the factors $k_{1\mathrm{v}}$ and k_2 can be written as

$$k_{1\mathrm{v}} = 1 - \frac{3}{16}\frac{\left|y_{\mathrm{Q}} - W\right|}{q} \tag{A.33}$$

and

$$k_2 = 1 - \frac{\left|y_{\mathrm{Q}} - W\right|}{4q}. \tag{A.34}$$

c) Slot leakage inductance for horizontal coils from the magnetic energy

The flux density distribution produced by the arrangement of the coils shown in Fig. A.3 is given by

$$B = \begin{cases} 2\dfrac{\mu_0}{b_{\mathrm{s}}}\dfrac{h}{h_{\mathrm{s}}}(\Theta_1 + \Theta_2) & 0 < h < h_{\mathrm{s}} \\ \dfrac{\mu_0}{\dfrac{2(b_0 - b_{\mathrm{s}})}{h_{\mathrm{hs}}}h + b_{\mathrm{s}}}(\Theta_1 + \Theta_2) & h_{\mathrm{s}} < h < h_{\mathrm{s}} + \dfrac{h_{\mathrm{hs}}}{2} \\ \dfrac{\mu_0}{b_0}(\Theta_1 + \Theta_2) & h_{\mathrm{s}} + \dfrac{h_{\mathrm{hs}}}{2} < h < h_{\mathrm{s}} + h_{\mathrm{hs}} \end{cases} \tag{A.35}$$

By substituting Eq. (A.3) into Eq. (A.1) and integrating along the slot, the leakage magnetic energy is written as

$$W_{\Phi} = \frac{1}{2}\mu_0 l_{\mathrm{ef}}\Theta^2\left\{\frac{1+g}{2}\frac{h_{\mathrm{s}}}{3b_{\mathrm{s}}} + \frac{1+g}{2}\left[\frac{h_{\mathrm{hs}}}{2(b_{\mathrm{s}} - b_0)}\ln\frac{b_{\mathrm{s}}}{b_0} + \frac{h_{\mathrm{hs}}}{2b_0}\right]\right\}, \tag{A.36}$$

The terms between in the curly brackets are defined as the slot permeance factor for horizontal coils λ_{uh}

$$\lambda_{\mathrm{uh}} = k_{1\mathrm{h}}\frac{h_{\mathrm{s}}}{3b_{\mathrm{s}}} + k_2\left(\frac{h_{\mathrm{hs}}}{2(b_{\mathrm{s}} - b_0)}\ln\frac{b_{\mathrm{s}}}{b_0} + \frac{h_{\mathrm{hs}}}{2b_0}\right), \tag{A.37}$$

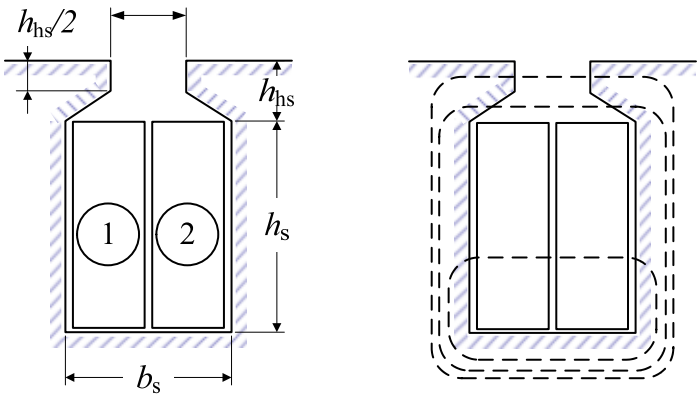

(a) (b)

Fig. A.3. (a) Slot geometry dimensions, (b) flux path in the different sections of the slot for a double-layer winding with horizontal coils. (Source: own elaboration)

where

$$k_{1h} = k_2 \tag{A.38}$$

By using Eq. (A.1) and Eq. (A.10), the slot leakage inductance of the phase winding for horizontal coils is given by

$$L_{uh} = \frac{4m}{Q_s}\mu_0 l_{ef} N^2 \lambda_{uh}\,. \tag{A.39}$$

d) Slot leakage inductance for horizontal coils from the induced voltage

The flux density distribution produced by coil 1 (left-hand coil) and coil 2 (right-hand coil) shown in Fig A.3 is given by

$$B_1 = B_2 = \begin{cases} 2\dfrac{\mu_0}{b_s}\dfrac{h}{h_s}\Theta_1 & 0 < h < h_s \\ \dfrac{\mu_0}{\dfrac{2(b_0 - b_s)}{h_{hs}}h + b_s}\Theta_1 & h_s < h < h_s + \dfrac{h_{hs}}{2} \\ \dfrac{\mu_0}{b_0}\Theta_1 & h_s + \dfrac{h_{hs}}{2} < h < h_s + h_{hs} \end{cases} \tag{A.40}$$

The self-inductance and mutual inductance of the coils are

$$L_1 = L_1 = M = \frac{1}{\mu I^2}\int_V B_1^2 \, \mathrm{d}V \tag{A.41}$$

Integrating Eq. (A.41) results in

$$L_1 = L_1 = M = \mu_0 l_{\mathrm{ef}} z_{\mathrm{c}}^2 \lambda_1 \,, \tag{A.42}$$

where

$$\lambda_1 = \frac{h_{\mathrm{s}}}{3b_{\mathrm{s}}} + \frac{h_{\mathrm{hs}}}{2(b_{\mathrm{s}} - b_0)} \ln\frac{b_{\mathrm{s}}}{b_0} + \frac{h_{\mathrm{hs}}}{2b_0} \tag{A.43}$$

Following the same procedure described in section b of Appendix A, the slot leakage inductance is given by

$$L_{\mathrm{uh}} = \frac{4m}{Q_{\mathrm{s}}} \mu_0 l_{\mathrm{ef}} N^2 \lambda_{\mathrm{uh}} \,, \tag{A.44}$$

where

$$\lambda_{\mathrm{uh}} = \left(1 - \frac{|y_{\mathrm{Q}} - W|}{4q}\right)\frac{h_{\mathrm{s}}}{3b_{\mathrm{s}}} + \left(1 - \frac{|y_{\mathrm{Q}} - W|}{4q}\right)\lambda_{\mathrm{hs}} \,, \tag{A.45}$$

which can be written as

$$\lambda_{\mathrm{uh}} = k_2 \frac{h_{\mathrm{s}}}{3b_{\mathrm{s}}} + k_2 \lambda_{\mathrm{hs}} \,. \tag{A.46}$$